Self-assembled Ge/Si core/shell quantum dots in alumina matrix for application in photo-electric conversion

Nekić, Nikolina

Doctoral thesis / Disertacija

2018

Degree Grantor / Ustanova koja je dodijelila akademski / stručni stupanj: **University of Zagreb, Faculty of Science / Sveučilište u Zagrebu, Prirodoslovno-matematički fakultet**

Permanent link / Trajna poveznica: https://urn.nsk.hr/urn:nbn:hr:217:504365

Rights / Prava: In copyright/Zaštićeno autorskim pravom.

Download date / Datum preuzimanja: **2024-04-18**

Repository / Repozitorij:

Repository of the Faculty of Science - University of Zagreb

FACULTY OF SCIENCE

DEPARTMENT OF PHYSICS

Nikolina Nekić

SELF-ASSEMBLED Ge/Si CORE/SHELL QUANTUM DOTS IN ALUMINA MATRIX FOR APPLICATION IN PHOTO-ELECTRIC CONVERSION

DOCTORAL DISSERTATION

Zagreb, 2018

University of Zagreb

FACULTY OF SCIENCE

DEPARTMENT OF PHYSICS

Nikolina Nekić

SELF-ASSEMBLED Ge/Si CORE/SHELL QUANTUM DOTS IN ALUMINA MATRIX FOR APPLICATION IN PHOTO-ELECTRIC CONVERSION

DOCTORAL DISSERTATION

Supervisor:

Dr.sc. Maja Buljan

Zagreb, 2018

PRIRODOSLOVNO-MATEMATIČKI FAKULTET

FIZIČKI ODSJEK

Nikolina Nekić

SAMOUREĐENE KVANTNE TOČKE Ge/Si JEZGRA/LJUSKA U ALUMINSKOJ MATRICI S PRIMJENOM U FOTOELEKTRIČNOJ KONVERZIJI

DOKTORSKI RAD

Mentor:

Dr.sc. Maja Buljan

Zagreb, 2018

Information about the supervisor

Name and surname: dr. sc. Maja Buljan

Dr. Sc. Maja Buljan is a senior research associate at Ruđer Bošković Institute in Zagreb, Department of Material Science and the head of the Laboratory for thin films. She received her PhD in synthesis and structural characterization of semiconductor nanocrystals at the University of Zagreb, Croatia, in 2008. She spent one year at the Charles University in Prague, Czech Republic, working on characterization of nano-materials by X-ray based techniques.

Maja is most notable for her development of materials based on self-assembled Ge-based quantum dots in amorphous dielectric matrices and their fabrication methods. She is also involved in the theoretical description and interpretation of Grazing Incidence Small Angle X-ray Scattering (GISAXS) from three-dimensional quantum dot lattices and other ordered nano-structured materials.

List of her publications is available at: https://bib.irb.hr/lista-radova?autor=242416

Web-page: http://www.irb.hr/eng/People/Maja-Buljan

Most significant recent papers:

1. **M. Buljan**, M. Karlušić, N. Nekić, M. Jerčinović, I. Bogdanović-Radović, S. Bernstorff, N. Radić, I. Mekterović. *GISAXS analysis of ion beam modified films and surfaces*, Comp. Phys. Comm. 212, 69-81, (2017)

2. N. Nekić, J. Sancho Parramon, I. Bogdanović-Radović, J. Grenzer, R. Huebner, M. Ivanda, **M. Buljan**. *Ge/Si core/shell quantum dots in alumina: tuning the optical absorption by the core and shell size* Nanophotonics 6 (5), 1055-1062 (2017).

3. **M. Buljan**, S. Facsko, I. Delač Marion, V. Mikšić Trontl, M. Kralj, M. Jerčinović, C. Baehtz, A. Muecklich, V. Holý, N. Radić, J. Grenzer. *Self-assembly of Ge quantum dots on periodically corrugated Si surfaces*. Appl. Phys. Lett. 107, 203101 (2015).

4. **M. Buljan**, N. Radić, J. Sancho-Paramon, V. Janicki, J. Grenzer, I. Bogdanović-Radović, Z. Siketić, M. Ivanda, A. Utrobičić, R. Hübner, R. Weidauer, V. Valeš, J. Endres, T. Car, M. Jerčinović, J. Roško, S. Bernstorff, V. Holy,

Production of three-dimensional quantum dot lattice of Ge/Si core–shell quantum dots and Si/Ge layers in an alumina glass matrix. Nanotechnology 26, 065602, (2015)

5. **M. Buljan**, M. Jerčinović, Z. Siketić, I. Bogdanović-Radović, I. Delač, M. Kralj, M. Ivanda, A. Turković, G. Dražić, S. Bernstorff, N. Radić, *Tuning the growth properties of Ge quantum dot lattices in amorphous oxides by matrix type,* J. Appl. Cryst. 46, 1490-1500 (2013).

Acknowledgments

I would like to thank my supervisor dr.sc. Maja Buljan, for the opportunity to work on this thesis, for all the comments, discussions and help that really contributed to this dissertation.

I am thankful for all my colleagues and collaborators dr.sc. Krešimir Salamon, dr.sc. Jordi Sancho-Parramon, dr.sc. Iva Šarić, dr.sc. Boris Okorn, dr.sc. Ana Šantić, dr.sc. Marko Jerčinović, dr. sc. Sigrid Bernstorff, dr.sc. Ivančica Bogdanović-Radović, dr.sc. Zdravko Siketić, dr.sc. Ida Delač Marion, dr.sc. Mile Ivanda, dr.sc. Branko Šantić, dr.sc. Tihomir Car that invested their time to help or perform measurements that contributed to this work, or helped with their insight to data interpretation. I am grateful for the collaboration with dr. Jörg Grenzer and dr. Rene Hübner that enabled me to come and visit HZDR Institute, as well as the collaboration with dr. Katerina Dohnalova for the opportunity to visit the University of Amsterdam.

Special thanks goes to my office roommate Lovro Basioli for all useful and useless discussions, laughs, support, help and company. Thank you to our technician Joško Erceg for all the sample depositions and all other small, but important things, and the rest of our team Dario Mičetić, Marija Tkalčević, and Ivan Mihoković.

Big thank you to my friends Tihana, Benjamin, Marija, Petra, Gorana, Ana, and Ivan for the friendship, understanding and encouragement throughout the years.

Words cannot express the thanks that some people deserve. My greatest gratitude goes to my mother Ivanka that was always my biggest support. A close second goes to Roman. Thank you for making me laugh, expanding my boundaries, and motivating me to always give my best.

Self-assembled Ge/Si core/shell quantum dots in alumina matrix for application in photo-electric conversion

NIKOLINA NEKIĆ

Ruđer Bošković Institute, Zagreb

Semiconductor materials confined in one or more dimensions exhibit special properties due to the quantum confinement effect. When confined in all three dimensions, a quantum dot (QD) is formed. Because of the confinement, energies of the QDs are discrete and depend on the QD size, enabling control of the absorption. Core/shell structures are somewhat more complicated but have several advantages over the regular core-only QDs. The shell could be used as a core passivation, a protective layer that reduces core oxidation and could increase the charge carrier lifetime, depending on band alignment.

This dissertation presents the experimental realization of Ge/Si core/shell quantum dots differing by the size of the core and shell and their optical properties. The material consists of Ge/Si core/shell self-assembled quantum dots produced by a simple magnetron sputter deposition of the $Ge/Si/Al_2O_3$ multilayer. Such QDs are uniform in size and ordered in a three-dimensional body-centered tetragonal QD-lattice within Al_2O_3 matrix. Different deposition parameters were used and their influence on the structure and electrical properties were investigated. Optical properties of the Ge/Si core/shell quantum dots are shown to significantly differ from the properties of pure Ge quantum dots. Influence of the matrix type on growth and assembly of QDs was studied. For that purpose, Ge QDs in silicon carbide and nitride were made. Considering that Ge oxidation is a serious problem in thin films with Ge QDs embedded in oxide matrices, we have shown that SiC and Si_3N_4 represent a good alternative to reduce the oxidation. However, from the studied samples, the ones with a silicon shell around the core are the best solution. After a detailed analysis of the structure, electrical transport in the films was

studied. All thin films have shown a significant current increase under illumination, which suggests a potential application in photodetectors.

(100 pages, 49 figures, 5 tables, 92 references, original in English)

Table of contents

1. INTRODUCTION

Nanostructures are known to have different properties than corresponding bulk materials because of the size effect. Depending on the number of confined dimensions, we distinguish quantum wells that are confined in one dimension, therefore becoming two dimensional (2D), quantum wires (1D) and quantum dots (0D).

In literature, the term nanoparticle is used for particles of sizes ranging from a few nanometers to even a few hundreds of nanometers. But only nanoparticles with sizes less than the exciton Bohr radius are called quantum dots (QDs). Quantum dots are sometimes also called "artificial atoms", because of their discrete energy states that resemble the energy levels of an atom. Due to the effect called quantum confinement, bandgap tuning is possible and change of an indirect bandgap toward a direct one. [1] Furthermore, their discrete states enable efficient generation of more than one electron-hole pair per absorbed photon, by multiple exciton generation. [2–4] This results in superior properties, like the enhancement of absorption and photocurrent with respect to the corresponding bulk materials. Therefore, changing their size, density, shape, and crystallinity leads to different properties, enabling a variety of applications. [5,6]

Germanium and silicon both represent materials frequently used in the electronic industry and are already used for solar cells, photodetectors, etc. But the goal is, as always, to reduce the production cost and increase efficiency. That is, new materials and structures are wanted that expand the spectrum of absorption, minimize the thickness of semiconductor needed to absorb light completely and amplify the signal. If possible, these materials should be compatible with silicon electronics and have the possibility for upscaling, in order to facilitate the transition from laboratory production to the industry. Nanomaterials based on germanium and silicon could be the solution to that problem.

A lot of techniques for the production of semiconductor QDs have emerged in the last few decades: colloidal synthesis, [7] ion implantation, [8–10] plasma-enhanced chemical vapor deposition (PECVD), [11–13] sol-gel, [14–16] molecular beam epitaxy (MBE), [17,18] etc. This work will demonstrate the magnetron sputtering technique as a tool for the production of self-assembled Ge-based QDs, with the possibility to tune QD properties by varying the deposition parameters. This technique represents a quick and simple way of obtaining QDs.

Silicon QDs embedded in SiO_2 matrix were studied in the context of producing an "all-silicon" solar cell, [19] as a QD-only solar cell and as a tandem cell where QDs are on top of a silicon cell.[20] Heterojunctions between Si QDs in oxide and carbide matrix with Si wafers have been made to demonstrate carrier types, [21] but these materials had no photovoltaic behavior directly in the QD-layers. Although there have been some indications on doping of Si QDs and rectifying behavior was accomplished, this behavior is not well understood and such devices are difficult to optimize in terms of voltage and current output.

Germanium QD systems have had their share of attention, as well. [9,22–25] Having a larger Bohr radius, Ge QDs are easier to achieve than the Si QDs. Compared to Si QDs that require much higher temperatures (1000 – 1100 °C), Ge QDs can be produced using lower temperatures of about 300-400 °C, [16] which results in lower production costs. Despite this interest for structural and optical properties of Si and Ge NCs in SiO_2, until recently only a few studies have addressed photodetector (PD) devices based on these materials. [11,22,26,27] Various Ge QD-based devices showed impressing spectral response and internal quantum efficiency. [28,29]

However, being embedded in an oxide matrix, these materials have a well-known problem of Ge oxidation, especially after the annealing to high temperatures necessary for the Ge QDs to crystallize. To avoid the oxidation Si_3N_4 matrix is sometimes used. [30]

In order to use silicon and germanium nanomaterial advantages and to avoid the germanium oxidation, we combine them into a core/shell structure. Core/shell QDs are specific for their electronic states. Ge-core/Si-shell QDs have a type II band alignment, causing electrons to localize in the shell, and holes in the core. [31] As a result, free charge carriers are separated and exciton lifetime is enhanced. [32,33] The effective band gap can be size-tuned, but the dependence on the size is not as simple as it is for one-material quantum dots. Nevertheless, theoretically calculated absorption of such materials is very high.

In the recent years, there have been several theoretical papers about energy levels and optical properties of Ge/Si core/shell nanocrystals, [31–34] but to our knowledge, no experimental work on this system has been published. In this thesis, the production process for the QDs is described and a detailed structural characterization of these materials is provided. The achieved self-assembly of the Ge/Si nanoparticles is especially important because it represents a simple, single step production recipe, which results in an ordered QD superlattice. The quantum confinement effect in Ge/Si core/shell nanoparticles embedded in alumina matrix is investigated. A strong influence of the core and shell size on optical properties, as well as the

ordering of the quantum dots, has been observed. Starting from that, this work is based on investigating the influence of the deposition parameters on QD structure, as well as discovering how the structure changes the other properties relevant for application, such as absorption, transport and photocurrent.

2. THEORY

With the development and improvement of different growth techniques (Molecular beam epitaxy, Plasma enhanced chemical vapor deposition (PECVD), magnetron sputtering…) and characterization methods such as transmission electron microscopy (TEM), various "quantum structures" became a part of the investigation. This progress made it possible to reduce the effective dimension from a three dimensional bulk to 2D quantum wells, 1D dimensional nanowires and even quasi-0D quantum dots. This confinement in some, or all dimensions, causes a very interesting modification in their electronic and optical properties, which makes such structures promising for many possible applications in microelectronics, nonlinear optics and photovoltaics. [35]

2.1. Quantum confinement

Light absorption in semiconductors leads to the excitation of electron from the valence band to the conduction band, leaving a hole in the valence band. Depending on the excitation conditions the Coulomb attraction between an electron and a hole might lead to a bound state, the Wannier exciton. The mean free path for the exciton relative motion is the exciton Bohr radius, which is usually 1-20 nm, depending on the material. Quantum confinement effect appears when the material is confined in one or more dimensions to the size comparable to exciton Bohr radius, thus constraining charge carriers in a potential well in one or more directions, which causes the quantization of energies. The structures confined in one, two or three dimensions are called quantum wells, quantum wires, and quantum dots respectively (**Figure 1**). Because of the quantized energy levels, quantum dots are often called "artificial atoms".
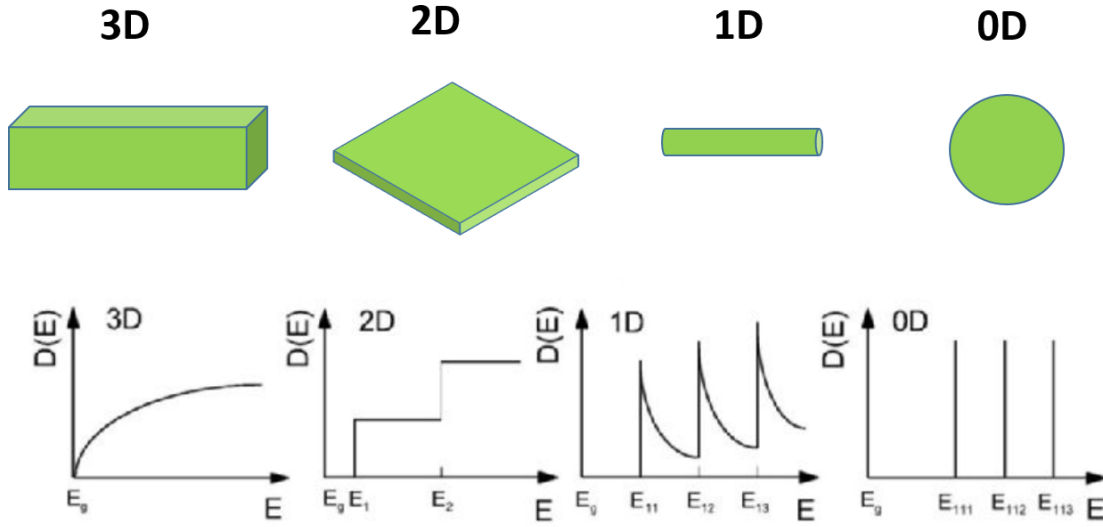
Figure 1. The effect of the confinement on the density of states. For QDs the density of states is a series of delta functions. Density of states graph taken from Ref. 36.

Quantum dots

Quantum dot is a nanometer-sized semiconductor particle, which confines the electron-hole pair in all three dimensions. Therefore, we can approximate the problem to the electron in a spherical box. This simple model can explain the basic optical properties of QD materials.

Consider an electron of mass m_0 inside a spherical potential well of radius R:

$$V(r) = \begin{cases} 0, & r \leq R \\ \infty, & r > R \end{cases}.$$
(1)

Solving the Schrödinger equation gives the wavefunctions: [37]

$$\Phi(r, \theta, \phi) = C \frac{j_l(k_{n,l}r) \, Y_l^m(\theta, \phi)}{r}.$$
(2)

C is a normalization constant, $Y_l^m(\theta, \phi)$ is a spherical harmonic, $j_l(k_{n,l}r)$ is the lth order spherical Bessel function and

$$k_{n,l} = \frac{\alpha_{n,l}}{R},$$
(3)

where $\alpha_{n,l}$ is the nth root of the Bessel function. Electronic energy levels of the particle is then:

$$E_{n,l} = \frac{\hbar^2 k_{n,l}^2}{2m_0} = \frac{\hbar^2 \alpha_{n,l}^2}{2m_0 R^2}.$$
(4)

Note that the energies are strongly dependent on the sphere size R, in the way that in a larger sphere, the electron has a lower energy. Also, the energies described are identical to the kinetic energy of a free particle, apart from the wavevector being quantized by the spherical boundary condition. So it may not be clear at first how this model can describe quantum dot behavior, where we have an electron in a semiconductor dot filled with atoms, and not a free particle confined to an empty sphere.
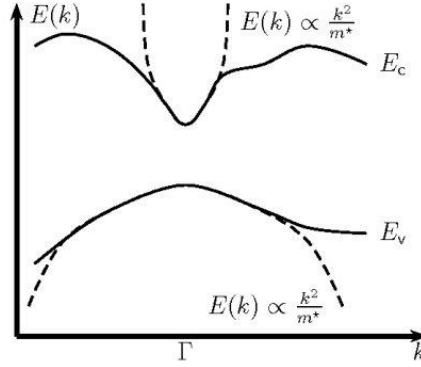

Figure 2. Schematic illustration of the effective mass approximation. The bands are assumed to have parabolic forms in the minimum of the conduction and maximum of the valence band. Taken from Ref. 38.

In order to reduce the quantum dot problem to the "particle in a sphere" form, let us start with the *effective mass approximation.* Bulk conduction and valence band are assumed to have simple parabolic forms near the extremes in the band diagram (**Figure 2**). The carriers behave as free particles with an *effective mass* $m_{eff}^{c,v}$, which accounts for the curvature of conduction and valence bands. With respect to the semiconductor band gap E_g, the energies of the conduction and valence bands are then: [39]

$$E_k^c = \frac{\hbar^2 k^2}{2m_{eff}^c} + E_g \ ,$$

$$E_k^v = -\frac{\hbar^2 k^2}{2m_{eff}^v} \ .$$

(5)

Physically, the effective mass includes the complicated periodic potential of the lattice. That way, we can completely ignore semiconductor atoms in the lattice and treat the electron and hole as free particles. Moreover, when the dot diameter is much larger than the lattice constant of the semiconductor, quantum dot can be treated as a bulk sample. This approximation is called the *envelope function approximation.*

Still, one more thing has to be taken into account. This treatment completely ignores Coulombic attraction between electrons and holes, which creates an exciton. Neglecting this term could be justified by a third approximation, the *strong confinement approximation*, which will be discussed further in the next section.

Another thing to consider is the depth of the potential well. We assumed that the potential is infinite outside the QD, which means the radial part of the wave function must be zero at the boundary $r = R$. In reality, this is not the case and the question is, what happens for a finitely deep well, when the wavefunctions 'leak' through the boundaries of the QD radius?

For a surrounding material with a high enough band gap, the confinement will be strong enough to be described with the model above. On the other hand, when the potential well is shallow, i.e. $V_0 < (\pi\hbar)^2/2m(2R)^2$, no bound state will exist. [40] This needs to be kept in mind when choosing the barrier materials.

Quantum confinement regimes

Energy levels in a quantum dot will depend on the strength of quantum confinement effect (potential barrier height) and Coulomb interaction between electrons and holes. Depending on the interplay of those two effects, two extreme cases can occur: the *strong* and *weak quantum confinement* regimes, with the *intermediate confinement* in between. [40]

For small QDs a *strong confinement* regime occurs. To be more precise, we consider QDs with a radius R smaller than the exciton Bohr radius a_X, but larger than the crystal lattice constant a_L (so that the effective mass approximation is still valid):

$$a_L \ll R \ll a_X . \qquad (6)$$

In this regime, the influence of the Coulomb interaction is considered smaller than the confinement effect and, in a rough approximation, Coulomb interaction can be neglected. Since the confinement energy of each carrier scales as $1/R^2$ (Eq. (4)), while the Coulomb interaction scales as $1/R$, in sufficiently small dots the quadratic confinement term dominates. Therefore, the electron and hole are treated independently and each is described as a "particle-in-a-sphere". Finally, this yields a simplified equation for a QD band gap: [41]

$$E_g(D) = E_g(\infty) + \frac{A}{D^2} eV \cdot nm^2, \qquad (7)$$

where $E_g(\infty)$ is the bulk band gap, D is the QD diameter, while the confinement parameter $A = \pi\hbar/2m^*$ depends on the exciton effective mass m^*.

When the radius of the QD is several times as large as the exciton Bohr radius, the *weak quantum confinement* is in order. For those cases, the excitonic effects dominate and the confinement only causes the quantization of the kinetic energy of the exciton center-of-mass motion.

It is possible to obtain the material in the desired regime by tailoring the size of the QDs, but the properties can also be tailored by changing the thickness of the spacing layers, or changing the matrix material and therefore the barrier height and strength of quantum confinement, while annealing can be used to obtain crystalline structures or to reduce the defects.

In a real dielectric matrix with a finite barrier height V_0, value of E_g given by Eq. (7) is reduced by the factor $\left[1 + \frac{\hbar}{R\sqrt{2m^*V_0}}\right]^2$. [27] Therefore, this will have to be taken into account when considering the QDs in matrices with a lower energy gap, such as silicon nitride and silicon carbide.

Core/Shell QDs

In order to passivate surface states an additional layer of the distinct semiconductors can be grown around the initial QD. [42] Such nanostructures are called core/shell QDs. Theoretical calculations show that the shell can significantly influence the optoelectronic properties, therefore making these structures even more interesting.

Depending on material combination and the position of their conduction and valence band energies, there are two possible cases: type I and type II band alignment (**Figure 3**). [43]

In type I band alignment, the band gap of one material entirely overlaps that of the other. This causes both carrier types to localize in one material. The example of such a hetero-structure is CdSe/CdS, in which the CdS bandgap completely overlaps the bandgap of CdSe. As a result, the probability of recombination is higher, consequently those materials are used for building light emitting devices.

Type II band alignment, on the other hand, causes separation of electrons and holes, thus localizing the electrons in the shell and holes in the core for Ge/Si nanoparticles. Such properties represent an advantage in photovoltaic applications, because of a smaller electron-hole recombination probability.
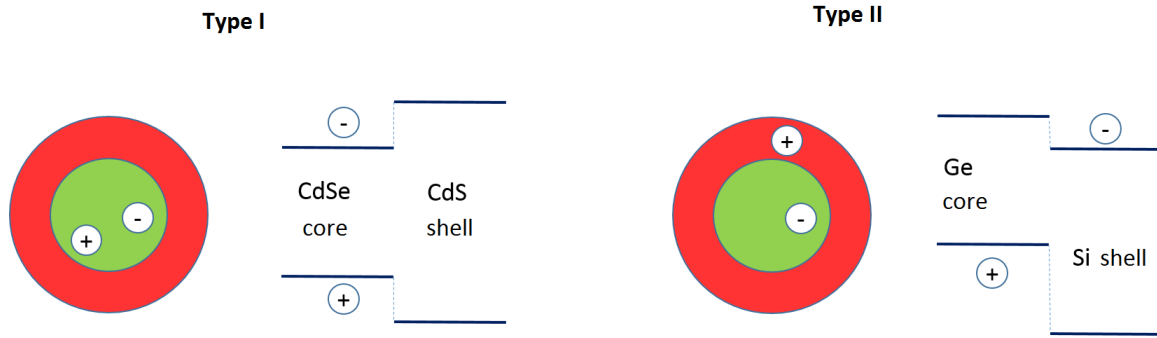
Figure 3. (a) Type I band alignment is shown on the example of CdSe-core/CdS-shell, where both electron and holes are localized in the core. The oposite situation where the core and shell materials are switched and both carriers are localized in the shell also represent type I alignment. (b) Type II band alignment for the Ge-core/Si-shell QD. Electrons are localized in the shell, while the holes are separated to the core.

2.2. Quantum dot formation and self-assembly

In order to be able to control the QD size and shape, it is important to understand the mechanisms of a self-assembled quantum dot growth. Well known mechanisms of self-organization on a crystal surface, such as Stranski–Krastanov or Volmer–Weber growth, are driven by misfit of the lattice constants of a growing layer and the layer below it. This results with a strain in the growing layer and nanocrystal formation. However, in the case of an amorphous surface, the self-assembly is achieved by nucleation combined with the influence of surface morphology. Principles of self-assembly in our system were explained with a model that was experimentally confirmed already for the Ge QDs in silica, [44,45] alumina, [24,46] and a mullite matrix. [47]

The model combines two mechanisms: diffusion assisted nucleation and enhanced nucleation probability in the troughs of the previous layer. [48]

The mechanism of diffusion assisted nucleation assumes that nucleation is caused by the diffusion properties of atoms coming to the surface during the deposition process. Since substrate temperature is usually above 300 °C during the deposition, surface diffusion of atoms is stimulated by the elevated temperature. When a point on the surface has a critical concentration of germanium atoms, nucleation of a nanoparticle begins. Such a cluster is less mobile, so it continues to grow, while the concentration of Ge atoms around it is decreased and

new nucleation in that area is less likely. This causes the correlation in distance between the nanoparticles in one layer but does not influence the inter-layer ordering.

In order to explain the interlayer assembly, we need to include the second mechanism that is based on surface morphology. This mechanism uses the assumption that the nucleation probability is increased in troughs on the surface and is crucial for reaching the self-assembly.

So after the first bilayer deposition of alumina and germanium, germanium nanoparticles are formed due to the diffusion dynamics. In the second bilayer deposition, alumina covers the formed nanoparticles, after which the second layer of germanium will nucleate in the troughs with a higher probability. This way the degree of spatial disorder is reduced in each subsequent layer.

However, if only the second mechanism was active, every new layer would have more and more quantum dots. The surface we are considering has more troughs than there are QDs in the layer underneath. This would cause more QDs reduced in size with every layer. But the first mechanism does not allow this, demanding the same diffusion and nucleation properties in all layers, resulting in the constant number and size of the QDs in each layer. STEM (*Scanning Transmission Electron Microscopy*) analysis has confirmed that above every nanoparticle a hill is formed and between them the valleys that represent the preferred nucleation sites in the next layer. QDs form only in the valleys that are in accordance with the first mechanism. Previously deposited layers influence the surface morphology of the current layer, therefore inducing ABAB or ABCABC stacking, depending on the matrix. The matrix surface properties determine the type of the paracrystal lattice (FCC or BCT) by influencing the vertical stacking. In Al_2O_3 matrix layers are stacked in ABAB configuration. Alumina has a property of smoothing the surface, so that only the previous layer influences the growth, resulting in a BCT (body-centered tetragonal) lattice of nanoparticles. In the SiO_2 matrix the two previous layers influence the nanoparticle nucleation place, so ABCABC stacking (FCC lattice) occurs. Even though the starting distribution of the nanoparticles is similar in different matrices due to the isotropic surface, the vertical stacking will differ depending on the matrix "smoothing" ability.

Monte Carlo simulation of nucleation and inlayer growth of nanoparticles has confirmed the self-organization based on the two mentioned mechanisms.[48] Surface and diffusion of the first layer is assumed to be isotropic and is hence treated as a disordered 2D hexagonal lattice, because of diffusion kinetics (Vornoi cells) on the isotropic surfaces. The first deposited layer of matrix that erases the morphology of the substrate makes this assumption plausible.

After a few deposited layers, with the matrix layer deposited last, hills exist above each formed QD. The surface shape at the interface layer j_3 depends on the positions of the nanoparticles in the layer below $j_3 - 1$, and if it is the case of SiO_2 matrix, even one more layer beneath $j_3 - 2$. Therefore, the morphology of the j_3 layer is given with the expression:

$$h_{j_3}(\boldsymbol{x}) = \sum_{j_1,j_2} \left[f\left(\boldsymbol{x} - \boldsymbol{X}_{j_1,j_2,j_3-1}\right) + C f\left(\boldsymbol{x} - \boldsymbol{X}_{j_1,j_2,j_3-2}\right) \right],$$

$$f(\boldsymbol{x}) = \exp\left(-\frac{|\boldsymbol{x}|^2}{b^2}\right), \qquad \boldsymbol{x} = (x,y),$$

(8)

where a 2D Gaussian-type function $f(\boldsymbol{x})$ is assumed for the shape of the hills, $\boldsymbol{x}$ is the position vector in the current layer, $\boldsymbol{X}_{j_1,j_2,j_3-1}$ and $\boldsymbol{X}_{j_1,j_2,j_3-2}$ are vector positions of the QDs with indices j_1 and j_2 buried in the layers $j_3 - 1$ and $j_3 - 2$, while b is the parameter that defines the width of the dots and C is the "inheritance factor" that describes the influence of the layer $j_3 - 2$ on the j_3 layer morphology. Simulation and experiment with Al_2O_3 matrix have a much better agreement with a C value much smaller compared to the SiO_2 matrix, where considerably higher C is required. [49] This is consistent with the experimental results that the hills above the buried QDs are smaller in alumina than in silica. Therefore, the conclusion that the alumina matrix smoothens a surface is valid.

Simulation results for the Al_2O_3 matrix are shown in **Figure 4** (a) and it shows that in-layer arrangement of nanoparticles changes from the distorted 2D hexagonal lattice, assumed in the first layer, to the distorted quadratic lattice in the higher layers. The reason for this is explained in **Figure 4** (c). For a relatively well ordered starting 2D lattice, with a standard deviation from the ideal position being $\sigma = 0.15$, six minima will form above each nanoparticle in the next layer. In the case of a higher disorder ($\sigma = 0.30$), some of the six minima are overlapping, or are really close to each other, so the correlation number is decreasing from six to four, because only one nanoparticle can form inside the two close minima. This will happen only for a small C factor in the expression (8), when the influence of the previous layers is not that strong, besides the one immediately beneath. If such smoothing is present, ABAB stacking of the layers occurs, resulting in a 3D BCT quantum dot lattice.
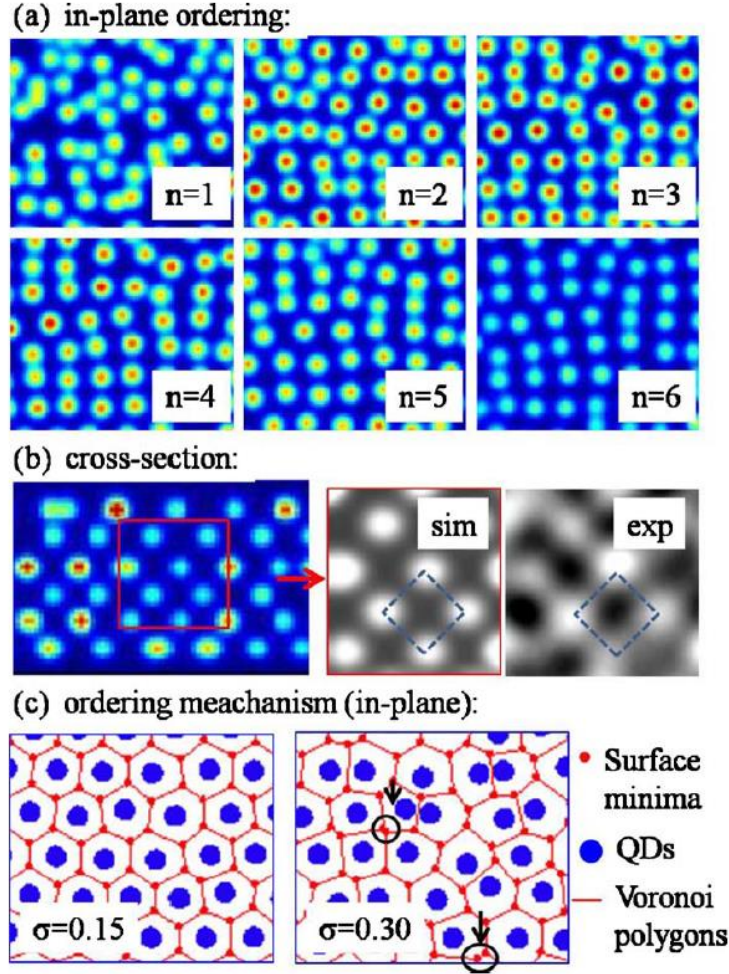
Figure 4. Monte Carlo simulations for the BCT lattice (Al$_2$O$_3$ matrix), taken from Ref. 49. (a) Enhancement of in-plane ordering of QDs with the increasing number of layer n, (b) Comparison of simulation and experimentally measured cross-sectional positions by TEM, (c) a well ordered 2D hexagonal lattice, with a small relative standard deviation from the ideal positions ($\sigma = 0.15$) will have six minima in the layer above it, while a lattice with $\sigma = 0.30$ has a lot of minima overlapping or very close to each other, which results with a 2D quadratic lattice after a few layers.

To summarize, the alumina matrix smoothens the surface resulting in a BCT lattice, which is more stable than the FCC-like one observed in silica. The ordering increases with the number of layers for the alumina matrix, while in silica stacking can change from ABCABC to ABAB and back, hence deteriorating the ordering quality. Monte Carlo simulations agree well with the experiments, confirming the validity of the presumed models of growth. This was also confirmed recently by Endres et al., where even more detailed simulations were made. [50]

2.3. Current conduction mechanisms

Before attempting to make special devices such as detectors or solar cells, it is important to investigate the electrical properties of thin films and to understand the possible transport mechanisms.

Since the thin films under investigation are constructed out of semiconductor QDs embedded in an amorphous dielectric matrix, let us first consider the types of conduction mechanisms in dielectric films: electrode-limited conduction mechanisms and bulk-limited conduction mechanisms. The electrode-limited conduction mechanisms, like their name suggested, depend on the electrical properties at the electrode-dielectric contact. They include Schottky emission, Fowler-Nordheim tunneling, direct tunneling and thermionic-field emission. [51]

The bulk-limited conduction mechanisms depend only on the properties of the dielectric itself. Bulk-limited conduction mechanisms are ohmic conduction, hopping conduction, space-charge-limited conduction, ionic conduction, Poole-Frenkel emission, and grain-boundary-limited conduction. Ohmic conduction is generally caused by the movement of mobile carriers in the corresponding band and a linear relationship between the current density and the electric field exists. Although dielectrics have a large energy band gap, there is still a small number of carriers that may be generated due to the thermal excitation. This current mechanism in dielectrics is observed if there is no significant contribution from other transport mechanisms, usually at very low voltages. Since in this research hopping conduction and space charge limited current model are the most relevant, a more detailed explanation is given in the following sections.

Hopping conduction

Hopping conduction occurs when electrons trapped in dielectric films tunnel through, that is, "hop" from one trap site to another. Hopping conduction is a tunneling effect, which means that the carriers have energy lower than the maximum energy of the potential barrier between the trapping sites, but the barrier is thin enough to allow tunneling. Schematic energy band diagram of hopping conduction in a MIS device, similar to devices that will be used later in experiment, is shown in **Figure 5**. Current of electrons jumping a distance a_h in the direction of the field E is given by expression [51,52]:

$$J = qva_h n \exp\left[\frac{qa_h E}{kT} - \frac{E_a}{kT} - 2\alpha a_h\right], \tag{9}$$

where q is the electronic charge, ν is the frequency of thermal vibration of electrons at trap sites, a_h denotes the mean hopping distance, n is the electron concentration in the conduction band of the dielectric, E is the electric field, and E_a is the activation energy. The term $\exp(-2\alpha a_h)$ is the factor depending on the overlap of the wavefunctions, where $\alpha = \sqrt{2m_e E_a}/\hbar$ and m_e is the electron mass. Activation energy is defined as the energy required to move the electron from the trap states to the bottom of the conduction band E_C. In the experiment, we apply voltage U between the two electrodes on the metal and the semiconductor, and assume that $E = U/d$, where d is the thickness of the thin insulator film. Using Eq. (9) mean hopping distance can easily be extracted from the slope of the $\ln(J) - E$ graph, since the slope is equal to qa_h/kT.
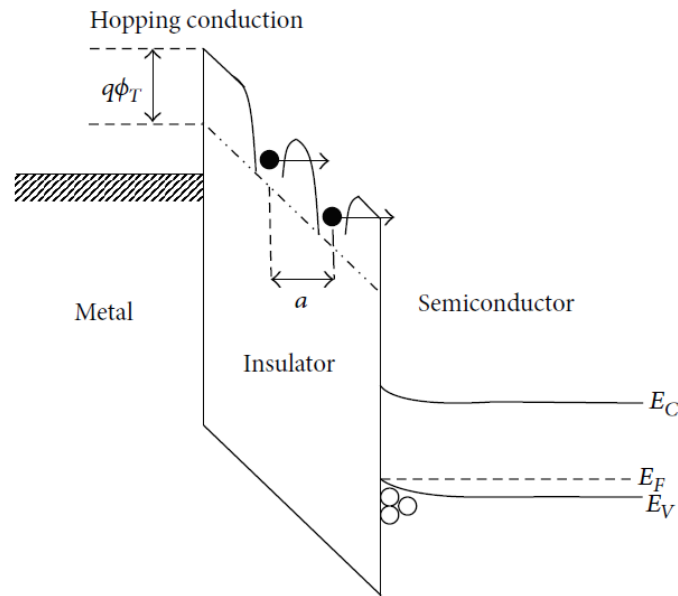

Figure 5. Energy band diagram of a metal-insulator-semiconductor with a hopping conduction, under external electric field E. Taken from Ref. 51.

One of the conduction mechanisms in Ge QDs embedded in an insulator (or a wide bandgap semiconductor) matrix could be hopping conduction. QDs and surface states represent electron trap sites in the insulator, which contribute to conduction. However, the type of conduction depends strongly on the barrier thickness and height. For a higher barrier distance, tunneling probability is decreasing, therefore causing other charge transport mechanisms to take over.

Space Charge Limited Current model

Space charge limited current regime represents the limit in which the current is dominated by the charge carriers injected from the contact. This happens, for example, when an undoped

semiconductor with a large energy gap is connected to a high current source, or a high voltage. The charge carrier concentration injected from the electrode can be much higher than the concentration in the neutral semiconductor. Hence, the space charge distribution will affect the electric field distribution between the electrodes.

The transition from the ohmic to the space-charge limited region occurs at the critical voltage labeled U_{tr}. If the applied voltage is smaller than U_{tr}, then the injected carrier density is small compared to the concentration of the free charge carriers in thermal equilibrium. This causes the injected carriers to redistribute to maintain charge neutrality, also known as dielectric relaxation. Thus, the injected carriers do not have the chance to travel across the insulator. On the other hand, for the voltage $U > U_{tr}$, the injected excess carriers dominate the thermally generated carriers, the traps are filled up and a space charge appears. The traps-filled limit current is defined as: [51]

$$J_{TFL} = \frac{9}{8}\mu\varepsilon\theta\frac{U^2}{d^3},$$ (10)

where d is the thickness of the thin insulator film, ε static dielectric constant, θ is the ratio of the free carrier density to total carrier density and μ is the carrier mobility.

At some point, the increase of applied voltage may increase the density of free carriers resulting from injection to such a value that the Fermi level moves up above the electron trapping level. After all the traps are filled up, at the trap-filled limit voltage U_{TFL}, all subsequently injected carriers move free in the dielectric film, causing the rapid jump in current. Hence, in the case of a very strong injection, traps are filled, a space charge layer builds up, the electric field is no longer constant and the conduction becomes space-charge limited. Above this threshold voltage U_{TFL}, the space charge limits the further injection of free carriers in the dielectric, resulting in a square dependence of the current called Mott-Gurney's law: [51]

$$J_{MG} = \frac{9}{8}\mu\varepsilon\frac{U^2}{d^3}.$$ (11)

A typical $J - U$ characteristic for space-charge-limited current plotted in a log-log curve is shown in **Figure 6**. The plot clearly shows three limited curves, Ohm's law, traps-filled limit current and Mott-Gurney's law.
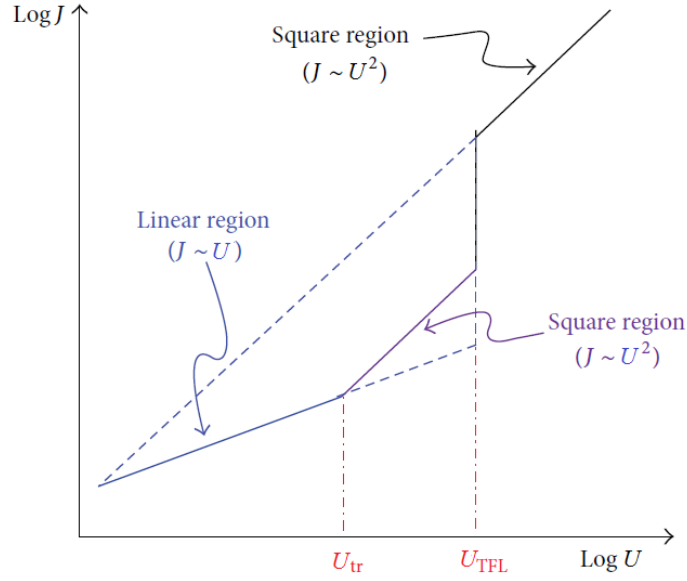
Figure 6. Log-log $J - U$ characteristic for space-charge-limited current. Three regimes are visible: the linear Ohmic regime, trap-filled limited square regime and the SCLC regime. Figure is taken from Ref. 51.

Conductivity temperature dependence

As we already mentioned, there are a number of mechanisms that may contribute to the conduction current through the film at the same time. Several conduction mechanisms depend on the temperature in different ways. Therefore, measuring the conductivity temperature dependence could offer a way to distinguish conduction mechanisms.

Hopping conduction is represented by an exponential temperature dependent conductivity given by: [53]

$$\sigma = \sigma_0 \exp\left[\frac{A}{T}\right]^{1/q}, \tag{12}$$

where σ_0, A and q are constants. A hopping electron always tries to find the shortest hopping distance and the lowest activation energy. Both conditions cannot always be satisfied at the same time. When hopping occurs between nearest neighbor localized states, the process is characterized by $q = 1$. This is known as *nearest neighbor hopping*. However, at low temperature the most frequent hopping is not to the nearest neighbor. A conduction mechanism dominated by Mott's *variable range hopping*, that is hopping between localized states distributed randomly in the film, a temperature dependence is characterized with $q = 4$ for a

3D system and $q = 3$ for 2D. At even lower temperatures usually Coulomb interactions start playing an important role and for that case $q = 2$.

Usually, for higher temperature regimes of hopping conduction, where the nearest neighbor hopping is most favored, the temperature dependence of the conductance starts to follow Arrhenius behavior: [54]

$$\sigma = \sigma_0 \exp(E_A/kT), \qquad (13)$$

where k is the Boltzmann constant, T temperature and E_A activation energy. Arrhenius behavior is observed when there is a conduction barrier that needs to be overcome for transport, and it is said that conductivity is simply activated with temperature. For disordered materials, but also in arrays of quantum dots, Arrhenius temperature dependence suggests a hopping mechanism for transport. [55,56] The same is obtained from Eq. (9) that states if localization is very strong, an electron will normally jump to the nearest state in space, because the term $\exp(-2\alpha a_h)$ falls off rapidly with distance. [52]

From photo-electric conversion to application

In semiconductor materials, conversion of light into an electric current works on the principle of electron-hole creation under illumination. When a semiconductor is illuminated with photons that have the same or greater energy than the semiconductor bandgap, photons are absorbed and electron-hole pairs created. These free carriers, electrons in the conduction band and holes in the valence band, are able to travel across the crystal under the influence of an intrinsic or externally applied electric field. The separation of electron-hole pairs generated by the absorption of light creates a *photocurrent*. The photocurrent is, therefore, a fraction of the photogenerated free charge carriers collected at the electrodes and is an increasing function of the incident light intensity. Based on the nature of the charge separation, we can distinguish between two categories of devices: *photoconductors*, where the electric field leading to the collection of charge carriers is provided by applying a bias voltage, and *photovoltaics*, which have an internal electric field, most often achieved with a p-n or a Schottky junction.[57] Both photoconductors and photovoltaics can be used as photodetectors, but only photovoltaics can operate as solar cells, as well.

Although the structure can be much more complicated with QD-materials, basic physics is the same. In order to have a good photovoltaic, it is important to have an intrinsic field, strong enough to ensure charge separation and a low recombination probability to enhance the

efficiency of the device. In recent years, there were several ideas on how to achieve this with Si QDs or Ge QDs embedded in a wide-bandgap matrix. [20,58] Most of them are based on doping the QDs and creating a p-type and n-type QD-multilayers. However, QD doping mechanisms are still not completely understood. [59] Also, these structures showed limited performances due to the high defect density at the QD/matrix surface and a high series resistance. [60]

We tried doping the Ge QDs by using already doped Ge targets but failed to observe a p-n junction formation. This could be due to many different reasons. One of which is the observation by Zhang et al. that Ge nanocrystals in SiO_2 matrix exhibit a high p-type conductivity induced by surface states. [61] Their thin films were not intentionally doped, which indicated inherent hole generation in the structure. It is possible the same mechanism is present in our Ge QDs embedded in Al_2O_3, causing the layer we intended to be "n-type" doped, to be neutral, or even a p-type as well. For that reason, this problem required more research and time, and will be investigated, but is out of the scope of this thesis.

Photoconductors, on the other hand, do not need an intrinsic electric field and operate under the applied bias voltage. Therefore, our research took a slightly different direction in investigating the performance of Ge QD-based photodetectors.

The main point of interest in photoconducting device is its response coefficient R_i: [57]

$$I_{ph} = R_i P_{opt} \, , \tag{14}$$

which links the photocurrent I_{ph} to the incident light power P_{opt}. All our devices were measured under the same incident light power, so comparing photocurrents corresponds to comparing responsivities.

The other important parameter is detectivity, a figure of merit defined by the equation:

$$D = \frac{R_i}{I_b} \ [W^{-1}] \, , \tag{15}$$

where I_b is the noise current. For the metal-insulator-semiconductor (MIS)-like photodetectors, the dark current represents the noise current. [62]

3. EXPERIMENTAL METHODS

All thin films investigated in this work were made with magnetron sputtering deposition.

The ordering of the quantum dots, as well as core and shell sizes depending on the deposition parameters are investigated. GISAXS (Grazing incident small angle X-ray scattering) is used for structural characterization. Measurements were done on the synchrotron Elettra, Trieste. In combination with ToF-ERDA[1] (Time of flight- Elastic Recoil Detection Analysis), full information on quantum dot ordering and composition can be obtained.

Raman and XRD were used to investigate the crystallization after annealing and Spectroscopic ellipsometry for optical properties.

3.1. Magnetron sputtering deposition

Sputtering deposition is a physical vapor deposition method used to produce thin films by sputtering in high vacuum conditions. A material target that represents a source is ejected on the substrate, for example, a silicon wafer or a glass substrate. Unlike the thermal evaporation, the target does not require heating, which means that the sputtering deposition is a non-equilibrium thermodynamic process. This is a very important advantage of sputtering because it enables the co-deposition of some material mixtures that cannot be produced by usual equilibrium processes. When comparing the sputtering to evaporation, there are many more advantages: film properties can be controlled, more materials can be used, adhesion is better. Furthermore, the scalability of this method is an important advantage, because of the possibility to develop the deposition process in the laboratory and transfer it to the industry. It seems one of the main disadvantages is that the equipment is more expensive.

---

[1] TOF-ERDA is a spectroscopic method developed for measuring depth profiles and concentrations of elements in the unknown sample. Heavy ions (like Cl, I, Au..) with energies of 1 MeV/A are used for recoiling atoms from the target. Energy and time of flight of the recoiled atoms are measured in coincidence which enable the separation of elements by energy and mass. More detail can be found in Ref. 92.
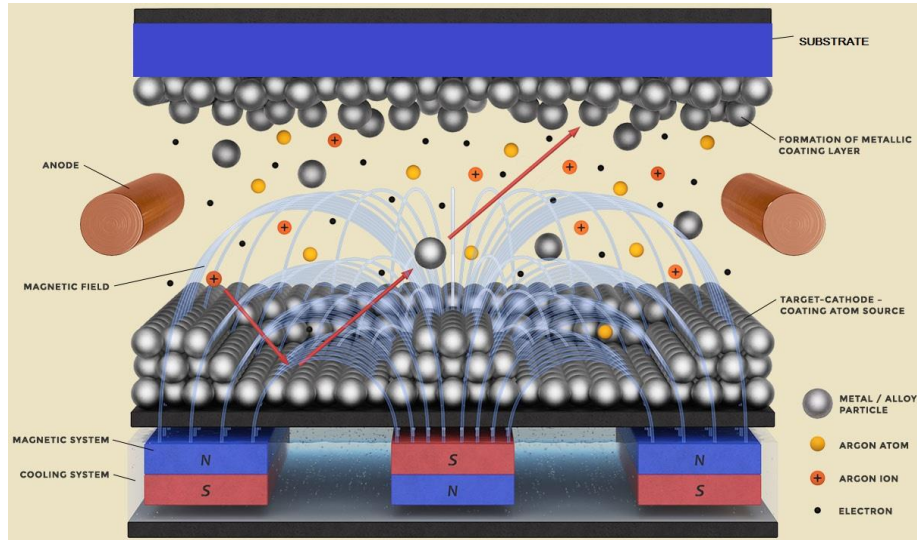
Figure 7. Magnetron sputtering scheme. The static magnetic field is used to contain the plasma near the surface and enhance the sputtering efficiency.

Typically, the target (a plate of the material to be deposited) is connected to a negative voltage supply. A noble gas (most commonly used is Ar) is introduced to the vacuum chamber under the pressure of 0.1 to 1 Pa, where it is ionized by setting up an electric discharge between the cathode (target) and anode, thus producing plasma. When the glow discharge is started, positive ions get accelerated by the electric field and strike the target plate, remove neutral target atoms by momentum transfer and these condense into thin films. Electrons released during ionization are accelerated towards the anode, on their way colliding with gas atoms, creating new ions and electrons, thus maintaining the glow discharge. The target atom will be sputtered when the energy transfer perpendicular to the surface is greater than the binding energy. The sputter yield is the ratio of the number of emitted particles per incident particle. Deposition probability is the ratio of atoms actually deposited on the sample divided by the total number of atoms emitted from the cathode.

Sputtering sources often employ magnetrons that utilize strong electric and magnetic fields. The static magnetic field is located parallel to the cathode surface so that the secondary electrons which are emitted from the cathode due to ion bombardment are constrained **Figure 7**. The drift $\vec{E} \times \vec{B}$ causes electron currents to move parallel to the cathode surface, closing on themselves, in order to confine charged plasma particles close to the surface of the sputter target. This increases the percentage of electrons that take part in ionization events, thus increasing the ionization efficiency. Therefore, the ionization process is much more efficient than it would be without magnetron. Most common are magnetrons in planar or cylindrical

geometry, while in this work a commercial planar magnetron with a torus magnetic field was used.

Sputtering process can be run in DC or RF mode. DC sputtering cannot be used for depositing dielectrics because insulating cathode will cause charge build up during Ar^+ bombarding. Therefore, DC mode is used for sputtering metals and semiconductors, and RF mode for dielectrics.

Important process parameters are:

i) Working pressure ($\sim 3 - 5$ mTorr). The influence of the Ar pressure and substrate temperature on the structure of metal coatings is shown in **Figure 8**.

ii) Magnetron power ($10 - 300$ W). A sputtering system can be characterized by how fast it deposits a given film per watt of power used. By altering the magnetron power ($P = U \cdot I$), the deposition rate is changed. If the working pressure is kept constant, increasing the power increases the deposition rate.

iii) Substrate temperature (RT-500 °C). This is a very important parameter, especially for the nanoparticle growth. Increasing the temperature of the substrate causes enhanced surface diffusion of the deposited atoms, which enables the nanoparticle growth during the deposition process. On the other hand, higher temperatures could cause ripping off the already deposited atoms, that effectively reduces the deposition rate, but it depends on the material.
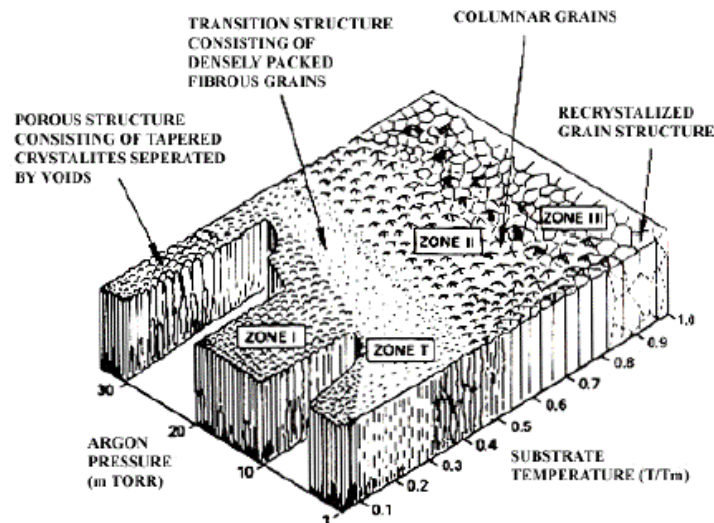

Figure 8. Structural zone models of sputtered metallic coatings depending on the substrate temperature divided by the melting temperature of the material and argon pressure. Taken from Ref. 63.

With magnetron sputtering it is possible to deposit a wide variety of metals, insulators, semiconductors, alloys, and composites. Thin films may be deposited by sputtering without high source temperatures, like it is required for evaporation, which is a great advantage. Also, another positive thing about this method is a reproducible deposition control – the same deposition rate for the same process parameters, so it is easy to control the film thickness via the deposition time.

For this thesis, *Multisource Magnetron Sputtering System CMS-18* from *Kurt J. Lesker Company* was used. Our sputtering system has four magnetrons, which means four targets could be used simultaneously. This could be used to produce alloys or mixtures of different materials by co-sputtering. In this thesis the sputtering system will be used for the production of multilayer thin films.
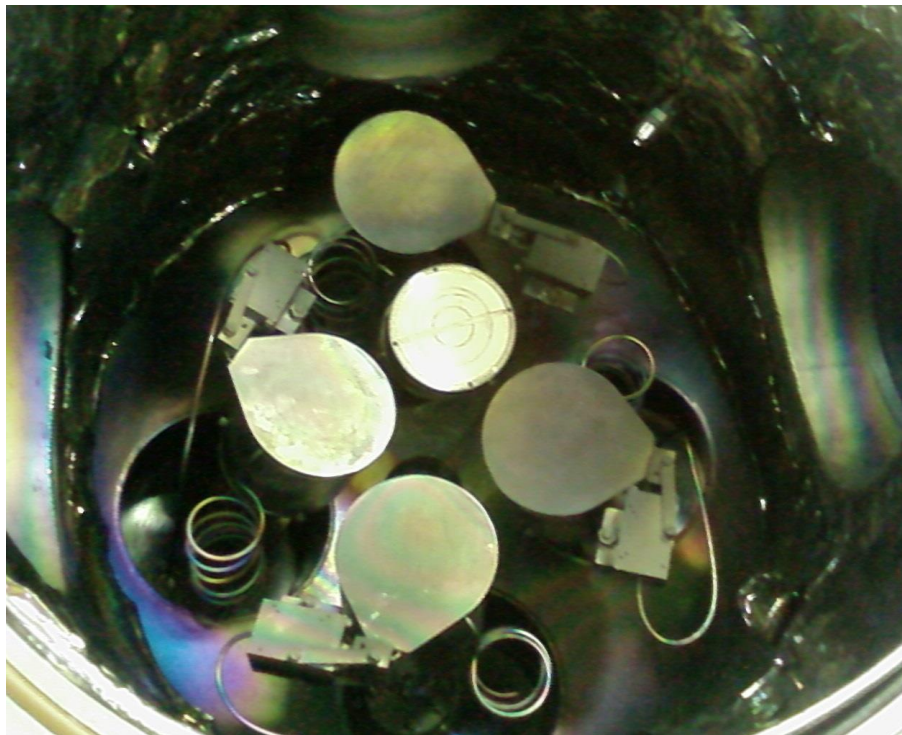

Figure 9. Magnetron sputtering chamber. Four magnetrons are shown, one without the lid has a gold target used mostly for the contact deposition. By moving the lids, we can control which material is deposited.

3.2. GISAXS (Grazing Incidence Small Angle X-Ray Scattering)

The appearance of nanostructures, thin films, and similar small-scale materials led to the development of many methods for their structural investigation, such as Transmission electron microscope (TEM), Scanning electron microscope (SEM), etc. However, diffraction of the Röntgen radiation can be used for the same purpose. Small wavelengths of synchrotron and neutron radiation enable an insight into the structure of very small objects, like molecules and nano-materials. Diffraction experiments with small incidence angle geometry must have a well-shaped beam since most of the incidence intensity is lost. This problem is somewhat solved with synchrotron radiation sources, where the beam is compact, collimated and has a high intensity (about three times more than the laboratory source). Besides a higher intensity, *brilliance* is what makes the synchrotron radiation superior to laboratory sources. This measure of the quality of the source takes into account the number of photons produced per second, the angular divergence of the photons, cross-section of the beam and the photons within a bandwidth of 0.1% of the central wavelength.

The significance of the methods that use synchrotron radiation is that they are non-destructive and applicable to various types of materials while providing a lot of information.

Small Angle X-ray Scattering (SAXS)

SAXS is a non-destructive and highly versatile standard method for the electron density fluctuations research, on the scale from a nanometer to a few hundreds of nanometers. By observing the electron density fluctuations on such small scales, it enables the study of structure for various types of nano-objects. Experiments are usually done in a so-called transmission geometry (**Figure 10** (a)), so that the incident beam goes through the sample and the diffraction is measured behind the sample, near the primary beam. This method is non-destructive and leaves the sample intact, which enables further research with it. Measured materials could be solid, liquid or even have gaseous properties, like aerosols. The advantage of SAXS over the imaging techniques like TEM is the statistical information about the sample since it includes a much larger sample volume.
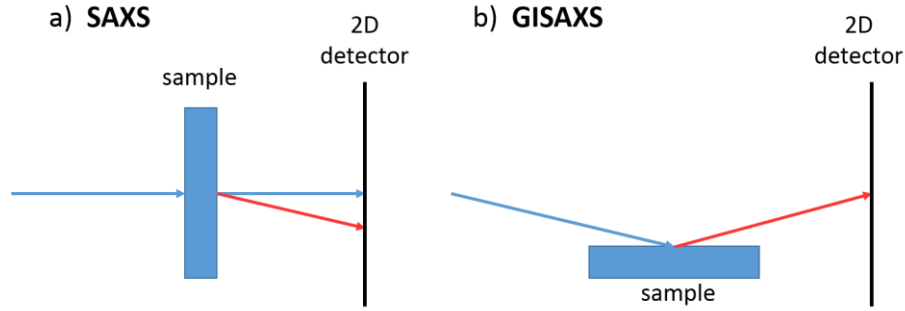
Figure 10. (a) Transmission geometry used for SAXS measurements where the X-ray goes through the sample, b) GISAXS geometry, the incident ray hits the sample under a small angle, refracts into the surface and diffracts on the thin film to the detector.

In order to get a SAXS signal from some material, there has to be a change in the average electron density. If the difference in the electron density comes from some particles or clusters, SAXS intensity will be proportional to the Fourier transform of their shape, also known as a *form factor*. When the particles are close to each other and form an ordered structure, an additional contribution to the diffraction appears, that comes from the particle correlations – the *structure factor*. The intensity of the signal is then:

$$I(q) \sim F(q)S(q) \tag{16}$$

When working with thin films that are usually on much thicker substrates than the film itself, the signal to noise ratio limits the use of the SAXS method. For those cases another method with a different geometry is used; geometry with a small incidence angle that ensures we get only the signal from the thin film (**Figure 10** (b)).

Grazing Incidence Small Angle X-Ray Scattering (GISAXS)

Modifying the traditional XRD and SAXS techniques into a grazing incidence (GI) geometry, we get a surface sensitivity and depth selectivity. GISAXS is an experimental method that is used for studying the structural properties. The advantage when compared to SAXS is the reduced contribution of the substrate in diffraction, that is, a better signal to noise ratio. In addition, surface sensitivity is higher and one gets a statistically averaged information from a big part of the sample surface. In our samples, a single measurement includes $\sim 10^{12}$ nanoparticles.

GISAXS experimental setup

As was mentioned earlier, measurement of the small angle diffuse scattering requires a high-quality beam: monochromatic, high intensity and collimation. Therefore, a GISAXS method has the best results with a synchrotron source. Newer generation synchrotrons have a special type of magnets, called *wigglers*, which cause the electrons to move in a winding path, therefore resulting in an even more intensive radiation. Such synchrotron sources have six orders of magnitude higher brilliance than the laboratory source.
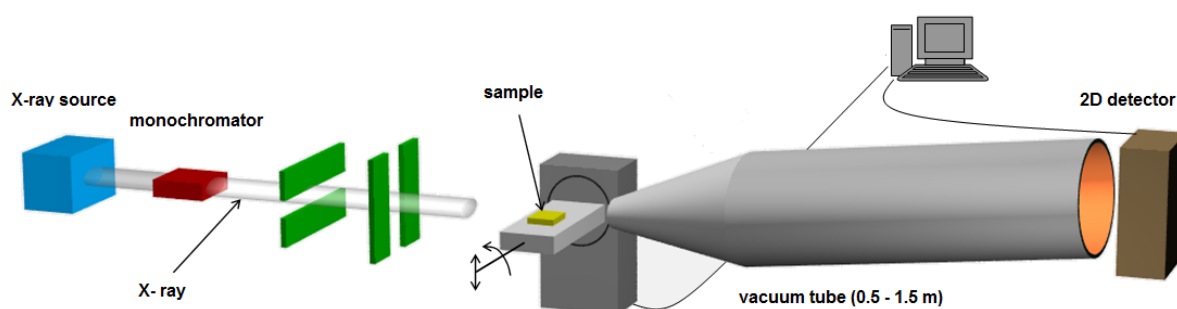

Figure 11. Simplified scheme of the experimental setup for GISAXS.

All of our GISAXS measurements were done at the SAXS beamline in synchrotron Elettra, Trieste. Energy of the incident X-rays was 8 keV (= 0.154 nm). Spectra were obtained with 2D image plate detector, 169×179 mm^2 and 981×1043 pixel resolution. The detector is set up perpendicular to the incident ray. For setting up the wanted incident angle a very precise sample mounting stage is used. The vacuum tube is used to lower the noise coming from the dispersion on air. **Figure 11**. shows the scheme of the experimental setup.

GISAXS method theory

The method is based on the total reflection principle: if the incidence angle is equal to the critical angle, then the refracted beam passes through the sample parallel to the surface. Increasing the incidence angle, the penetration depth of the X-ray to the sample is increasing, therefore giving us the information about the thin film structure on some wanted depth. A part of the incident beam diffracts incoherently due to the surface regularities, part of it reflects on the surface and the rest refracts on the surface into the sample and diffracts on the particles of interest (**Figure 12**).
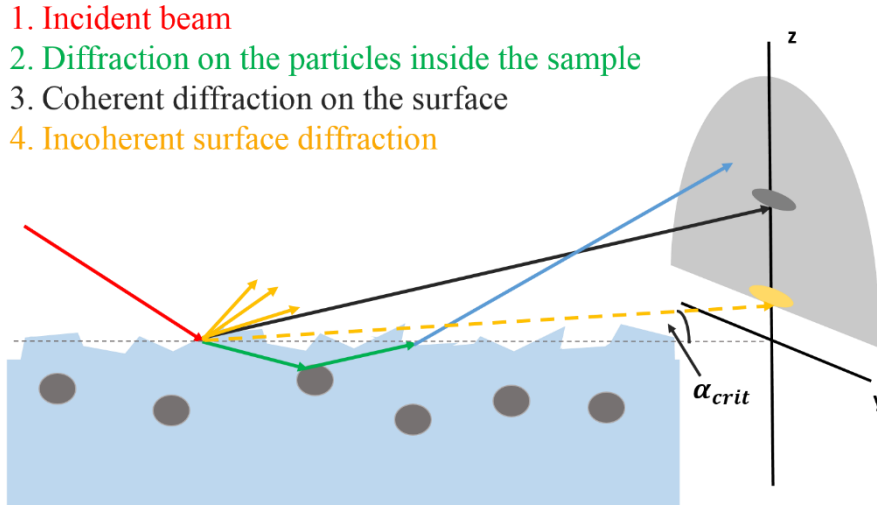
Figure 12. GISAXS diffraction scheme. Part of the incident beam will reflect on the surface (black arrow), part of it is incoherently scattered because of the surface irregularities (yellow), and a part refracts on the surface into the sample and diffracts on the particles of interest (green).

One of the main applications of GISAXS technique is the characterization of thin films with self-ordered systems on the nanometer scale. With the adequate analysis software for nanoparticles, it is possible to obtain the information about the particle shape, average size and distance between the particles, surface roughness and the depth distribution of those properties.

Detailed geometry of the diffraction and obtaining the GISAXS signal is shown in **Figure 13**. Incident ray is refracted at the surface, where the ratio of the incident α and refraction angle α' is given by Snell's law:

$$\frac{\cos \alpha}{\cos \alpha'} = \frac{n}{n_0} \tag{17}$$

where n and n_0 are refraction index of the sample and air, respectively. For X-rays, refraction index is a complex value [64]:

$$n = 1 - \delta - i\beta \tag{18}$$

δ being a parameter that depends on the medium density, and β describes the absorption. When the X-ray is passing through the sample, few effects should be taken into account [65] and corrections made:

o Refraction. The detector is measuring the intensity as a function of the angle 2θ between k_i and k_f, which is different than the angle of interest $2\theta'$ from the diffraction on the nanoparticles. Therefore, the diffraction intensity should be shown without the

refraction effects, as a function of the angle $2\theta'$. Diffraction is elastic, so the connection between the wave vector and the diffraction angle is:

$$\boldsymbol{q} = \boldsymbol{k_f} - \boldsymbol{k_i}, \qquad q = \frac{4\pi}{\lambda}\sin\theta \qquad (19)$$

o <u>Transmission</u>. Transmission through the surface is described with a Fresnel coefficient t, which is defined as an intensity ratio of the refracted and incident ray:

$$t = \left(\frac{2n_0\sin\sigma'}{n_0\sin\sigma' + n\sin\sigma}\right)^2, \qquad (20)$$

where σ' and σ are angles that the refracted beam closes with the surface (**Figure 13**). Transmission coefficient is maximal for the critical angle of the material, which is also a minimal angle under which the ray can enter the sample. For the real surfaces we have to consider the roughness of the surface and include the roughness coefficient ζ: [65]

$$\begin{aligned}
\tilde{t} &= t \cdot e^{\frac{(k_0 - k_1)^2\zeta^2}{2}} \\
k_0 &= k_f'\sin\sigma', \\
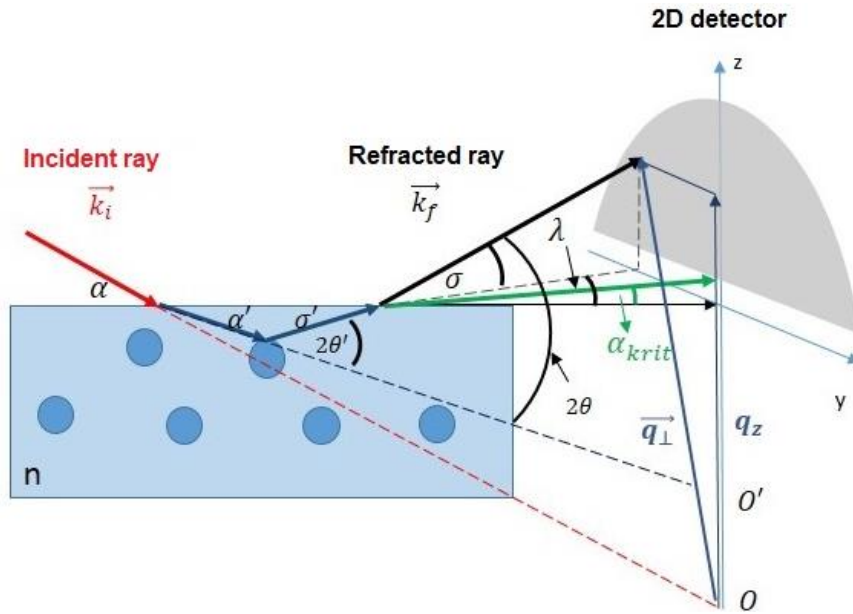k_1 &= k_f\sin\sigma.
\end{aligned} \qquad (21)$$

Figure 13. Detailed geometry of a GISAXS spectra. Scheme taken from Ref. 65.

- o Absorption. Part of the intensity is lost on absorption inside the material. Initial intensity I_0 of the refracted beam is decreased while passing through the material to the depth D and back, to the value:

$$I = I_0 \int_0^D e^{-\mu z\left(\frac{1}{\sin \alpha \prime} + \frac{1}{\sin \sigma \prime}\right)} dz, \tag{22}$$

Where the linear absorption coefficient μ is connected to the imaginary part of the refraction index β and the wavelength of the incoming ray with the expression:

$$\mu = \frac{4\pi\beta}{\lambda}. \tag{23}$$

GISAXS analysis of the experimental spectra

Analysis of 2D GISAXS maps is based on the calculation of the intensity distribution in the reciprocal space for the X-ray diffraction on the nanoparticles and adjusting the parameters of the calculation to the experimental values. Experimental phenomena that appear for X-ray diffraction under the small angle of incidence (grazing incidence) or a small angle of refraction, with rough surfaces and nanoparticles below the surface, can be described using the *Distorted Wave Born Approximation* (DWBA). In this approximation, the sample is divided into two parts: the undisturbed system and the perturbation. For the system of QDs assembled in a 3D lattice inside of the matrix, the matrix represents the undisturbed system, while the nanoparticles are the perturbation. Taking into account only the waves refracted from the perturbation (the quantum dots), the intensity of the refracted beam in the given point of the reciprocal space q, is given with the expression [24]:

$$I(\boldsymbol{Q}) = A|t_i t_f|^2 \left\langle \sum_{i,j} F_i(\boldsymbol{q}) e^{-i(\boldsymbol{q} \cdot \boldsymbol{r}_i)} \cdot F_j^*(\boldsymbol{q}) e^{-i(\boldsymbol{q}^* \cdot \boldsymbol{r}_j)} \right\rangle, \tag{24}$$

where A is a constant that includes the intensity of the incident beam, the difference in the electronic density of nanoparticles and matrix, detector efficiency and likewise factors that do not depend on the diffraction vectors. Fresnel coefficients for the incident and the outgoing ray t_i and t_f have been described in the previous section, $\boldsymbol{q}$ is the wave vector of dispersion on the nanoparticles under the surface corrected for the refraction effects, while $\boldsymbol{r}_i$ and $\boldsymbol{r}_j$ are the position vectors of the nanoparticles i and j. Factor $|t_i t_f|^2$ gives the Yoneda maximum when the exit angle matches the critical angle. The shape of the nanoparticle is described with the

form factor $F(\boldsymbol{q})$ which represents the Fourier transform of the nanoparticle shape. For the spheroidal shape the form factor is: [24]

$$F(\boldsymbol{q}, R_L, R_V) = 4\pi R_L^2 R_V \frac{\sin\psi - \psi\cos\psi}{\psi^3},$$

$$\psi = \sqrt{R_L^2(q_x^2 + q_y^2) + R_V^2 q_z^2}. \tag{25}$$

Lateral and vertical spheroid radii are R_L and R_V.

Next approximation we are using is called a *Decoupling Approximation* (DA), that assumes that nanoparticle sizes are not statistically correlated with their positions.[66] The brackets $\langle \rangle$ in Eq. (24) represent averaging over the chosen size distribution of nanoparticles around the average value, as well as the averaging over the position of the dots. Applying the DA gives us:

$$I(\boldsymbol{Q}) = A|t_i t_f|^2 \{ [\langle |F(\boldsymbol{q})|^2 \rangle - |\langle F(\boldsymbol{q}) \rangle|^2] \cdot G_I(\boldsymbol{q}) + |\langle F(\boldsymbol{q}) \rangle|^2 \cdot G(\boldsymbol{q}) \} \tag{26}$$

Where $G_I(\boldsymbol{q})$ is the sum of all illuminated nanoparticles if we neglect the effects of the X-ray absorption in the sample:

$$G_I(\boldsymbol{q}) = \left\langle \sum_i e^{-i r_i \cdot (\boldsymbol{q} - \boldsymbol{q}^*)} \right\rangle. \tag{27}$$

Function $G(\boldsymbol{q})$ is a 3D correlation function of the nanoparticles positions:

$$G(\boldsymbol{q}) = \left\langle \sum_{i,j} e^{-i(r_i \cdot \boldsymbol{q} - r_j \cdot \boldsymbol{q}^*)} \right\rangle. \tag{28}$$

In both expressions, the averaging goes only over the positions.

We assumed the nanoparticles are arranged in an irregular 3D lattice. If we denote the basis vectors with $\vec{a}^{(1,2,3)}$ and three indices $n_{1,2,3}$, the position of the nanoparticle is given by:

$$\vec{r}_{n_1,n_2,n_3} = n_1 \vec{a}^{(1)} + n_2 \vec{a}^{(2)} + n_3 \vec{a}^{(3)} + \vec{D}_{n_1}^{(1)} + \vec{D}_{n_2}^{(2)} + \vec{D}_{n_3}^{(3)} \tag{29}$$

where $\vec{D}_{n_k}^{(k)}, k = 1, 2, 3$ are random vectors that describe the deviation of the ideal position of the nanoparticle, regarding the origin and basis vectors. Depending on the ordering scope, we will use two models: *short range* and *long range ordering* (SRO and LRO). For the LRO the ideal position of the nanoparticles is predefined, while the real positions fluctuate around it. The SRO model assumes that only the neighbor nanoparticles are influencing the positions,

meaning that only the distance between the nanoparticles is predefined, but not their positions. Deviation of the ideal position is then depending on the model:

$$\vec{D}_{n_k}^{(k)} = \begin{cases} \sum_{j=1}^{n_k} \vec{\delta_j} & ; \ \text{SRO} \\ \vec{\delta}_{n_k}^{(k)} & ; \ \text{LRO} \end{cases} \qquad (30)$$

$\vec{\delta_j}$ being the random deviation vector from the ideal position of the nanoparticle with index j.

Choice of the basis vectors is based on the deposition process, where it is assumed that the diffusion and growth are the same within the plane parallel to the substrate, and are differing perpendicular to the substrate. Therefore, the first two vectors $\vec{a}^{(1,2)}$ are lying in the plane parallel to the surface ($x - y$ plane). Vector $\vec{a}^{(3)}$ can have an arbitrary direction, considering that the component $\vec{a}_z^{(3)}$ is the period of the multilayer. For samples used in this work, the periodicity of the multilayers is implying the long range order in the z direction (perpendicular to the surface), while the short range order is in the lateral components.

More details of the mathematical model used in the analysis of the experimental GISAXS results can be found in the literature. [24]

In this thesis, we are also working with the core/shell nanoparticles. The form factor calculation for that case follows that for the solid ellipsoid, but with separate terms for the core-shell and shell-matrix boundaries. However, the standard form-factors of a single spherical ellipsoidal core/shell shapes did not give a good match with the experiment for our samples. Taking into account the nature of the core-shell nanoparticle growth, that we discussed before, it is unlikely that the core and shell would be centrosymmetric. Therefore, we assume a shape of the core/shell QDs where the core is shifted from the center of the shell by a vector $\boldsymbol{d}$. Besides the core and shell, there is also a mixing interface layer of thickness T_{GeSi}, in which germanium and silicon atoms are mixed. Both core and shell parts of the QDs are assumed to be elongated in the direction parallel to the surface by a factor f:

$$R_L^{(core,shell)} = f R^{(core,shell)}, \qquad R_V^{(core,shell)} = R^{(core,shell)} \qquad (31)$$

Only the mixing interface layer has a constant thickness throughout the interface surface. All of this is demonstrated in **Figure 14**.
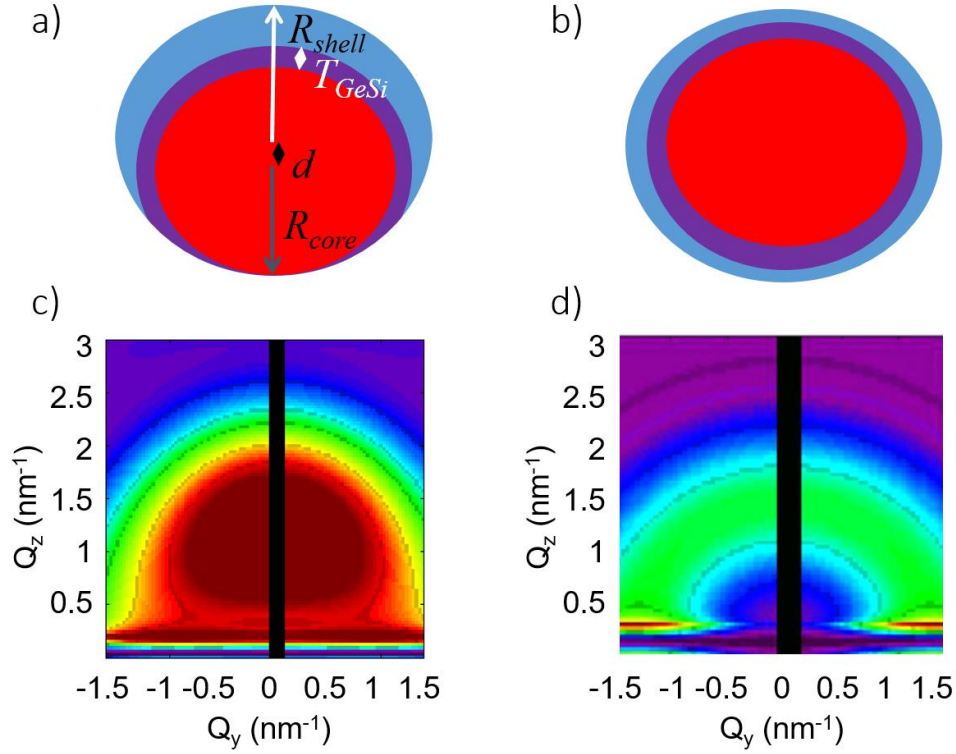
Figure 14. a) Shape of the core/shell QD used for the model, b) centrosymmetric core/shell QD, c) and d) show the corresponding form factors for the a) and b) shape.

Because of the very small sizes and almost a few atoms thick shells, the core/shell structure investigated in this thesis is extremely hard to see with the TEM measurements. This is why the GISAXS method is very important and interesting. To highlight the sensitivity of this method, the form factors of the core/shell and only core QDs with the same size and arrangement are shown (**Figure 15**). These images also show how the GISAXS maps would look like for a completely disordered system because the structure factor is then constant. On the other hand, in an ordered system, both the structure and the form factor give a contribution to the final GISAXS map. The results clearly show a difference between the core/shell and core self-assembled QDs, even for very thin shells, thus giving us a powerful tool for the core/shell structure investigation.
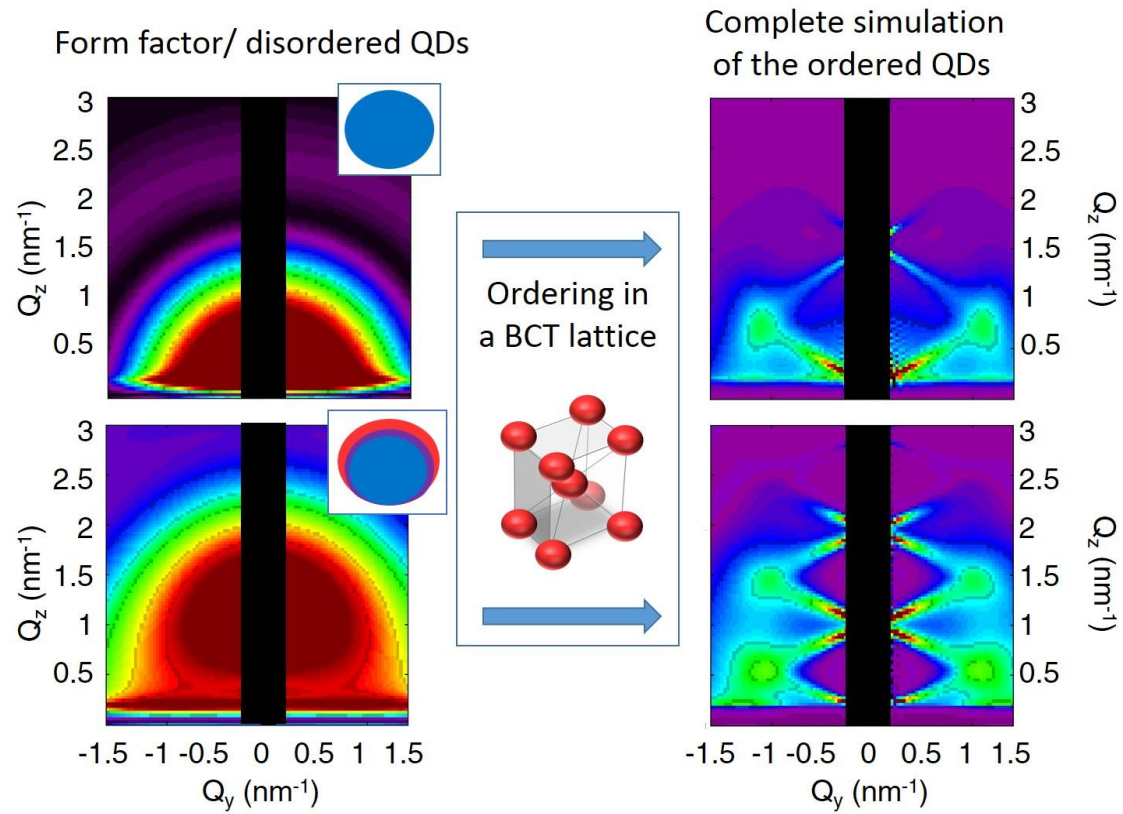
Figure 15. The difference between core/shell and only core QDs can be seen from the form factor images. For completely disordered QD system, the structure factor is constant and GISAXS maps are dominated by the form factor contribution only. By ordering the QDs in a BCT lattice, there is a contribution from both the structure and the form factor, resulting in the simulations shown on the right side of the figure. A clearly different image for the core/shell and only core QDs of the same size is shown. [67]

3.3. Spectroscopic ellipsometry

Spectroscopic ellipsometry is an optical measurement technique for investigating the optical constants of the sample. The light beam reflected from the sample is analyzed and the change in polarization of light is measured. The name comes from the fact that the polarized light often becomes elliptically polarized upon light reflection.

Linearly polarized light is obtained by combining two polarized light beams that are in phase, while elliptically polarized is the combination of the two orthogonally polarized beams out of phase. Elliptically polarized wave is the most general description of polarization state.

The optical constants describe the interaction between a light wave and a material. Incident light wave is refracted, slowed down and the wavelength changes upon entering the material. The complex refractive index describes this behavior and is defined as: [68]

$$\tilde{n}(\lambda) = n(\lambda) + ik(\lambda). \tag{32}$$

Both of those components are needed to describe materials. The real component n is often refered to as just *refractive index* and it is used for wave speed and the refraction angle calculation (Snell's law). The imaginary component is called the *extinction coefficient*, because it represents the loss of electromagnetic energy.

On the other hand, if we are interested in the material response to the incident electromagnetic wave, we define the complex dielectric function:

$$\varepsilon(\lambda) = \varepsilon_1(\lambda) + i\varepsilon_2(\lambda), \tag{33}$$

where ε_1 represents the volume polarization that comes from the dipole polarization, while ε_2 represents the volume absorption. The dielectric function describes the material response to electromagnetic radiation, while the refractive index describes the light wave response to interaction with the material. The connection between these optical constants at each wavelength is:

$$(n + ik)^2 = \varepsilon_1 + i\varepsilon_2. \tag{34}$$

Furthermore, wavelength dependent absorption coefficient can be calculated from the imaginary part of the refraction index as:

$$\alpha(\lambda) = \frac{4\pi k(\lambda)}{\lambda}. \tag{35}$$

The basic overview of the ellipsometry measurement is shown in **Figure 16**. Linearly polarized light enters the surface, reflects off the sample and the change in polarization of the reflected light is measured.
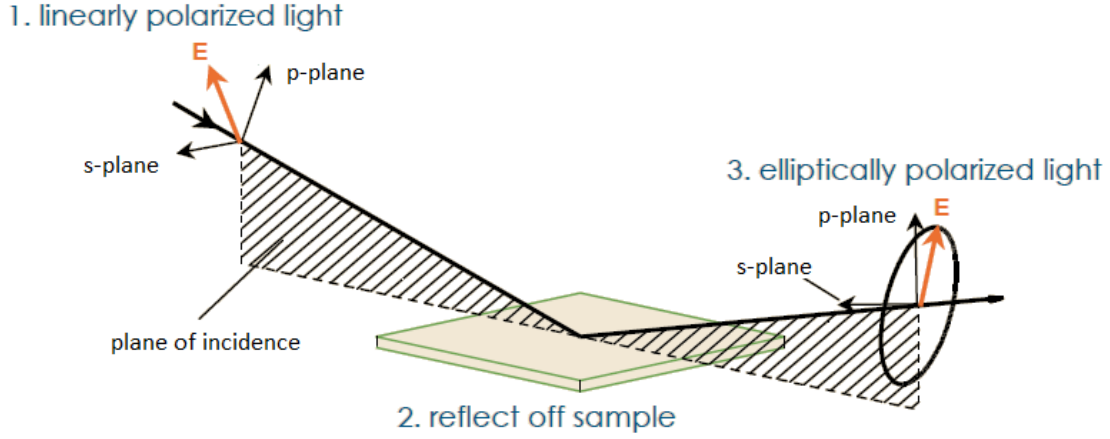

Figure 16. Basic principles of ellipsometry measurement. Linearly polarized light comes to the sample and after reflection becomes elliptically polarized. The difference in polarization is measured.

Ellipsometry measures the two values: the amplitude ratio ψ and phase difference Δ between p- and s- polarized light waves (s- stands for germ. *senkrecht*, which means perpendicular and p- *parallel* to the plane of incidence).

The two values (ψ, Δ) measured from ellipsometry are connected with the ratio of reflection coefficients for p- and s-polarizations:

$$\rho \equiv \tan\psi \exp(-i\Delta) \equiv \frac{r_p}{r_s}, \tag{36}$$

where the reflection coefficients are given by the square root ratio of reflected intensity I_r and incident light intensity I_i:

$$\frac{I_{rp}}{I_{ip}} = |r_p|^2, \quad \frac{I_{rs}}{I_{is}} = |r_s|^2. \tag{37}$$

Moreover, if polar coordinates are used, reflection coefficients can also be expressed as:

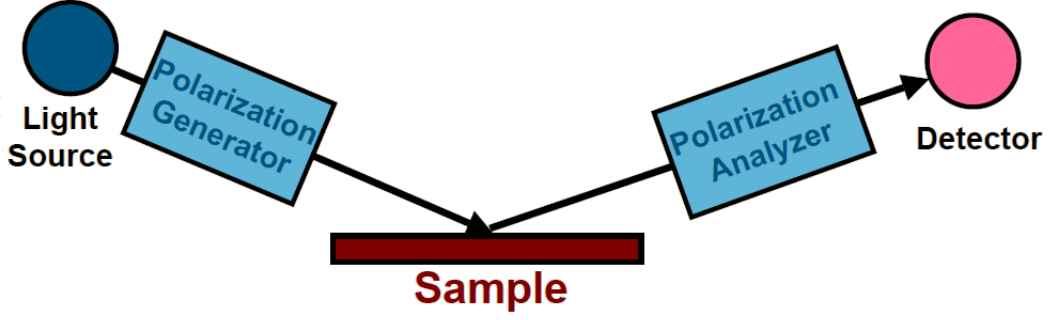$$\tan\psi = \frac{|r_p|}{|r_s|}, \quad \Delta = \delta_{rp} - \delta_{rs}. \tag{38}$$

Figure 17. A scheme of the ellipsometry measurement setup.

Since the difference between r_p and r_s is maximized at the Brewster angle, sensitivity also increases at this angle. Therefore, the measurement is generally preformed at the Brewster angle. In ellipsometry, ψ and Δ are measured, while the thickness of the film and index of refraction are calculated, based on a model.

It is interesting to note that when the sample structure is simple, the amplitude ratio ψ can be connected with the refractive index n, while the phase difference Δ can be connected with absorption characterized by the extinction coefficient k. Therefore, the complex refractive index can be obtained directly from the two measured parameters (ψ, Δ), by applying the Fresnel equations. [68] Fresnel equations define the reflection and transmission coefficients for p-polarized light, given by:

$$r_p \equiv \frac{E_{rp}}{E_{ip}} = \frac{n_t cos\theta_i - n_i cos\theta_t}{n_t cos\theta_i + n_i cos\theta_t},$$

$$t_p \equiv \frac{E_{tp}}{E_{ip}} = \frac{2n_i cos\theta_i}{n_t cos\theta_i + n_i cos\theta_t},$$

(39)

where θ represents the angles, n refractive indices, E electric field amplitudes, while the subscripts i, r, and t represent the incidence, reflection and transmission. Similarly, the reflection (transmission) coefficient for s-polarized light is expressed by:

$$r_s \equiv \frac{E_{rs}}{E_{is}} = \frac{n_i cos\theta_i - n_t cos\theta_t}{n_i cos\theta_i + n_t cos\theta_t},$$

$$t_p \equiv \frac{E_{tp}}{E_{ip}} = \frac{2n_i cos\theta_i}{n_i cos\theta_i + n_t cos\theta_t}.$$

(40)

The above equations are still valid when the refractive index n is a complex refractive index $\tilde{n}$. In that case, coefficients become complex numbers, as well.

The ellipsometric analysis relies on the model that depends on the system under investigation. Since we are investigating a multilayer thin film with nanoparticles, the analysis was done by considering each multilayer as a single homogenous film with a thickness equal to the multilayer thickness. Effective optical constants were modeled using a flexible multiple-oscillator model. [69] We shall not go into the details of this model, because the details are not of relevance for this work.

Ellipsometry was measured using VASE ellipsometer from J.A.Wollam Co, Inc., in the spectral range between 1 and 5 eV and incidence angles of 65°, 70°, and 75°.

3.4. Electrical and photocurrent measurements

Contacts

When considering the contact materials for semiconductors, it is important to know whether the metal and semiconductor are making an ohmic contact or a Schottky contact. If a metal work function ϕ_m is larger than a semiconductor electron affinity χ_s, the Schottky barrier height is equal to $\phi_B = \phi_m - \chi_s$. Because of the barrier, there is a depletion region in the semiconductor, near the interface, thus making a rectifying contact, with the current-voltage relationship qualitatively the same as a p-n junction. If the metal work function is smaller than a semiconductor electron affinity, the ohmic contact should form.

This way of predicting the energy barrier is called the Schottky-Mott rule. However, in practice, most of the metal-semiconductor junctions do not follow this rule, because of the effect known as the Fermi level pinning.

For that reason, and also because we are using different materials, it is always important to check experimentally the contacts. The ohmic contacts are characterized by a linear I-V characteristic in both current directions with a low contact resistance, which enables the efficient flow of carriers. The Schottky contact, on the other hand, has a non-ohmic, rectifying behavior.
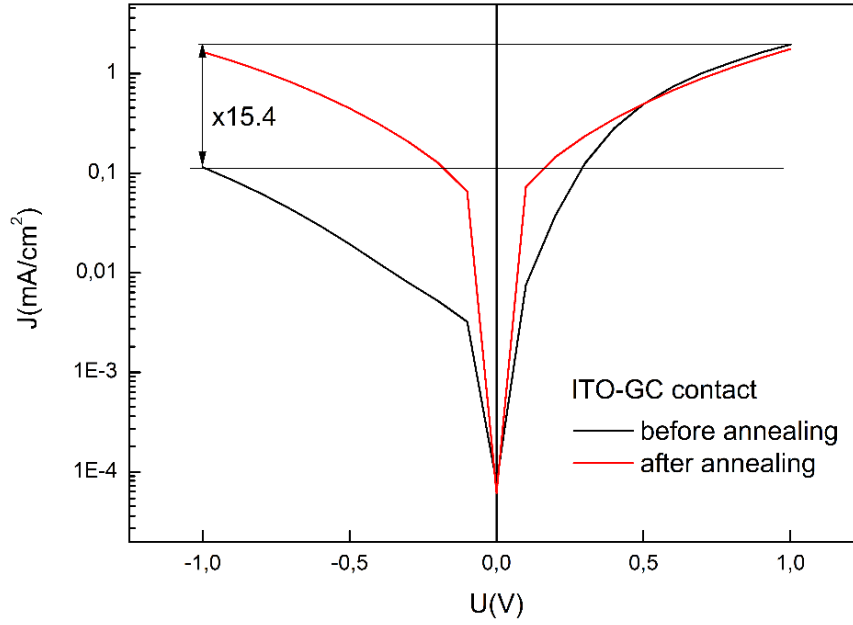
Figure 18. Comparison of the J-V curves for the ohmic and non-ohmic ITO contacts on the GC (Ge/SiC) sample. Before annealing, the contact has the rectifying behavior with the 15.4 ratio in the -1V to 1V range (black line), while after 15 min on 400 °C in vacuum, the contact becomes ohmic, with a symmetrical behavior (red line). [2]

We used magnetron sputtering deposition for all contact materials. Aluminum was used for the back contact on p-type silicon and was additionally annealed to 400 °C in vacuum, for 15 min. That way the diffusion of aluminum into silicon is ensured. Aluminum acts as a p-type dopant, therefore making a highly doped surface layer of silicon by diffusing into the surface. This doping is decreasing the depleted region, thereby reducing the Schottky barrier to the point where the carriers could easily tunnel through.

ITO (Indium doped Tin Oxide) was used as a top transparent contact. **Figure 18** shows the formation of an ohmic contact between ITO and GC-sample (Ge QDs in SiC matrix) after a short annealing. This measurement was done for at least one representative sample in the group, to ensure that all thin films form an ohmic contact with the ITO. It is important to note that the current in Figure 18 for negative voltages is also negative, but is shown in logarithmic scale for easier comparison, therefore absolute value of current was taken. This way of current-voltage representation is present later in Experimental section, as well.

---

[2] Note that current values are negative for $V < 0$, but logarithmic scale and absolute values of current are used for convenient comparison of positive and negative voltages.

All contacts were deposited after placing a shadowing mask, in order to ensure a specific and uniform contact surface on all samples. The mask and hence the contacts have a surface area of $19.6\ mm^2$.
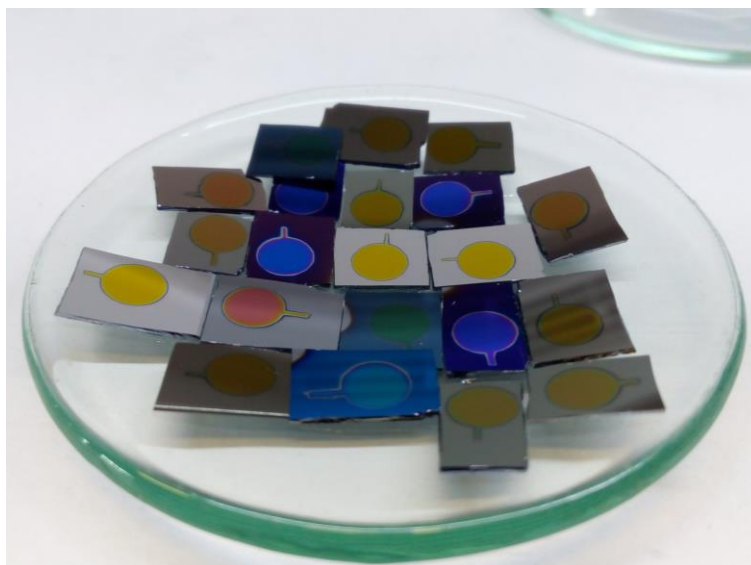

Figure 19. A photo of samples after the deposition of the upper ITO contacts. All contacts have the same surface area.

Current-voltage measurements

All current-voltage (I-V) measurements were done with a Keithley 2401 Sourcemeter SMU, controlled and data collected by a LabView program. For the illumination, a Sciencetech Solar Simulator that has an arc xenon lamp was used.

In order to test the materials performances as detectors, a metal – "insulator" – semiconductor (MIS) device was made, according to the scheme shown on the inset of **Figure 20**.

All measurements were done in dark and under illumination (light) in order to test the photoresponse.
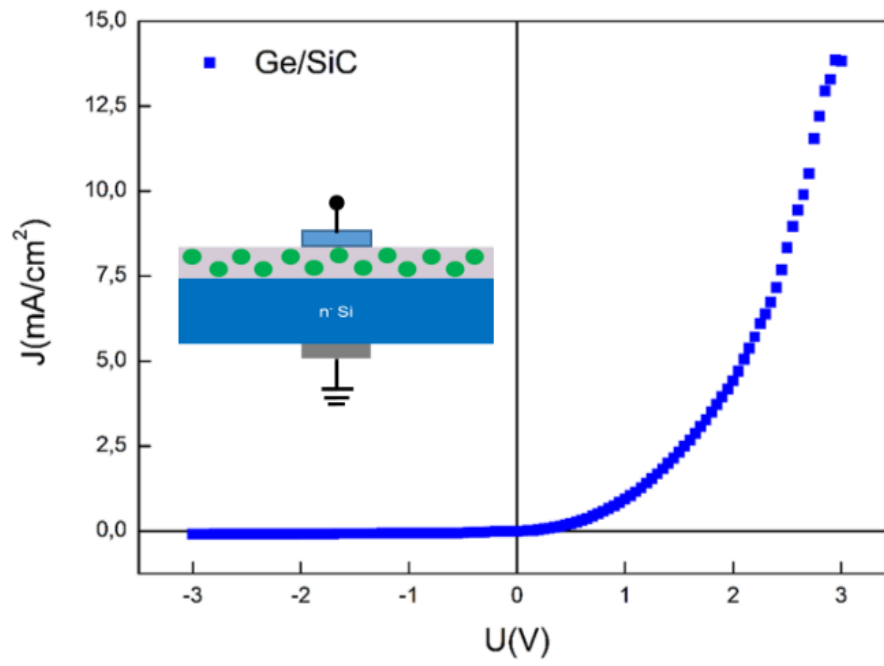
Figure 20. A typical I-V curve of the device has a rectifying behavior. Inset shows a scheme of the device made for the I-V measurements. Instead of the insulator in the MIS structure, we put the QD thin film of interest.

4. MEASUREMENTS AND RESULTS

Samples investigated in this thesis are classified into groups:

I. Ge/Si group contains Ge/Si QDs in alumina matrix. Three series are contained in this group: a) QDs with different core sizes and shell thicknesses, b) samples with different alumina layer thickness, and c) samples deposited on different deposition temperatures.

II. GC, GN and GA groups where we used different matrices: SiC, Si_3N_4, and Al_2O_3 in search for other solutions, so that Ge oxidation would be avoided. QDs in SiC and Si_3N_4 are not core/shell, but only Ge QDs.

III. ACN group – the samples that showed best structural properties, one of each for every matrix were chosen for further investigation of electrical properties.
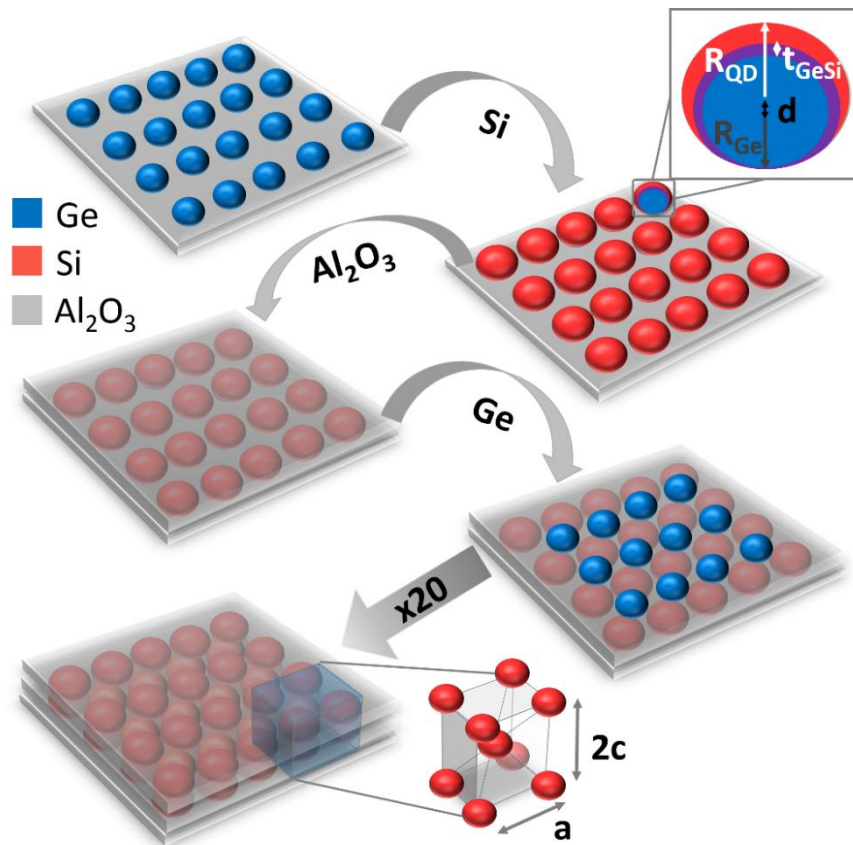

Figure 21. Magnetron sputtering deposition of Al_2O_3/Ge/Si multilayer results in a core/shell quantum dot structure. The upper right inset shows a cross-section of one QD. The core center is shifted and there is an intermixing layer at the interface between Ge and Si. Quantum dots self-assemble in a body-centered tetragonal (BCT) lattice. [67]

Samples are made simply by alternating the sputtering deposition of the two or three materials, depending on whether the nanoparticles have a shell or not. First, deposited layer is the matrix (M: Al_2O_3, SiC or Si_3N_4), following with the Ge layer and Si layer for the shell. **Figure 21** is a schematic representation of the deposition process, showing also the resulting self-organization of the nanoparticles in the BCT lattice. The parameters of the BCT lattice are two base vectors a and c, which represent the in-layer distance of the QDs and the multilayer period respectively. Sputter deposition method used here is a crucial difference between other work with Ge or Si QDs in oxide matrices that was done elsewhere. [60,70,71] Most of them obtain QDs by first depositing multilayers of silicon/germanium rich oxide and silicon oxide, which yields crystalline QDs only after annealing. Those QDs are not ordered and annealing is needed to form the dots, otherwise, only multilayers are present. On the other hand, QDs presented in this work are amorphous after the deposition, but are assembled in a BCT lattice. It should be noted that the two methods can produce very different interfaces. This difference in the QD production and the appearance of self-assembly could cause different properties, which makes the research of these systems even more interesting.

In this work, multiple substrates were used: silicon wafers, glass, and quartz depending on the type of measurement that was being done. The first deposited layer was always the matrix material. That way morphology of the substrate has a minimal effect on the type and quality of nanoparticle ordering. We also confirmed that with GISAXS measurements.

Figure 22 shows the GISAXS map of the same film consisting of Ge QDs in an alumina matrix, on two different substrates. The maps are very similar, showing that the substrate does not significantly influence the QD ordering quality. Mostly the central part (close to $Q_y = 0$) differs, and the difference originates from the different surface roughness of the substrates.
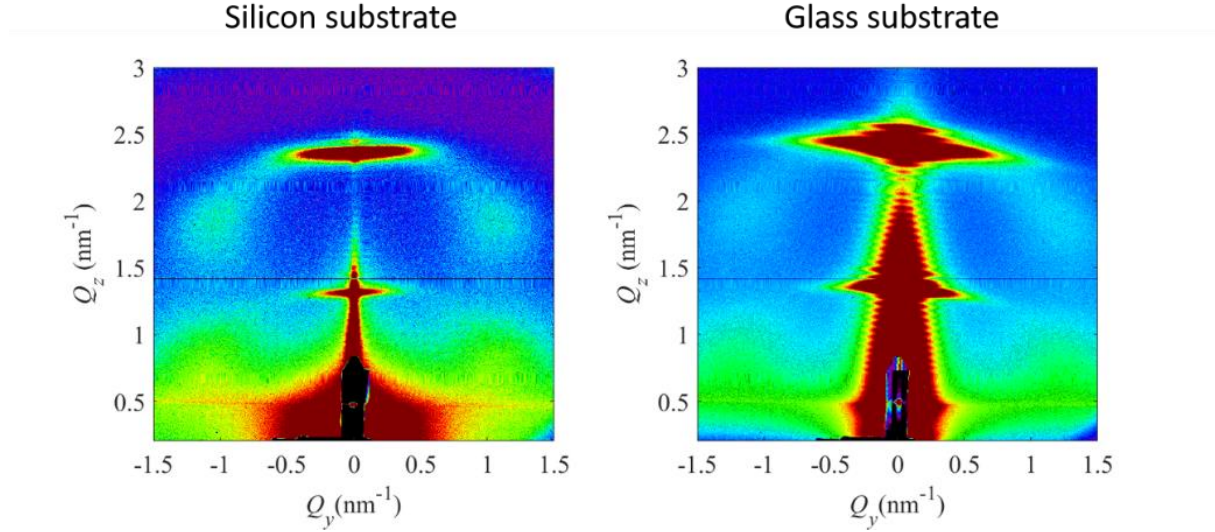
Figure 22. Two GISAXS maps for the same sample on two different substrates: silicon and glass substrate.

4.1. Structural properties

Structure of the thin films was studied primarily by Grazing Incidence Small Angle X-Ray Scattering (GISAXS) method.

The Ge/Si group was made of samples differing by the size of the Si shell and Ge core. Let us divide them into two subgroups: a) samples named Ge, Ge/Si1, Ge/Si2 and Ge/Si3, in which the Ge sample has no shell, while the shell size in other samples increases respectively, b) samples Ge/Si2, Ge1/Si, Ge2/Si and Ge3/Si, in which the core size increases respectively, while the amount of silicon remains the same. Ge/Si2 is one sample that is used in both subgroups. Note that the shell thickness is also slightly changed in the last three samples since the core size is getting larger. To vary the sizes of the core and shell, different deposition times were used, while the alumina deposition time was the same for all samples. Magnetron powers were 300W, 10W and 50W for Al_2O_3, Ge and Si target respectively. Deposition time for Ge and Si target, as well as atomic percentages, are given in **Table 2**. The self-ordered growth regime results in a regular spatial distribution of the QDs in the matrix, as well as in QD size uniformity. [48] QDs are amorphous after the deposition.

Transmission electron microscopy was measured on two samples: Ge/Si2 and Ge3/Si. Ge/Si3 has the well-ordered structure of QDs, while the dots in Ge3/Si have merged together. These measurements are in agreement with the GISAXS results, as will be shown next.

The multilayer structure is clearly visible and there is an indication of the QD ordering. However, the complex core/shell structure is very challenging to see for such a small QD size.

A TEM micrograph is a two-dimensional projection of the analyzed sample, so it is extremely challenging to distinguish between the core and shell of the QDs in the TEM images. This emphasizes the importance of the GISAXS method for the structural analysis of these samples.
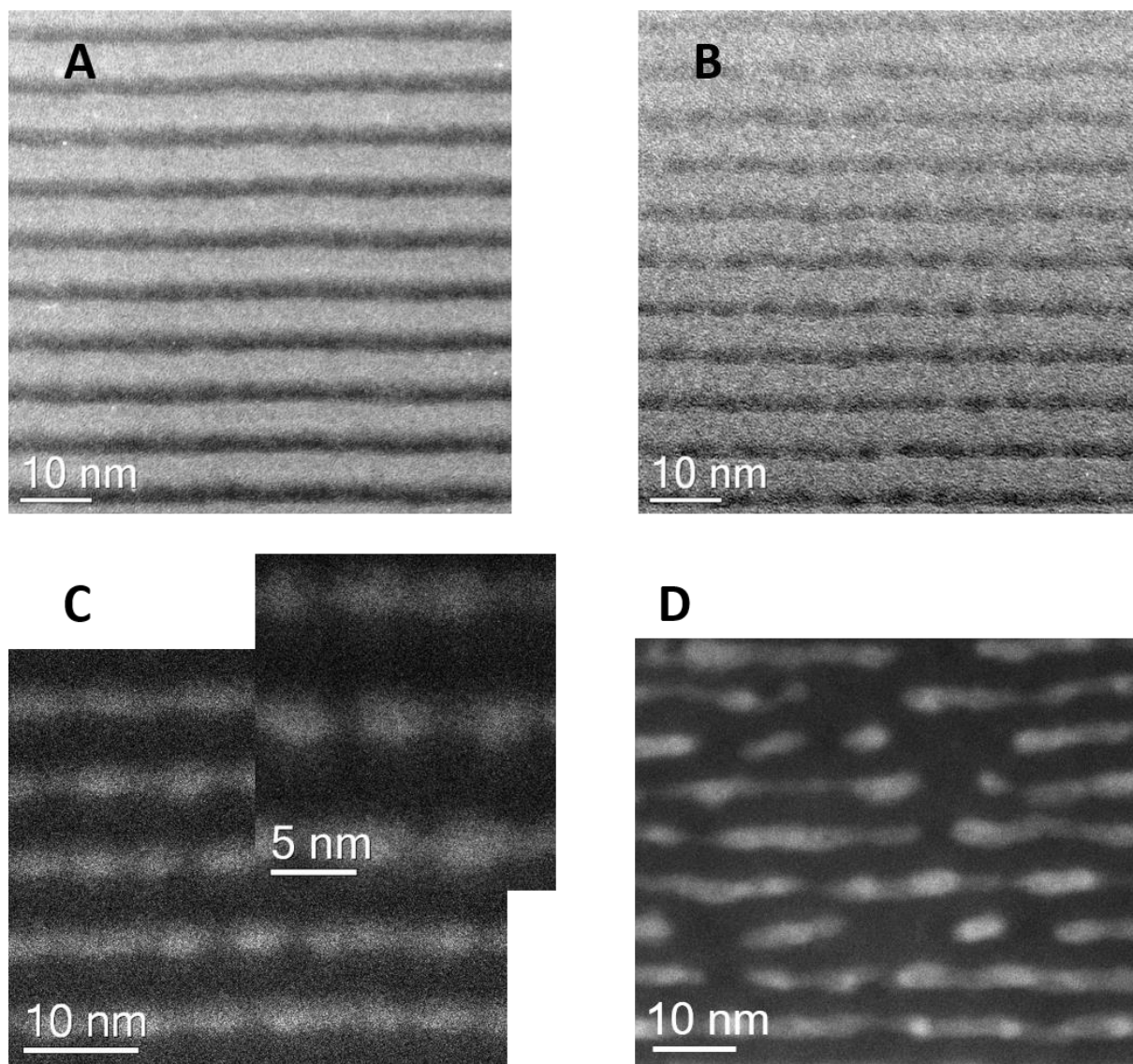

Figure 23. CTEM picture of the a) Ge3/Si sample, b) Ge/Si2 sample, c) STEM of the Ge/Si2 clearly showing QDs of about 3 nm radius and d) STEM of the Ge/Si3 sample after annealing to 800 ℃.
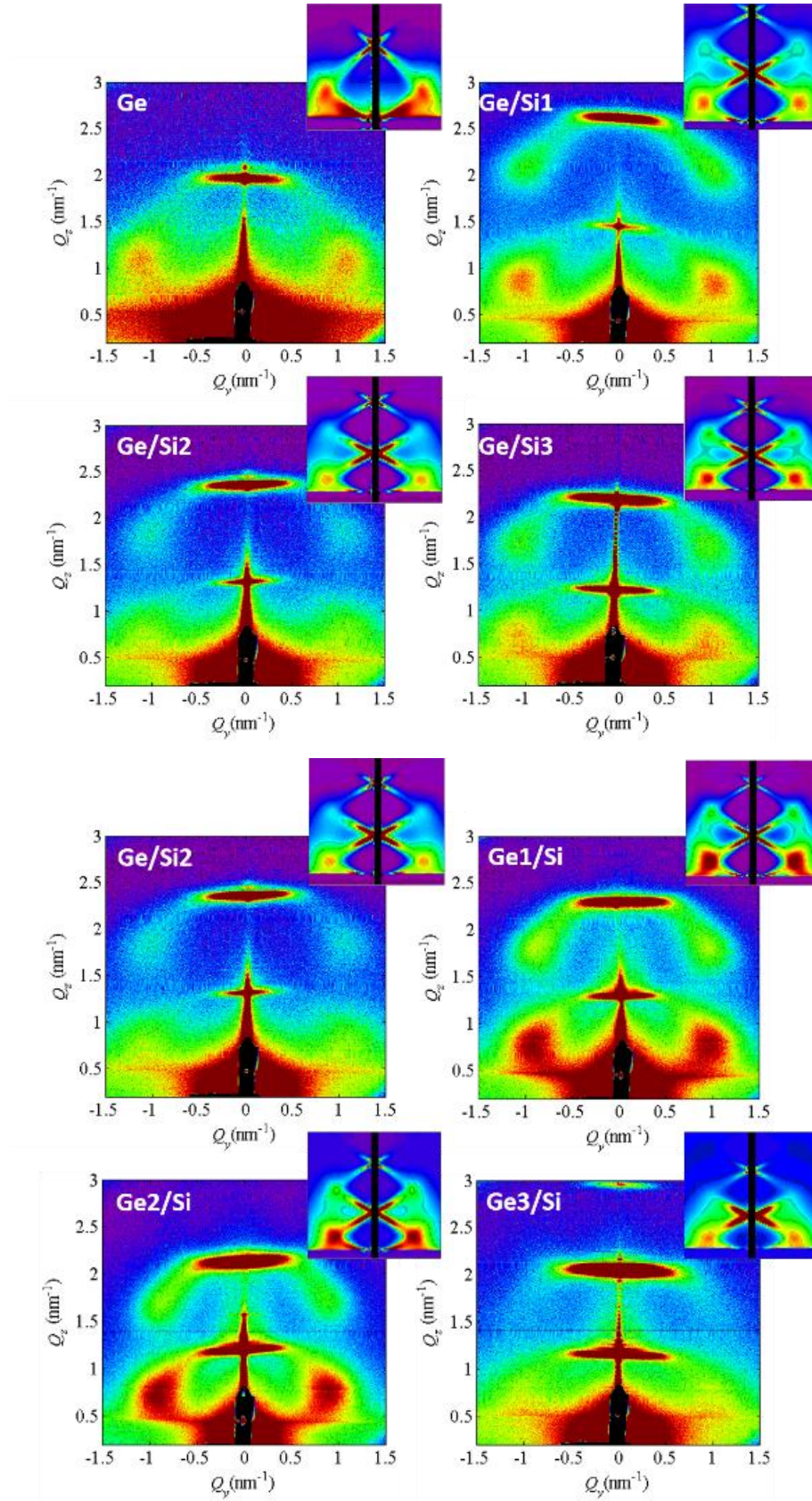
Figure 24. GISAXS maps of all studied samples. Insets show the simulations obtained using the model that was explained in detail in Ref. 48.

The GISAXS maps of all samples are shown in (**Figure 24**). Four characteristic lateral intensity maxima (Bragg spots) are visible in all maps, showing that the formed QDs are well-arranged in a 3D QD lattice. According to the model described in Section 3.2., GISAXS maps were numerically analyzed. As we already mentioned, it is assumed that the QDs are arranged in a BCT lattice and have a core/shell internal structure, with the center of the core shifted from the shell center (**Figure 14** (a)). Simulations obtained by numerical analysis are shown in the insets of **Figure 24**. These simulations are in good agreement with the measurements for $|Q_y| > 0.5$ nm^{-1}. For lower values of $|Q_y|$ there is a significant contribution from the correlated roughness of the multilayer. That contribution is partially responsible for the horizontal sheets appearing in the central part of the GISAXS map. As this contribution is not taken into account in the model used for the description of the QDs, and the model assumes a 3D lattice of QDs, the central parts of the simulated and experimental maps significantly differ. More details about the appearance of crossings in the simulated maps can be found in Ref. 24. The mentioned range with the small $|Q_y|$ values is not important for this study, because we are interested only in the $|Q_y|$-values where the dominant contribution to GISAXS intensities comes from the QDs.

Table 1. Quantum dot size and other parameters determined from GISAXS: QD in-layer separation a, multilayer period c, QD and core radius, shell thickness t_{shell}, and the shift of the core from the center of the shell d.

Samples	a (nm)	c (nm)	R_{QD}(nm)	R_{core}(nm)	t_{shell}(nm)	d(nm)
Ge	4.8 ± 0.2	4.1 ± 0.2	1.8 ± 0.2	1.8 ± 0.2	0	0
Ge/Si1	4.9 ± 0.2	5.1 ± 0.2	2.1 ± 0.1	1.70 ± 0.05	0.6 ± 0.2	0.40 ± 0.06
Ge/Si2	4.8 ± 0.2	6.4 ± 0.2	2.4 ± 0.2	1.70 ± 0.05	1.0 ± 0.2	0.6 ± 0.1
Ge/Si3	5.6 ± 0.2	6.8 ± 0.2	2.6 ± 0.2	1.70 ± 0.05	1.3 ± 0.4	0.9 ± 0.1
Ge1/Si	4.8 ± 0.2	6.4 ± 0.2	2.4 ± 0.2	2.2 ± 0.1	1.0 ± 0.2	0.6 ± 0.1
Ge2/Si	6.0 ± 0.2	6.4 ± 0.1	2.9 ± 0.2	2.4 ± 0.1	0.9 ± 0.5	0.7 ± 0.1

The parameters obtained from the simulation are given in **Table 1**. The size of the Ge core and Si shell really increase, as it was intended with the deposition parameters. Besides the ones in the table, some other parameters were also obtained with the analysis, which have similar values for all samples. Values of the radius standard deviation σ_R are in the interval $[0.2 - 0.4]$, where the deviation is higher for a larger radius. All samples have a similar intermixing layer thickness around $t_{GeSi} = (0.3 \pm 0.1)$nm. Relatively strong, narrow lateral Bragg peaks are a sign of a

very good ordering in most samples. The exception being Ge3/Si, with a decreased ordering quality. The reason for that was the merging of Ge cores, after which covering with Si created a layer, rather than separate QDs. Therefore, quantum dots were not created in that sample, which is also clear from the TEM measurement (**Figure 23**). For this reason, this sample was left out of further analysis.

With Time of Flight Elastic Recoil Detection Analysis (ToF-ERDA) the chemical composition was found, i.e. the atomic percentages of Ge, Si, Al, and O are obtained (**Table 2**). It is shown that the percentage of Si is rising from Ge/Si1 to Ge/Si3, also the atomic percentage of Ge is gradually growing from Ge1/Si to Ge3/Si thin films, as is in accordance with the deposition parameters. The atomic composition is found to be homogeneous throughout the film.

These results are also important to check the reliability of the GISAXS model used to describe the QD internal structure. Using the parameters obtained from GISAXS, the atomic composition of the crystalline Ge/Si QDs in alumina matrix was calculated.

Table 2. Ge and Si deposition times and atomic percentages for all samples. The silicon percentage is rising from samples Ge/Si1 to Ge/Si3, since silicon deposition time was increased. Samples Ge1/Si to Ge4/Si show an increasing percentage of germanium, in accordance with the increase in a deposition time of germanium.

Sample	t_{Ge} [s]	t_{Si} [s]	Ge [at.%]	Si [at.%]	Al [at.%]	O [at.%]
Ge	55	0	9.9 ± 0.6	0.82 ± 0.08	27 ± 1	57 ± 3
Ge/Si1	55	30	8.6 ± 0.6	6.5 ± 0.5	27 ± 1	52 ± 3
Ge/Si2	55	60	8.7 ± 0.6	11.3 ± 0.7	26 ± 1	48 ± 3
Ge/Si3	55	90	8.2 ± 0.5	16.2 ± 1	26 ± 1	43 ± 2
Ge/Si2	55	60	8.7 ± 0.6	11.3 ± 0.7	26 ± 1	48 ± 3
Ge1/Si	75	60	12.0 ± 0.8	12.0 ± 0.8	27 ± 1	44 ± 2
Ge2/Si	95	60	13.0 ± 0.7	13.2 ± 0.7	24 ± 1	46 ± 2
Ge3/Si	115	60	16.8 ± 1.1	11.4 ± 0.8	23 ± 1	43 ± 2

The obtained values agree very well with the measured values, indicating that the GISAXS parameters are valid. Therefore, this procedure was repeated for every structural analysis in this work from now on.

To summarize, we managed to produce core/shell quantum dots differing in silicon shell thickness, as well as differing in core radius. Important to note is that there is also a critical

amount of germanium that could be sputtered, after which QDs start to merge. For 300 °C deposition temperature that was 17 at.% germanium, with QD radius of 3 nm. Production of samples with bigger QDs is only possible with higher temperatures which increase diffusion and hence the in-layer distance and radius, as well.

Influence of the annealing

Annealing, in general, is a heat treatment that changes properties of materials. In this work, we use the term annealing to denote heating samples in a vacuum tube for 30 minutes on a specified temperature. Annealing is often used to reduce the defects and dangling bonds in the material and to obtain crystallization. Most of the times, high temperatures of at least 800℃ are needed to get crystalline Ge QDs. [46,50] Even higher temperatures are needed for Si QDs (1000 ℃). However, crystallization temperatures can change depending on the matrix that QDs are embedded in. [47,72]

Increased temperature enables germanium atoms to diffuse through the alumina matrix. From the TEM image of the annealed sample Ge/Si3_800 on **Figure 23** d) it is visible that the QDs have merged together to form elongated ellipsoids that are somewhat further away from each other, than the QDs in the as-grown samples. A similar effect was observed for Ge clusters in SiO$_2$, where it was shown that the clusters undergo Ostwald ripening and crystallization for annealing temperatures higher than 700℃. [73] Larger clusters are energetically more favorable.

This can also be seen from GISAXS. Two samples were measured with GISAXS: Ge (without a shell) and Ge/Si2 both as-grown and annealed (**Figure 25**). It is evident that the assembly and the shape of the nanoparticles have changed with the heating. Therefore, we cannot apply the same model for the analysis of annealed samples. But a short qualitative analysis can give us enough information. As we know, a peak in the reciprocal space comes from a repeating structure in the real space. From the peak position q in the reciprocal space, we can calculate the distances between those structures: [74]

$$d = \frac{2\pi}{q} \tag{41}$$

From this expression, the calculated lateral distances of the QDs are 5nm and 11nm for Ge and Ge/Si2 samples respectively, which agrees with the TEM image.

Sample Ge was annealed only to 700℃ since it was enough to crystallize the QDs, while a higher temperature causes the oxidation of germanium. On the other hand, samples with a

silicon shell crystallize after 800℃ annealing. To confirm this and obtain an insight into the Ge and Si bonding properties, we performed Raman measurements on all samples from the Ge/Si group.
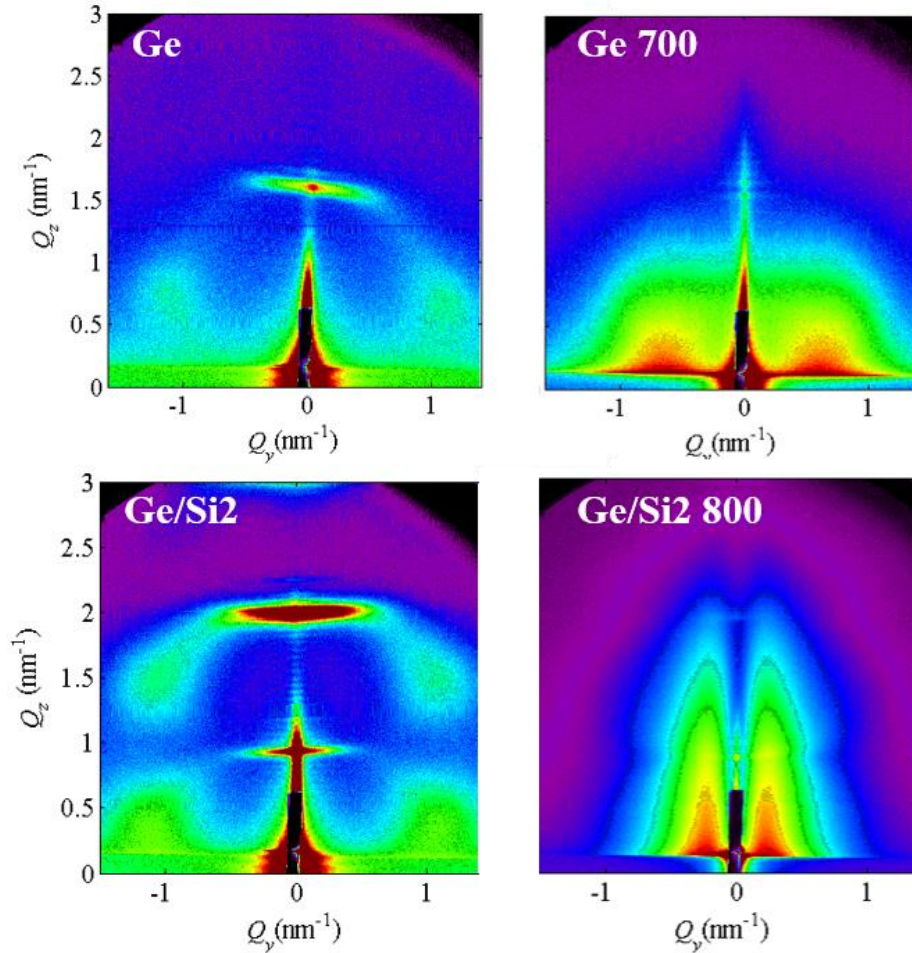

Figure 25. Effect of the annealing on Ge and Ge/Si2 samples. GISAXS maps of both as-grown (left) and annealed samples (right) are shown.

The results are summarized in **Figure 26**. The amorphous Ge-Ge related band appears around 80 cm^{-1} and 275 cm^{-1}, the amorphous Si-Si peak around 470 cm^{-1}, while the Ge-Si band appears close to 380 cm^{-1}. Corresponding crystalline bands are shifted slightly to higher k values from the amorphous ones. The Raman spectra of the annealed samples with a constant Ge-core, show a slight increase of the Si-related band, while the width and intensity of the Ge-related bands are nearly constant. For samples with a constant shell thickness and increasing core sizes; the intensity of the Ge-peak is increasing and becomes narrower. The Ge-Si band is visible for all samples containing core/shell QDs. A nearly constant intensity of the Ge-Si band for all samples

indicates the same thickness of the Ge/Si interface layer, in correspondence with the parameters obtained from GISAXS analysis (**Table 1**). The exception is the sample Ge/Si1 with the thinnest Si shell, which has a Ge-Si band, but significantly lower. This could simply be due to the fact that the Si shell is much thinner, so most of this thin silicon shell is oxidized with the excess oxygen in the matrix, causing a reduced intensity of the Ge-Si Raman band.
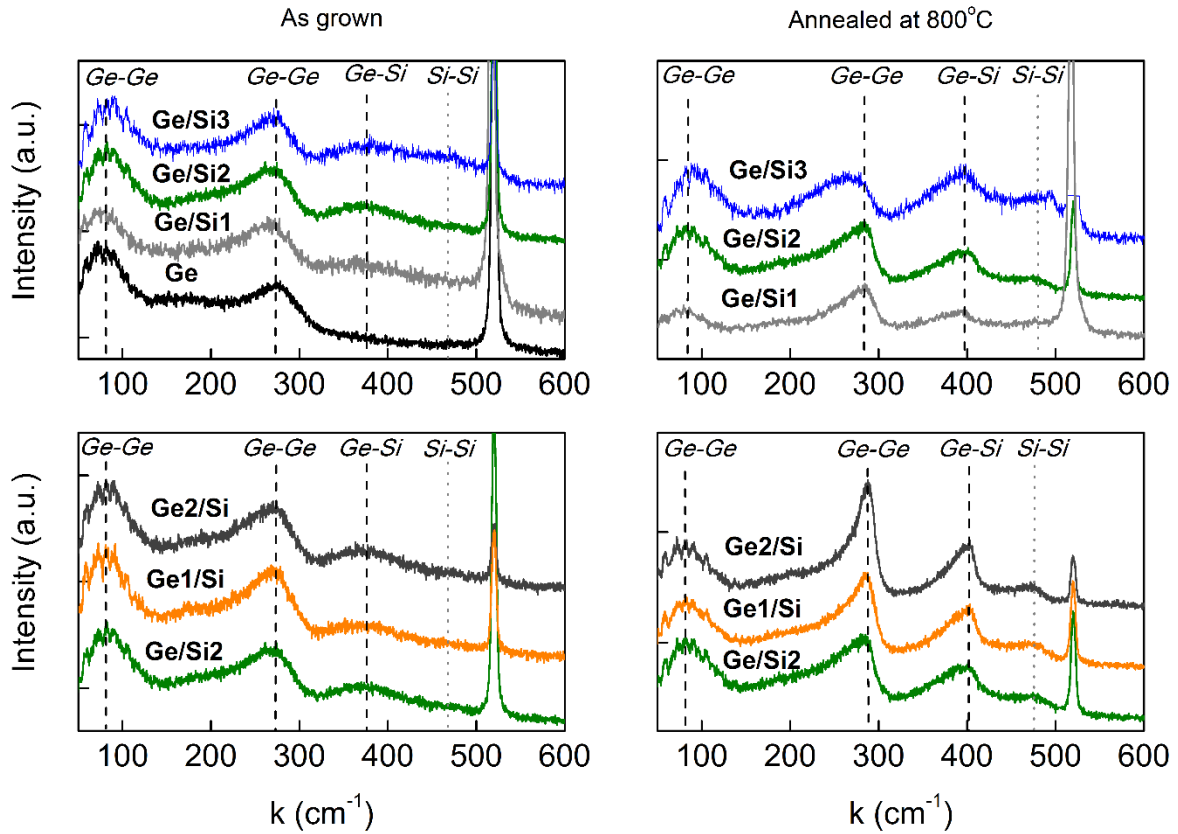

Figure 26. Raman spectrum of Ge, Ge/Si1, Ge/Si2, Ge/Si3 and Ge/Si2, Ge1/Si, Ge2/Si samples. Left column shows as-grown samples, while the right column shows samples annealed to 800 °C.

The shift of the Raman peaks toward the higher k values confirm that the QDs are crystalline. However, for the crystalline QDs Raman spectra are different than for the bulk material. The narrow, symmetrical peaks characteristic for a bulk are not present, but an asymmetrical widening toward higher frequencies (lower k) appears. This is a typical behavior for confined optical phonons and a detailed analysis of this effect can be found elsewhere. [75]

Influence of the deposition temperature

Besides changing the deposition time or the magnetron power, we can also control the deposition temperature. This parameter greatly influences the size and disorder of the nanoparticles. Buljan et al. studied the influence of the deposition temperature on similar structures $Ge+Al_2O_3/Al_2O_3$, obtained by co-depositing germanium and alumina with alternating alumina spacing layer. [46] We expect some similarities, but also some differences in the results since the simultaneous deposition of alumina with germanium influences the diffusion of germanium atoms.

For this purpose, we made three samples GeSiT1, GeSiT2 and GeSiT3 deposited on 200, 300 and 400 °C respectively, while all other parameters are kept the same.

Table 3. Germanium and silicon percentages from ERDA and the results from the numerical analysis of the GISAXS maps for samples made with different deposition temperatures.

Sample	T [°C]	Ge [at.%]	Si [at.%]	a [nm]	c [nm]	$\sigma_{LL}[nm]$	$\sigma_{LV}[nm]$	$R_{QD}[nm]$	$R_C[nm]$
Ge/SiT1	200	8.3±0.6	16.6±0.7	5.0	5.6	1.9	1.6	2.4	1.7
Ge/SiT2	300	9.5±0.6	17.5±0.8	5.7	5.7	1.9	1.3	2.5	1.8
Ge/SiT3	400	11.0±0.7	17.4±0.8	6.6	5.7	1.8	1.3	2.8	2.1

Three GISAXS maps with corresponding simulations can be found in **Figure 27** (a). Qualitative analysis of the maps implies that the increase in deposition temperature enhances the ordering, which is seen from the increasing sharpness of lateral Bragg peaks for the sample Ge/SiT3. This is explained by an increased diffusion on higher temperatures, enabling more Ge atoms to achieve the ideal nucleation spot. From the simulation, we obtained the parameters from **Table 3**. The results show that the in-layer separation of QDs a_0 increases, while the multilayer period c_0 does not change significantly. Deposition temperature influences the diffusion process, so for the higher temperature the diffusion radius increases, resulting in a slightly larger QD radius and in-layer distance. Similar results are for the $Ge+Al_2O_3/Al_2O_3$ structures. [46] **Table 3** also shows germanium and silicon percentages from ERDA. Note that the amount of germanium is increasing slightly at higher temperatures.

In-layer disorder is characterized by two parameters: deviations of the QD positions parallel (σ_{LL}) and vertical (σ_{LV}) to the ideal positions defined by the in-plane basis vector a_0. Lateral deviations are larger than the vertical ones, which is expected for this system, since the vertical position is determined by the spacing layer. Although lateral deviations stay constant with the

increased deposition temperature, the in-layer distance is increasing, which means that the ordering is improving. The relative disorder expressed as σ_{LL}/a_0 is decreasing as the deposition temperature rises, like **Figure 27** (c) clearly shows.
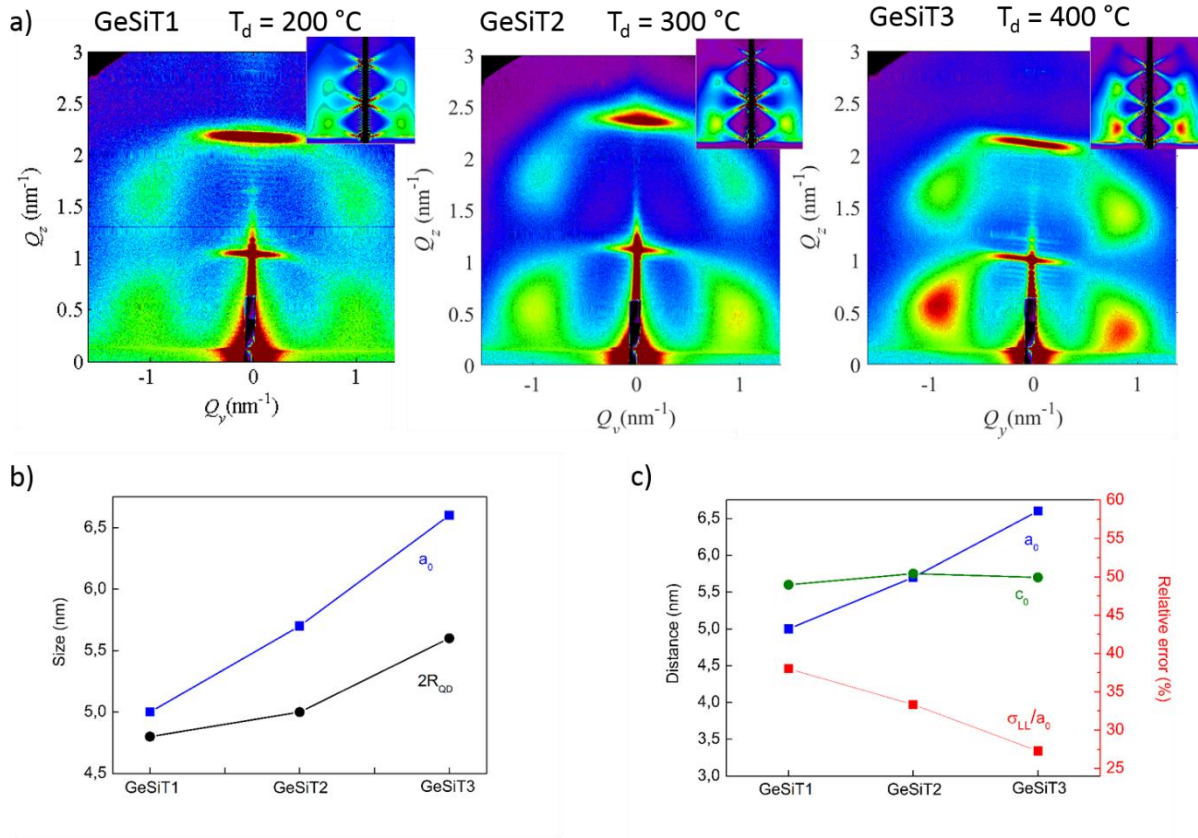

Figure 27. (a) GISAXS maps of the three samples GeSiT1, GeSiT2 and GeSiT3, differing only by the deposition temperature, (b) parameters obtained from the GISAXS simulation: lateral lattice vector a_0 and the diameter of the nanoparticles are both increasing with the temperature, (c) the relative error of the lateral disorder is decreasing with the temperature, and vertical lattice vector does not change significantly.

Influence of the spacing layer thickness

When considering the application, we must have in mind that current transport in these materials relies on tunneling and hopping between adjacent QDs. In order to achieve desirable electrical properties, the vertical distance between the QDs must be small to increase tunneling probability, but large enough to maintain quantum confinement and self-assembly.

For this reason, we created four samples: GeSiA1, GeSiA2, GeSiA3, GeSiA4, where the alumina spacing layer thickness increases, hence increasing the multilayer period from $3.7, 4.5, 5.0$ to 6.5 nm. This was achieved simply by increasing the alumina deposition time from $25, 50, 75$ to 100 s. All other parameters were kept the same as it was for the GeSi2 sample. Both GISAXS and TEM show that self-assembly was achieved for all samples and that the size of the nanoparticles is not changing significantly (**Figure 28**). The average radius ranges from $R_{QD} = 2.3 - 2.4$ nm.
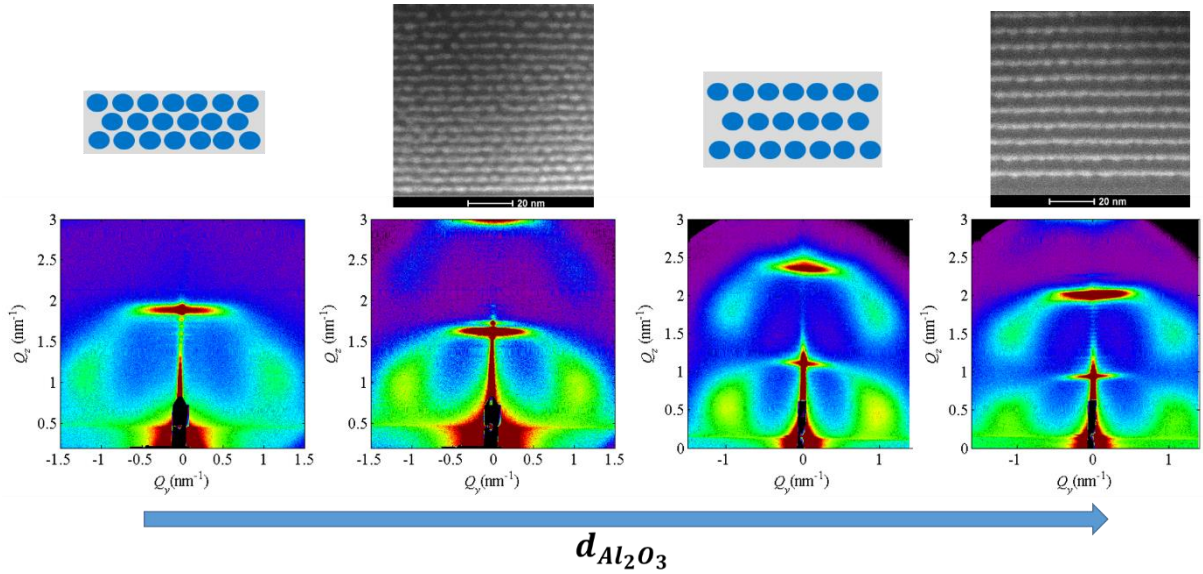

Figure 28. GISAXS maps of the four samples are shown. The multilayer period and the alumina spacing layer increases from left to right. Cross-sectional TEM images of the two samples are shown above the GISAXS maps, while schemes of the cross-section are inserted for the other two samples.

Assuming the base-central-tetragonal ordering and using simple geometry, we calculated the vertical edge-to-edge distance D for these four samples. This is actually half of the spatial diagonal in a tetragonal lattice, minus QD diameter: $= \sqrt{c^2 + \frac{a^2}{2}} - 2R_{QD}$. The results of GISAXS analysis and the calculated vertical dot distance is shown in **Table 4**. Therefore, we have shown it is possible to obtain self-assembled Ge QDs with only 0.5 nm vertical distance, which is very important to further improve the electrical properties of studied materials.

Table 4. GISAXS analysis results for samples with a varying alumina layer thickness show that it is possible to obtain self-assembled Ge QDs in alumina for a very small spacing layer, resulting in a 0.5nm vertical edge-to-edge distance.

Sample	a [nm]	c [nm]	σ_{LL} [nm]	σ_{LV} [nm]	R_{QD} [nm]	R_C [nm]	D [nm]
Ge/SiA1	4.8	3.7	1.8	1.1	2.3	1.7	0.5
Ge/SiA2	5.0	4.5	1.8	1.1	2.3	1.7	1.0
Ge/SiA3	5.7	5.0	1.9	1.1	2.3	1.7	2.0
Ge/SiA4	4.8	6.4	2.0	1.3	2.4	1.8	2.5

Influence of the matrix

It is well known that the type of the substrate influences the formation of the nanoparticles. Depending on whether it is crystalline, nanostructured or an amorphous substrate, different types of growth will occur. [76] In the case of the amorphous matrix, it not only influences the nanoparticle growth, but also the self-assembly. Since the self-assembly is attributed to the surface morphology features originating from the nanoparticles' growth, it is clear that the matrix type could affect the ordering type and the degree of regularity. [48] M.Buljan et al. have studied Ge QDs in alumina, silica and mullite matrices. [47] They showed that the alumina matrix has a tendency to smooth the surface during the growth of the film, so only the layer below the growing layer influences the morphology. In the silica matrix, on the other hand, several layers below influence the growing layer. Therefore, FCC ordering occurs in the silica matrix, while BCT is found in alumina and mullite matrices for the given layer thicknesses.

In order to avoid germanium oxidation, we are interested in silicon nitride and carbide matrices, as an alternative to oxide matrices. Also, these matrices could be a better choice because of their lower energy gap, so the tunneling probability of the charge carriers is increased.

Therefore, we introduce three sample series: GA, GN and GC, which have alumina, silicon nitride and silicon carbide as a matrix, respectively. The same deposition process was carried out for all three groups; a multilayer deposition of Ge/M where M is SiC or Si_3N_4, with a small difference for the alumina matrix group, where a silicon shell was added (Ge/Si/Al_2O_3). Magnetron powers were 150W, 125W and 300W for Al_2O_3, Si_3N_4 and SiC target respectively, with the deposition times being 120s, 110s, and 40s. Deposition times for those targets were chosen with the aim to obtain a similar spacing layer for all three matrices. Germanium target power and deposition time were the same in all three groups and samples: 10W and 55s, while

a thin silicon shell was added only in the GA group, with a magnetron power of 50W and a deposition time of only 20s.

We have seen that the deposition temperature strongly influences the ordering in the alumina matrix, so we produced three samples in each GM group, changing only the deposition temperature from 300, 400 to 500 ℃. The sample names consist of the matrix group and the deposition temperature used, for example, GC500.
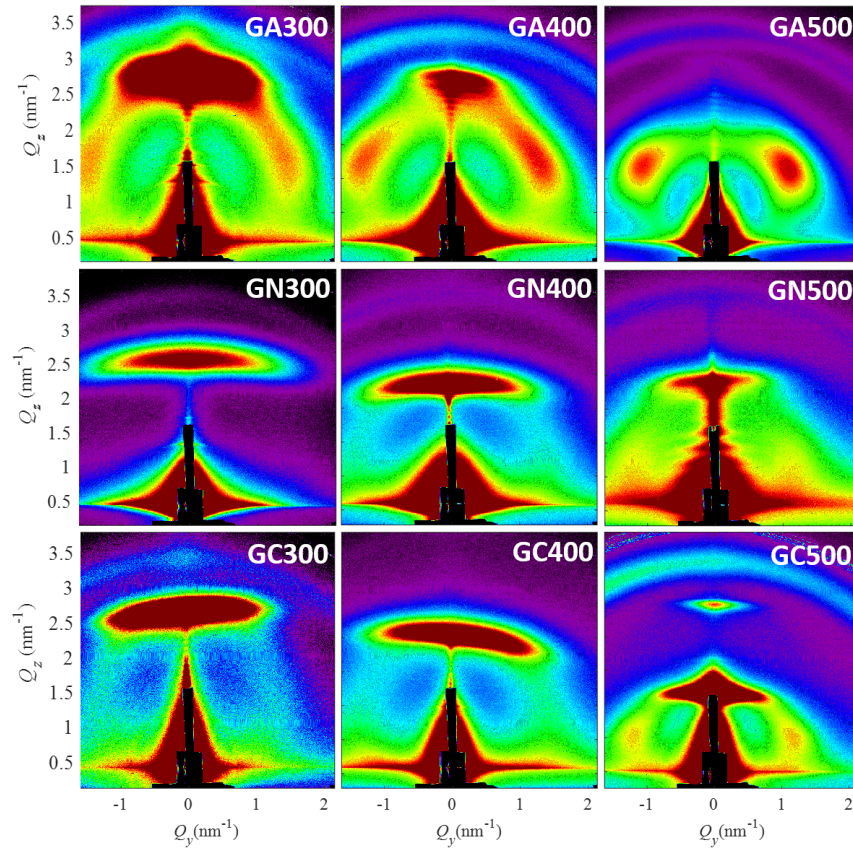

Figure 29. GM group GISAXS maps, where the first row shows samples with alumina matrix, the second silicon nitride, and the third silicon carbide matrix, while each row shows a different deposition temperature: 300, 400 and 500 °C.

GISAXS maps for those samples indicate that the nanoparticles are forming in SiC matrix for all mentioned deposition temperatures, but the ordering starts at 500℃ (**Figure 29**). In the Si_3N_4 matrix, for the lowest deposition temperature, the only multilayer structure is present and a higher temperature is needed to form nanoparticles. Nevertheless, we can say with certainty that at 500℃ particles are formed and ordered in all three matrices. This could be explained by enhanced diffusion on higher temperatures. The GISAXS analysis was done only on samples deposited at 500°C because it was difficult to obtain a good fit on other samples. All three samples have an average radius of 1.4 nm.

One sample from each group was also measured with a TEM (**Figure 30**). These images are in agreement with GISAXS measurements: indeed, all three samples contain germanium nanoparticles, while the ordering quality is lowest in silicon nitride matrix, where it is visible that after first 15 layers, QDs are no longer assembled in a lattice.
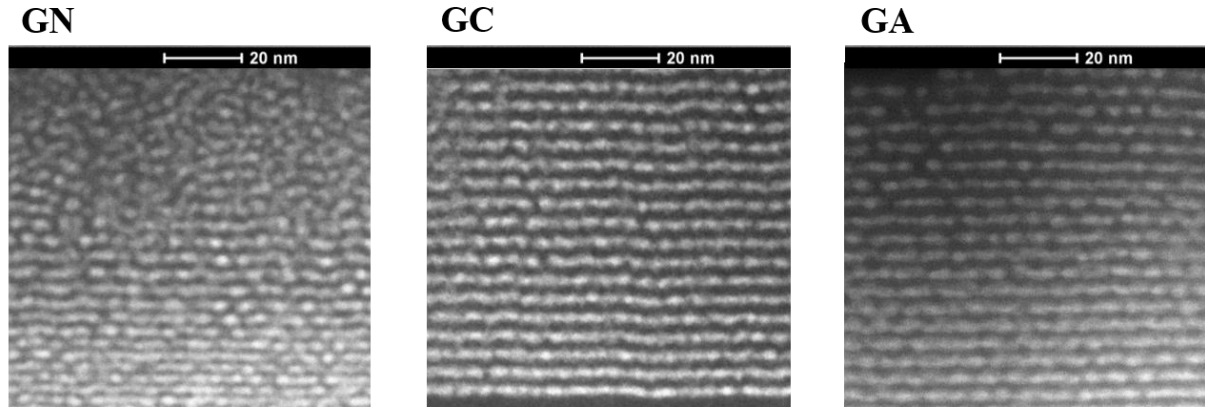

Figure 30. Cross-sectional TEM image of the GN500, GC500 and GA500 samples show that there are nanoparticles in all three matrices, but with different degree of ordering.

Figure 31. shows GISAXS maps of the samples GA500, GN500, and GC500 as-grown and annealed to 800℃. From the qualitative analysis of the maps, we can see that the structure of the GN500 sample is not significantly changed, while GA500 and GC500 samples structures are changed after annealing. Like we already explained for the alumina matrix, during annealing germanium nanoparticles undergo Ostwald ripening and form larger nanoparticles that are horizontally further apart from each other. We see here that the same is happening for the silicon carbide, but not silicon nitride matrix. Obviously, the embedding matrix significantly affects the formation of crystalline germanium QDs. A very important factor concerning germanium migration is the diffusivity in the matrix. For silicon, it was reported that Si diffusivity is eleven orders of magnitude smaller in Si_3N_4 ($\sim 3 \times 10^{-13} cm^2/s$) than in SiO_2 ($\sim 1 \times 10^{-24} cm^2/s$). [27] It is possible that also the Ge diffusivity is significantly smaller in Si_3N_4 than Al_2O_3, which would explain the GISAXS maps of the annealed GN500 sample that shows almost no change in the QD shape and structure. How this limited diffusivity affects the crystallization of Ge QDs, was discovered after the GIXRD (*Grazing Incidence X-Ray Diffraction*) measurements were done. GIXRD measurements were done in our laboratory by Dr. Krešimir Salamon.
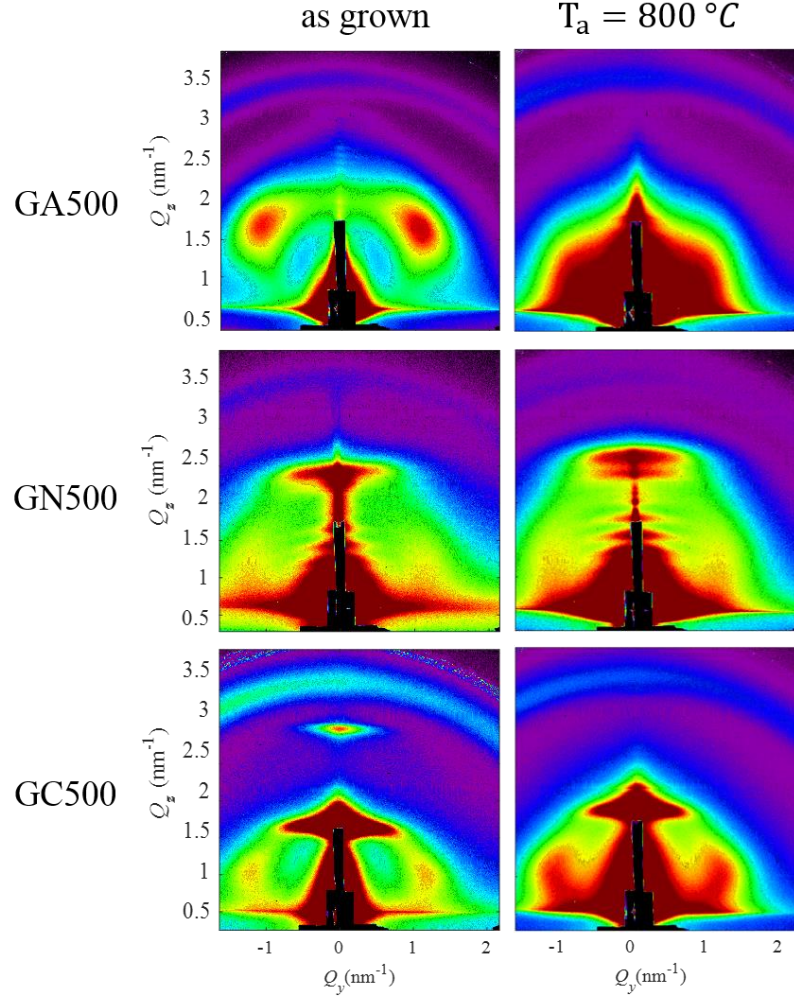
Figure 31. GISAXS maps of the samples GA500, GN500, and GC500 that contain Ge QDs in different matrices, as grown and annealed to 800 ℃.

Germanium and silicon both crystallize in FCC diamond-like structure. The temperature onset of crystallization is determined by measuring the three most intense diffraction peaks of Ge and Si: (111), (220) and (311). Usually, these peaks are considerably broadened due to the presence of nanocrystals (size effect). All samples annealed to a sufficient temperature show these diffraction peaks (**Figure 32**). This widening of the diffraction maximum is caused by the small size of the nanocrystals. [77] It is important to note that there are also other factors that could influence the widening of the diffraction curve, like crystal deformation or strain.

In Al_2O_3 matrix germanium crystallizes at 700 °C, which is visible from Raman measurements shown in the next section (**Figure 33**), where we show that germanium oxidation also plays an important role. For Ge QDs in SiC or Si_3N_4 matrix 800 °C and even 900 °C is needed, respectively. The lack of Ge crystallization in silicon nitride can be attributed to the small particle sizes. There is a critical radius above which the crystallization lowers the free energy. [27] Therefore, if germanium clusters cannot migrate because of the low diffusivity in Si_3N_4,

crystallization shall not occur for the nanoparticles under the critical radius. By further increasing the annealing temperature to 900°C and 1000°C, we managed to obtain Ge crystallization in Si_3N_4, by enhancing the diffusivity and the radius of the QDs.
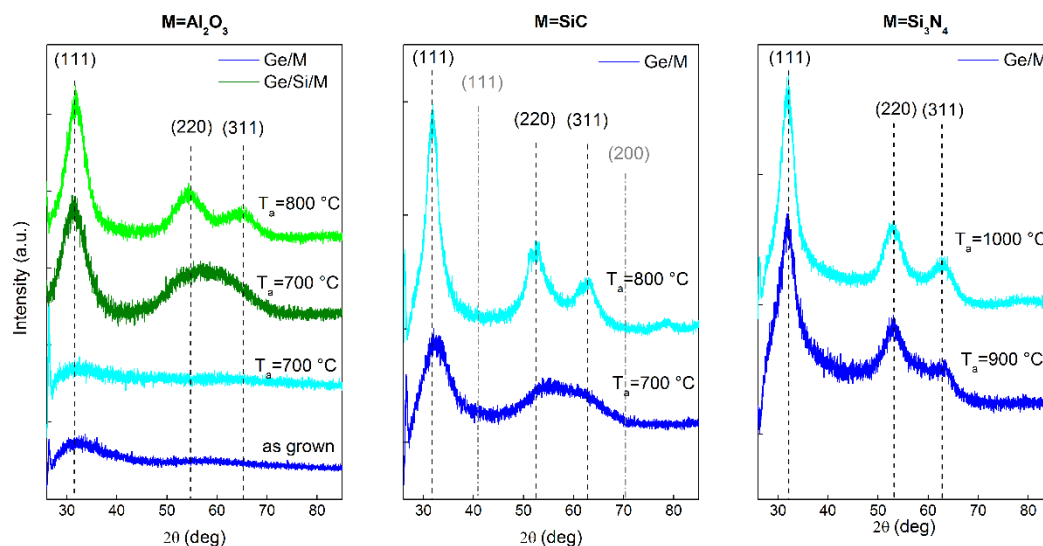
Figure 32. GIXRD measurements show the crystallization of Ge/M (blue) QDs in all three matrices. Note that Ge in Al_2O_3 is almost gone after annealing to 700 °C, while the similar sample with the silicon shell (Ge/Si) crystallizes at 800 °C. This is due to the Ge oxidation (see the next Section). In the SiC matrix, Ge/M sample crystallizes after 800 °C anneal. For the Si_3N_4 matrix annealing to higher temperatures was needed, as the crystallization starts at 900 °C.

4.2. Germanium oxidation

One disadvantage of sputtered Ge QDs in oxide matrix, like alumina or silica, is germanium oxidation. This is an unwanted effect, which reduces the amount of the active absorbing material. Moreover, after annealing such partly oxidized Ge QDs to 800 °C, volatile GeO evaporates from the sample. In case of very small QDs, surface to volume ratio is large, so almost all of the Ge oxides, especially after annealing on higher temperatures. The first notion of this effect was evident in Raman measurements and GIXRD measurements (**Figure 32**). **Figure 33** shows the Raman spectrum of the same sample of germanium QDs in alumina matrix before and after annealing to 700° C. As grown sample shows an amorphous Ge- related band that appears close to 275 cm^{-1}, after annealing to 700 °C a crystalline Ge- peak is visible, while after 800 °C there is no signal. This indicates that at 800 °C most of germanium oxidizes and evaporates out of the sample.

Simply by adding silicon into the deposition procedure after germanium, a protective Si shell will form. Samples containing silicon shell showed both Ge-Ge and Ge-Si peak in Raman, even after annealing to high temperatures (**Figure 26**).
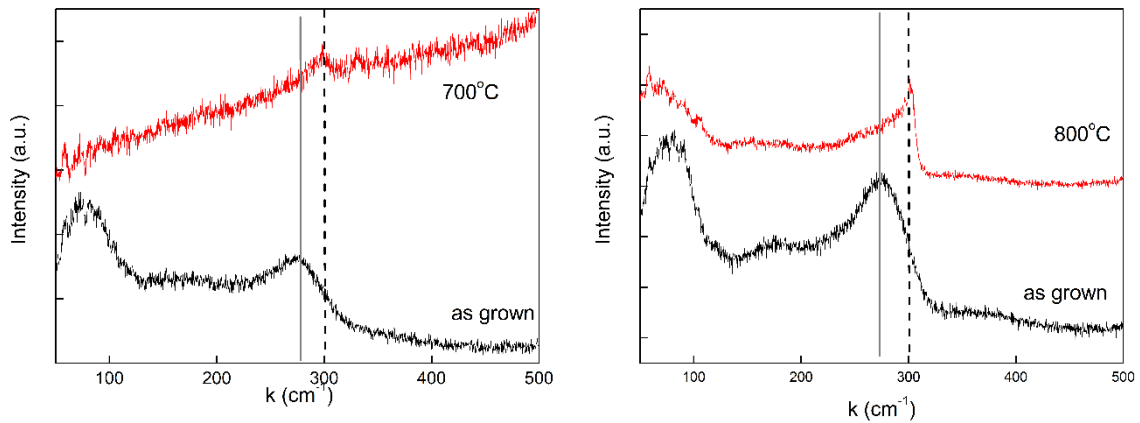

Figure 33. Raman spectra of samples Ge (left) and Ge/Si1 (right). Black line shows as grown samples, while the annealed ones are drawn with a red line.

Another way to avoid germanium oxidation is to use non-oxide matrices, like silicon carbide and silicon nitride. In order to investigate germanium oxidation in these matrices, four samples from the different matrices groups were considered: GA1, GA2, GN500, and GC500. Sample GA1 contains Ge QDs and sample GA2 has Ge/Si core/shell QDs in an alumina matrix, deposited at 300 °C. Samples GN500 and GC500 have Ge QDs in silicon nitride and carbide matrix, respectively. For the quantum dots to form in these matrices, a higher deposition

temperature was needed, so these samples were deposited at 500°C. All other deposition parameters, like germanium magnetron power and deposition time, were kept the same. These are all as-grown samples.

XPS (X-ray photoelectron spectroscopy) was done for these four samples to determine the amount of oxidation. In all samples, we observed the spectra around the Ge 2p and Ge 3d states (core levels). These levels have a characteristic spin-orbit splitting to $2p_{3/2}$ and $2p_{1/2}$, and $3d_{5/2}$ and $3d_{3/2}$. For 3d state, this splitting is small in energy (0.6 eV) but much larger for the 2p state (21 eV). Therefore, the results only show Ge $2p_{3/2}$ state, like it is commonly done in literature, while both levels are shown around Ge 3d state. [78] Spectra are characterized by a shift caused by germanium oxidation, and most of them are fitted with two or three Gaussian-Lorentzian curves. The pure Ge (Ge(0)) and germanium oxides are denoted in figures.

All samples contained a lot of oxide and carbon on the surface, due to the air exposure, so the measurements were made after cleaning the surface by bombarding it with low energy Ar ions (2 keV Ar^+). The results presented in **Figure 34** show that all samples have germanium oxide to some extent, except the sample GA2. However, the amount of Ge oxide varies; GC500 sample has an almost negligible oxidation, while GN500 contains a considerable amount of germanium oxides and in GA1 sample oxides are dominating the pure Ge. Only in the sample with the silicon shell, germanium oxide is not forming. However, the silicon shell is oxidizing instead, as it can be seen from **Figure 35**.
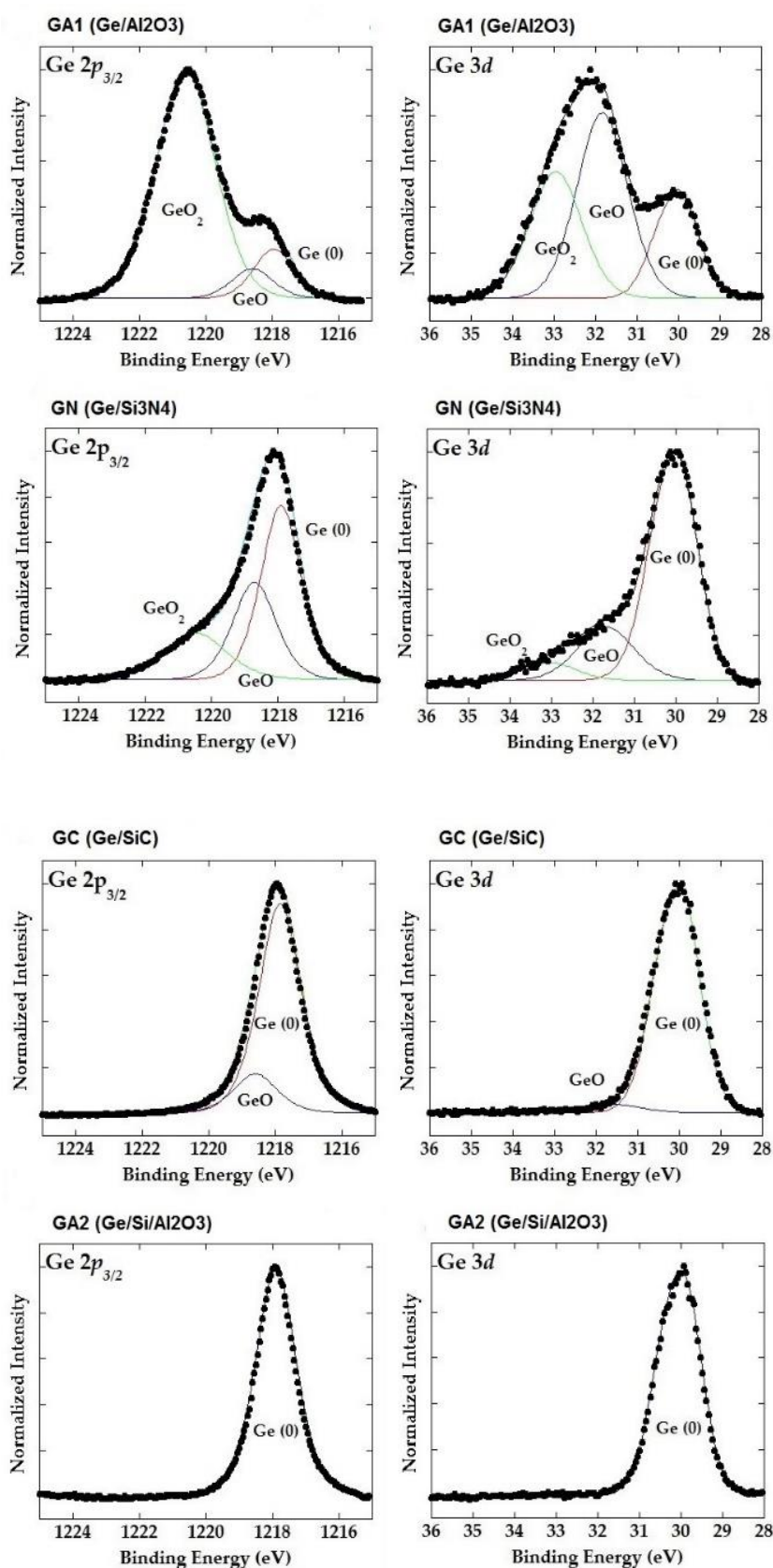
Figure 34. XPS spectra for Ge 2p3/2 and Ge 3d states for GA1, GN500, GC500, and GA2 samples.
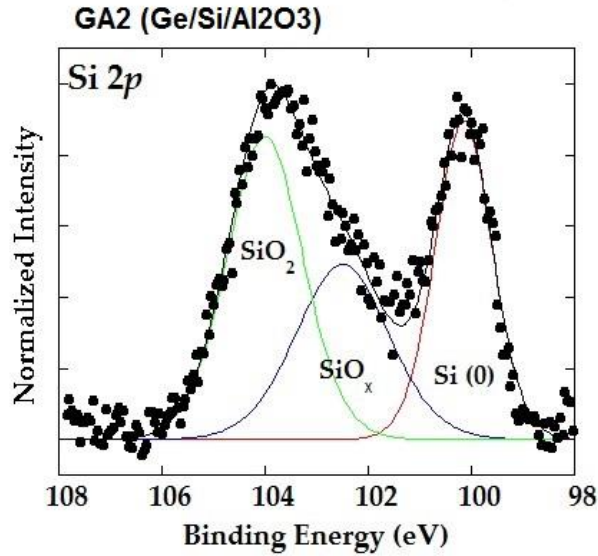
Figure 35. XPS spectra for Si 2p state. Sample GA2 is the sample with the protective silicon shell. Here we see that instead of germanium, the silicon shell partly oxidizes.

Oxygen in samples with silicon carbide and silicon nitride matrices was not expected. Its presence could be due to a slightly lower vacuum during the deposition than usual. Even ERDA measurements confirm the presence of oxygen of 14% at. in both GN500 and GC500 samples. Still, these matrices present a significant improvement when considering oxidation, compared to alumina. However, the silicon shell proved to be the most efficient in preventing germanium oxidation. This was to be expected, since silicon is in contact with aluminum oxide and a part of the silicon shell oxidizes. Along with the better self-assembly properties, this represents the advantage of Ge/Si QDs in alumina matrix over the Ge QDs in silicon carbide and nitride.

All XPS measurements were done by Dr. Iva Šarić in the Department of Physics and Centre for Micro and Nano Sciences and Technologies at the University of Rijeka.

4.3. Optical properties

When investigating nanomaterial photovoltaics, optical properties are extremely important. As we explained in Chapter **2.1.**, because of the quantum confinement effect, it is possible to tune the band gap of the nanocrystals by changing their size. This was done over the years for a variety of single-material QDs produced with different methods, confirming that there is a red shift in absorption for larger dots. [71,79] Therefore, QD-based materials are great candidates for tandem solar cells, where smaller nanocrystals would be on the top to absorb the lower wavelengths and the larger ones on the bottom would absorb the higher wavelengths. This way, a wider range of the solar spectrum would be used. [58,80] Another way to use QD materials are QD-based detectors that are able to detect a specific range of wavelengths, most often infrared, depending on the size of the dots. [81–83]

Core/shell quantum dot structures are somewhat more complex. Depending on the band gaps of the materials combined in core and shell, band gaps can align in different ways. This band alignment significantly influences the materials optical and electrical properties and therefore dictates the possible application. Precisely, Ge/Si core/shell QDs have a type II band alignment. For a sufficiently thick silicon shell, electrons and holes are located in different materials, resulting in longer exciton lifetime and smaller recombination probability. [31] This indicates that the core/shell type II materials are very promising for photovoltaics, where recombination probabilities dictate the final efficiency of the devices. Even though there have been a few theoretical articles predicting the optical properties of Ge/Si core/shell QDs, [32,33,84] this is the first experimental verification to our knowledge.

The ellipsometric analysis was done by considering each multilayer structure (Ge, Si, and alumina) as a single homogeneous film with a thickness equal to the total multilayer thickness and effective optical constants modeled using a flexible multiple-oscillator model. [85] Al_2O_3 matrix has a bandgap of about 9 eV, and is transparent in the considered spectral range. Therefore, all the absorption can be associated with the presence of Ge/Si QDs.
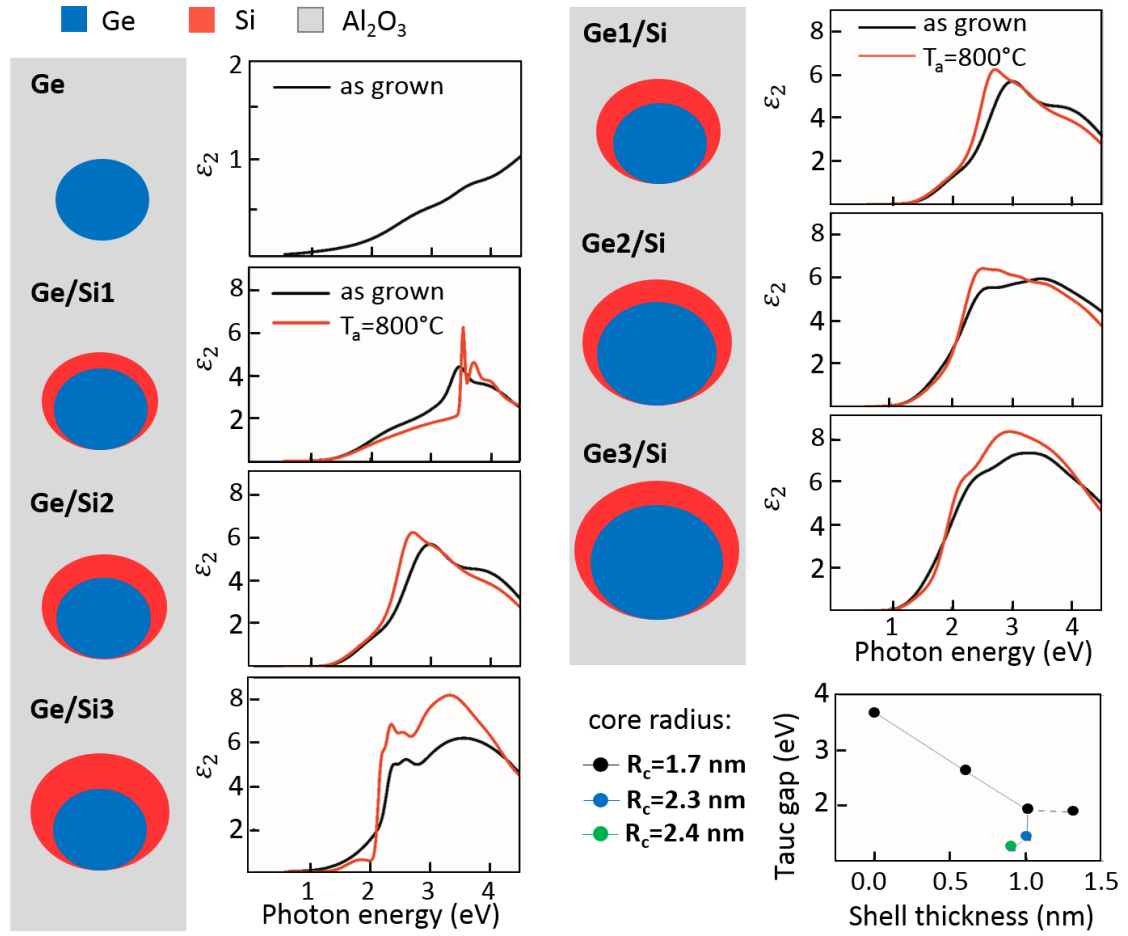
Figure 36. Tuning the optical properties by changing the shell thickness (left column) and core radius (right column). The black curve shows the as-grown and red curve the annealed samples. Lower right part shows the Tauc gap depending on the shell thickness (black dots) and core size (blue and green dot). [67]

In **Figure 36** imaginary part of the dielectric function (ε_2) is shown in dependence on the size of Si shell (left side) and Ge core (right side). As visible from the figure, the QDs with a Si shell present much stronger absorption than pure Ge QDs. This has been theoretically predicted by the larger dipole transition moments taking place in core-shell QDs in comparison to homogeneous (either Si or Ge) QDs. [33] Ge/Si QDs show a double-peak structure that has been predicted by density functional theory calculations. [32] A strong narrower peak is superimposed on the broad one. Both peaks show dependence on the size of core and shell. Remarkable confinement effects are revealed by the evolution of the narrower absorption peak with the QD morphology: decreasing the Ge core or the Si shell thickness results in a blue-shift of the absorption peaks. The relatively large shifts are obtained for the very small change in Si-shell thickness.

We have used absorption spectra and a Tauc plot to calculate the optical gap connected to the absorption peaks, often referred as Tauc gap. [86] These results are summarized in the lower right part of **Figure 36**. The strong dependence of the optical absorption on the silicon shell thickness is shown. The same figure also shows the imaginary part of the dielectric function for the annealed films (red curves).

Influence of the matrix on optical properties

Not only QD size influences the optical properties, but also the embedding matrix. Quantum confinement depends on the height of the potential barrier around the QDs. Reducing the barrier height, a weaker confinement of the electron-hole pair occurs. Besides the barrier height, other matrix effects like defects, dangling bonds, and interface states can also contribute to the optical behavior. Therefore, using the knowledge obtained by the structural analysis of the GC, GN, and GA samples, three new samples were deposited called A3, N3, and C3. Sample A3 had the same deposition parameters like the sample GA2, which has $Ge/Si/Al_2O_3$ multilayers deposited on 300 °C. Magnetron powers and deposition times were 150W/120s, 10W/55s and 50W/20s for Al_2O_3, Ge and Si target respectively, to obtain a well ordered Ge nanoparticles with a very thin silicon shell. Samples N3 and C3 were deposited at 500 °C to ensure the nucleation of Ge nanoparticles, while the magnetron powers and deposition times were 125W/110s and 300W/40s for the silicon nitride and silicon carbide targets. Germanium magnetron power and deposition time was the same as for the A3 sample. Hence, samples N3 and C3 have the same deposition parameters like samples GN500 and GC500.

This way, three samples with comparable Ge QD sizes with different embedding matrices were obtained, with diameters around 3 nm.
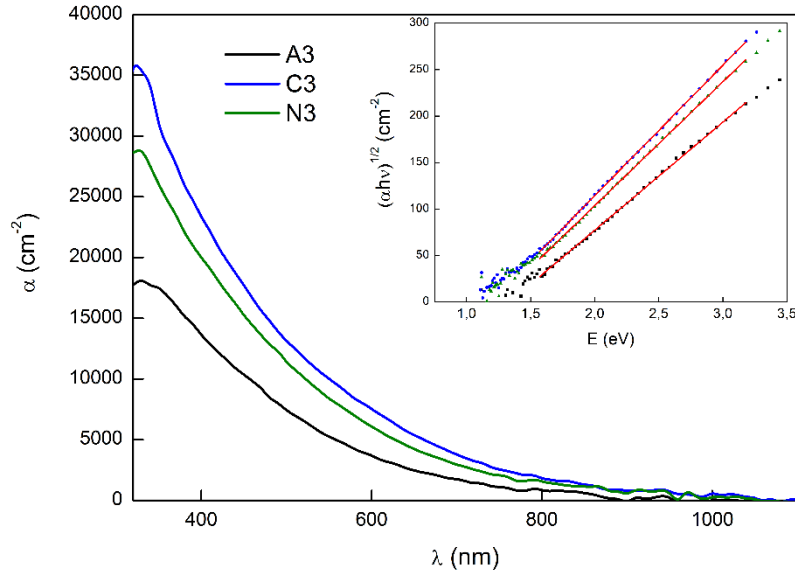
Figure 37. The absorption coefficient for the samples with Ge QDs in different matrices. The inset shows the Tauc plot for the indirect gap, while the red lines represent the linear fit.

Absorption was measured for those three samples. Silicon nitride has the bandgap of approximately 5 eV, and silicon carbide bandgap is $3 - 3.5$ eV. All three matrices are transparent in the measured range, so the absorption can be attributed to the presence of the germanium QDs. **Figure 37** shows that the absorption coefficient is the largest for the Ge QDs in a silicon carbide matrix and the lowest for the alumina matrix. Optical gap derived from fitting the Tauc plot is 1.33, 1.22 and 1.19 eV for samples A3, N3, and C3, respectively. All of them exhibit the optical gap larger than that of the amorphous bulk Ge (0.8 eV). The differences between the values of the optical gap could be due to a matrix energy gap difference. In order to explain this, we should consider the barrier heights seen by electrons and holes in the Ge QDs. For an infinite barrier, the variation of the QD energy gap is given by Eq. (7). Alumina offers the highest barrier to carriers, which results in the highest bandgap. On the other hand, silicon nitride and carbide have a lower barrier, larger delocalization of carrier wave function hence lowering the QD bandgap. Hence, a finite barrier calculation is needed, where QD band gap widening is reduced, resulting in smaller optical gap for the silicon nitride and carbide matrices.

4.4. Electrical transport and photocurrent

In previous sections, we have shown how different deposition parameters influence the ordering of nanoparticles and their absorption properties. In this section, we investigate transport in those QD-based thin films and connect it to the previous results regarding structure.

Basic I-V curves were measured on samples deposited on a p-type Si-wafer (**Figure 38**). Top contact was ITO, while the bottom contact was aluminum and a silver paste attached wire. After the contacts were deposited (but before applying the silver paste), samples were annealed to 300 °C for only 15 min to ensure an Ohmic contact. Contact area had a diameter of 0.5 cm, corresponding to an area of $0.196\ cm^2$. For all photocurrent measurements same light intensity was used.
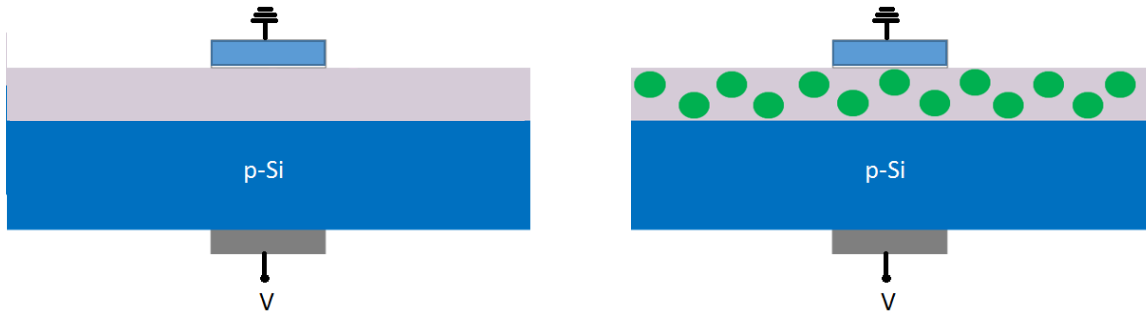

Figure 38. Schematic representation of the detector devices made, the left one presenting control devices and the right picture presenting Ge-QD devices.

Influence of the deposition parameters

First, let us start from the samples deposited at different temperatures: GeSiT1, GeSiT2 and GeSiT3. From the measured current-voltage data, current density $J = I[A]/S[cm^2]$ and electric field $E = U[MV]/d[m]$ were calculated, where $S = 0.196$ cm^2 is the contact area, and d is the thin film thickness. All devices were measured in the same voltage range $[-3, 3]$, but their thickness is not identical, thus resulting in different electric field ranges. In order to check whether the hopping conduction is present, we will try to fit the hopping conduction equation Eq. (9) on the obtained data.

Figure 40 shows an $\ln(J) - E$ plot of all three samples, convenient for a linear fit in higher electrical field region. Fit for the samples GeSiT2 and GeSiT3 were successful (inset of **Figure**

40), while the sample GeSiT1 is obviously not linear and therefore not suitable for fitting. This suggests that hopping conduction was not present for this sample, at least in this range of electric fields, or is masked by some other transport mechanism, like space charge limited current. From the slope of the fit curve, the average hopping distance can be calculated. Since the current is measured between the upper and lower contact, assuming the most probable tunneling between closest neighbors, the charge carriers jump to the closest dot in the vertical direction, like it is shown in **Figure 39**. In addition, the larger width of the barrier results in smaller current and conductivity.
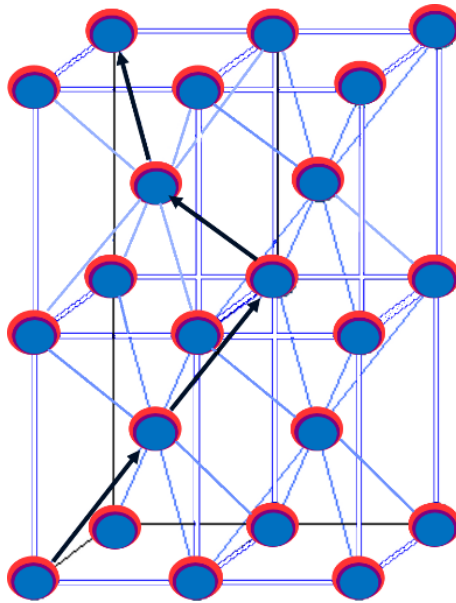

Figure 39. Black arrows represent the edge-to-edge distance *D* and a possible charge carrier path.
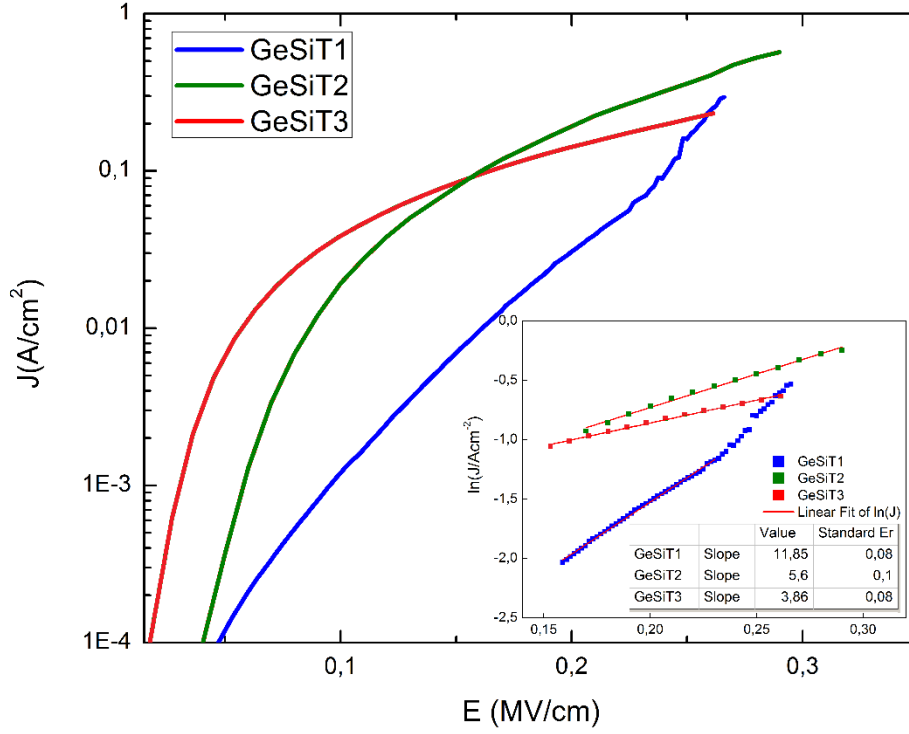
Figure 40. Current density for samples deposited on different temperatures.

Table 5 compares the shortest edge-to-edge distance between the vertical nearest neighbors D from GISAXS analysis ($D = \sqrt{c^2 + \frac{a^2}{2}} - 2R_{QD}$) with the average hopping distance a_h obtained from $\ln(J) - E$ fit. For the smaller edge-to-edge distances agreement between D and a_h is very good. This suggests the nearest neighbor hopping between localized electronic states. For samples Ge/Si3 and GeSiT1, which have a nearest neighbor distance larger than 2 nm, the hopping equation does not describe the current density behavior of these samples, and a good linear fit for those samples is not possible, which explains the disagreement in the **Table 5**.

Table 5. Shortest vertical edge-to-edge distance D obtained from GISAXS and a hopping distance a_h from the $J - E$ fit.

Sample	D [nm]	a_h [nm]
Ge	1.7 ± 0.1	1.7
Ge/Si2	2.4 ± 0.2	2.9
Ge/Si3	2.7 ± 0.2	3.8
GeSiT1	2.1 ± 0.5	3.1
GeSiT2	1.8 ± 0.3	1.5
GeSiT3	1.7 ± 0.2	1.0

For the samples with an edge-to-edge distance larger than 2 nm, current becomes limited by the injected space charge, hence masking the intrinsic conduction mechanism. A similar behavior was observed for Si QDs in a SiO_2 matrix when comparing the samples with a different number of layers. [87]

For this reason, $\log(J) - \log(U)$ graphs were plotted to be able to study the SCLC regimes. After the Ohmic behavior for small voltages, the current becomes space charge limited. In the SCLC regime for insulators $J \sim U^2$ dependence is expected. On the other hand, the slopes of the graphs in **Figure 41** have a $J \sim U^m$ behavior with $m \approx 4$ and 5. This is not unusual for QD systems, since values ranging from 3 to 5 have been reported. [87,88] In these systems, parameter m describes an exponential trap distribution below the mobility edge.
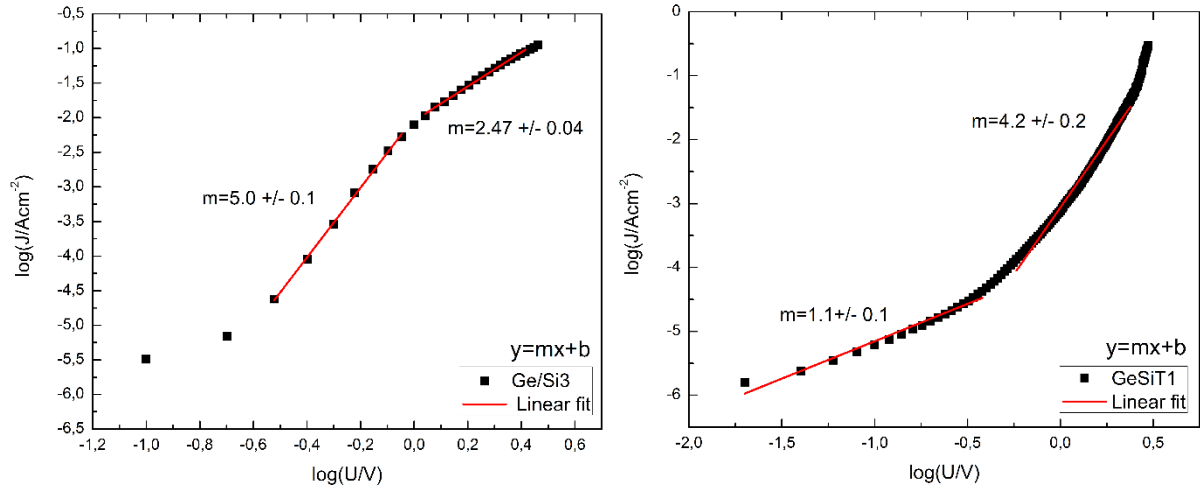
Figure 41. Space charge limited current transport in Ge/Si3 and GeSiT3 samples.

A similar SCLC behavior and the transition from a combination of trapping-detrapping in the localized states and hopping between localized states to only hopping between localized states was observed for Ge nanowire systems, when the nanowire surface to unit cell volume ratio α was increased. [89] For large enough α, their nanowire-mesh system starts to mimic the behavior expected for quantum dot arrays, and deeper trap energies were found for those samples.

Influence of the matrix

Next, the samples A3, N3 and C3, which have different embedding matrices, were investigated. First, a current-voltage dependence was measured.

Figure 42. Forward voltage current for the samples A3, N3, and C3 shown in a $log\,I - log\,U$ graph. Space charge limited current transport is present for A3 and N3 samples.

As expected, carrier transport is strongly affected by the matrix material, and the current is highest for the C3 sample with SiC matrix, due to the smallest energy barrier height.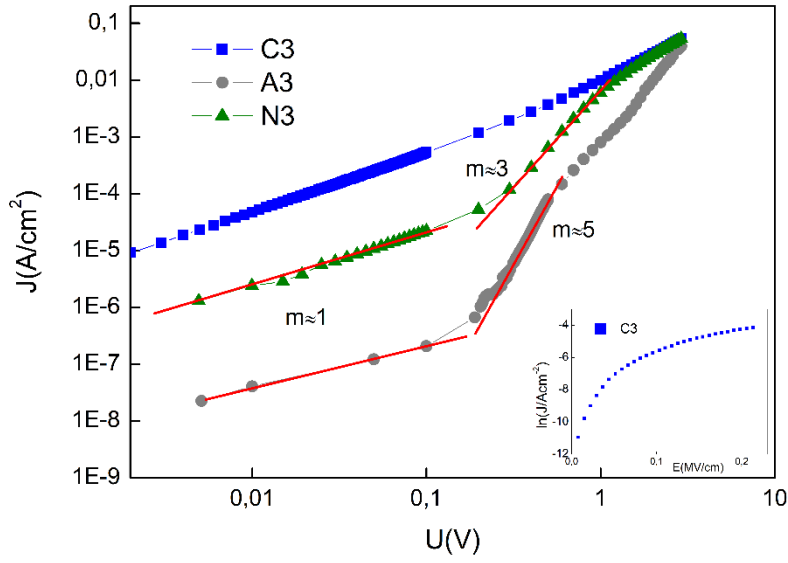 **Figure 42** shows the $log\,J - log\,U$ plot of all three samples, where it is visible that in N3 and A3 the SCLC mechanism dominates the transport. Similar to the GeSi3 and GeSiT3 samples, after a linear Ohmic range for the small voltages, current starts to grow like $J{\sim}U^m$, where $m = 3 - 5$, indicating space charge limited current not only for the sample A3 (which has alumina matrix, so the same behavior like the Ge/Si samples have is expected), but also for the sample N3 with silicon nitride matrix. On the other hand, sample C3 shows a different behavior. Drawn in a $log(J) - E$ plot (inset of **Figure 42**), for $E > 0.1$ MV/cm linear behavior is present, pointing to hopping transport. Ge QDs in silicon carbide have a smaller barrier to cross, so the tunneling probability is higher, than for the other two matrices. This causes a higher current density, better transport and no space charge.

When considering a photodetector operation, current in the reverse bias is important and needs to be low, to increase the on/off ratio. Reverse bias current for the three studied samples is shown in **Figure 43**. The inset of this figure shows the same for the control samples. The reverse bias current of control samples, without Ge QDs, is less than that of the samples with Ge QDs, because the carrier tunneling rate is lower for the pure dielectrics. The exception being the sample A1, which is the thinnest (around 30 nm only), so the contact contribution is very strong.

Sample A3 has the lowest current density at a reverse bias voltage, ranging from $10^{-7} - 10^{-6}$ A/cm^2, compared to N3 that has 10^{-5}A/cm^2 and C3 with even higher $J \approx 10^{-4}$ A/cm^2.
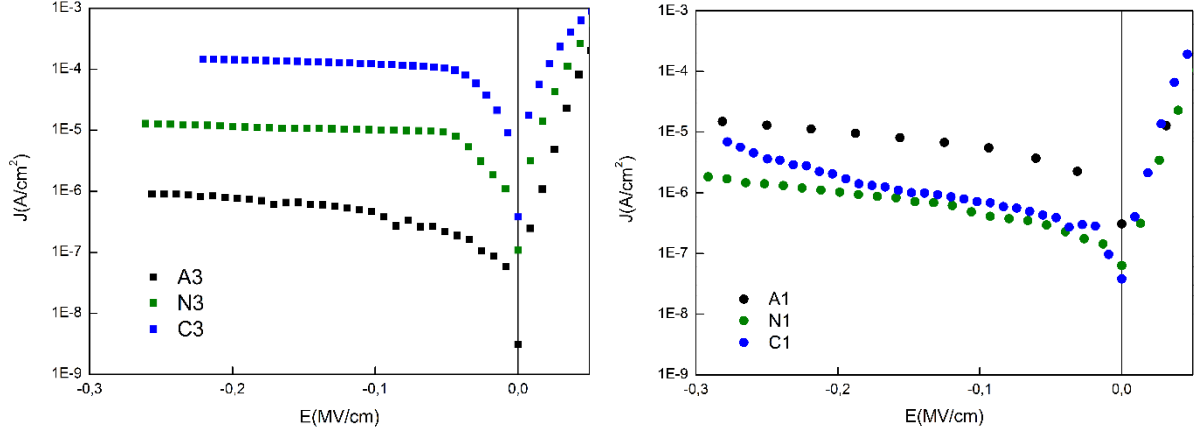
Figure 43. $Log\ (J) - U$ plot in the inversion mode (reverse-biased) for the samples A3, N3 and C3 with Ge QDs (left) and control samples without QDs - matrix only (right).

Some current mechanisms can be eliminated by a shape of the $J - U$ curve, but to distinguish between the different types of hopping, the temperature dependence of the conductivity was measured. Conductivity plotted in the $log(\sigma_{DC}) - 1/T$ graph shows a linear behavior (**Figure 44**). Therefore, in the temperature range that was measured, the parameter q from equation (12) is $q = 1$, indicating the nearest neighbor hopping between the QDs for all three samples. Conductivity of Ge/Si QDs in alumina matrix (A3) is the lowest, while Ge QDs in silicon carbide matrix have the highest conductivity (C3), as one would expect. The observed Arrhenius-like T dependence is typical of a simple, thermally activated process. Activation energies were extracted from the slope of the Arrhenius plot (Eq. (13)), and they are 0.29 eV, 0.25 eV and 0.17 eV for samples A3, N3 and C3, respectively.

Figure 44. Conductivity shows an Arrhenius like dependence on temperature for samples A3, N3, and C3. Activation energies were extracted from the slope of the linear fit.

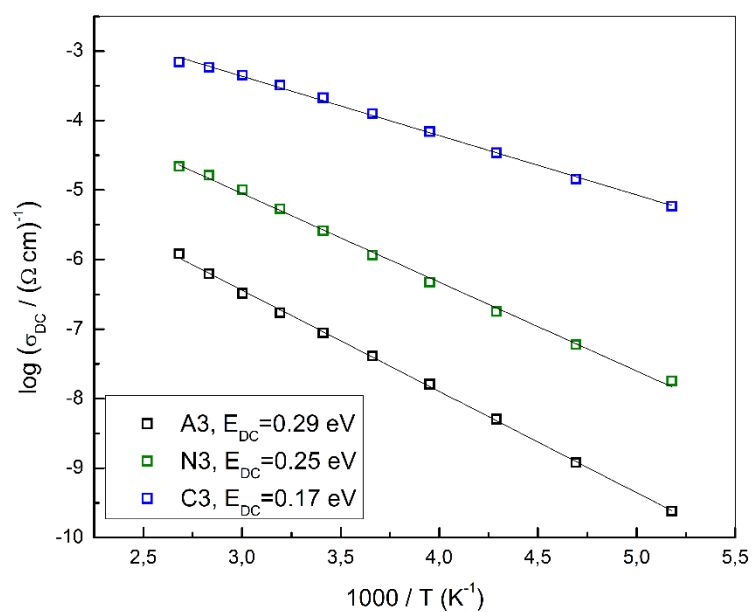These measurements were done by dr.sc. Ana Šantić, in the Laboratory for functional materials, Division of Materials Chemistry, Ruđer Bošković Institute.

Photocurrent

One of the interesting properties of studied materials is their ability to increase the current upon illumination, so there is a clear enhancement with respect to the dark current. This effect has been observed in Ge nanocrystals (NC) embedded in the SiO_2 matrix and explained by the mechanism of hole-trapping mediated by the Ge NCs. [22,26–28,71,90]

When the sample is illuminated, electron-hole pairs are generated, both in the Ge QDs and in the Si substrate. The holes have a lower ability to tunnel through the Al_2O_3 barriers, with respect to the electrons, so holes will get preferentially trapped by the Ge QD interface states. This localization of positive charge in Ge NCs facilitates extra injection of electrons from the contact, resulting in a large current enhancement under illumination. The devices operate in the inversion mode (reverse bias), since a certain electric field is necessary to extract the carriers to the contacts. Photocurrent measurements were done exactly the same like the previously described $I - V$ measurements, with the addition of illumination from the Xenon lamp light.

We have seen in the previous section that the increase of the shell thickness, effectively decreases the carrier tunneling abilities between the dots and space charge limited conduction occurs for thicker Si shell. Now we are interested to see how this influences the photocurrent and the performance of the device.

By adding a thin silicon shell, the dark current in reversed bias is decreased for almost two orders of magnitude, whereas the photocurrent is not significantly decreased (**Figure 45**). For a thicker shell (Ge/Si3), the dark current is even smaller, but the photocurrent decreases, as well.
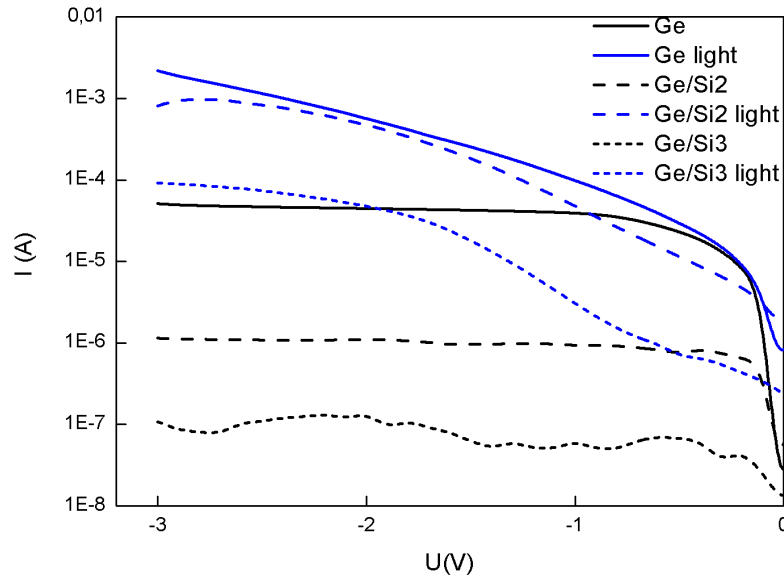
Figure 45. Samples Ge, Ge/Si2 and Ge/Si3 in reverse bias under illumination and in dark.

The reason for such an increase of current under illumination is preferential hole trapping and electron injection from the contact to ensure the charge neutrality. Hole trapping is more efficient for the QDs with a shell, since holes are trapped inside the core. This effect may also come from the fact that a part of the silicon shell oxidizes, hence increasing the barrier thickness. Therefore, a thicker shell will result in a decreased photocurrent, as well.

As a final point, we come to comparing the performances of devices containing Ge QDs with different embedding matrices. **Figure 47** shows the reverse bias current density in dark and under illumination for the three samples. In the forward bias, there is no difference between the current under illumination and in the dark, so only the reverse bias is shown. Sample A3 has the highest current under illumination, but this is true only for voltages larger than $-1V$ because a high enough electric field is needed to efficiently extract the injected carriers.
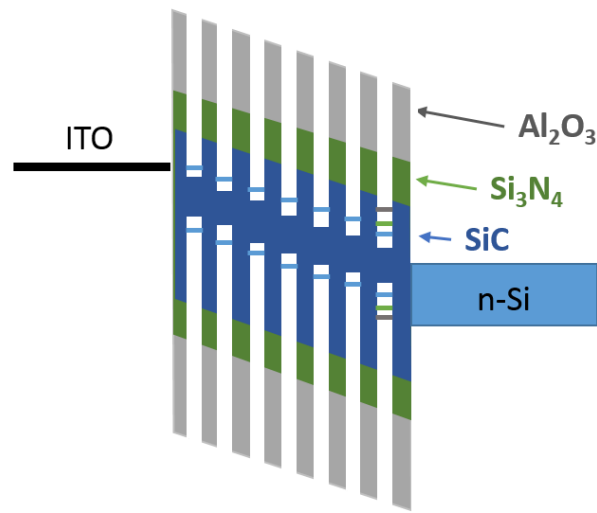
Figure 46. Schematic representation of energy band diagrams for the Ge QDs in three different matrices. Grey represents Al_2O_3, green Si_3N_4, and blue SiC. The confinement is stronger for a larger matrix bandgap, which is indicated with energy levels in conduction and valence band of Ge QDs, where the Ge QD bandgap increases.
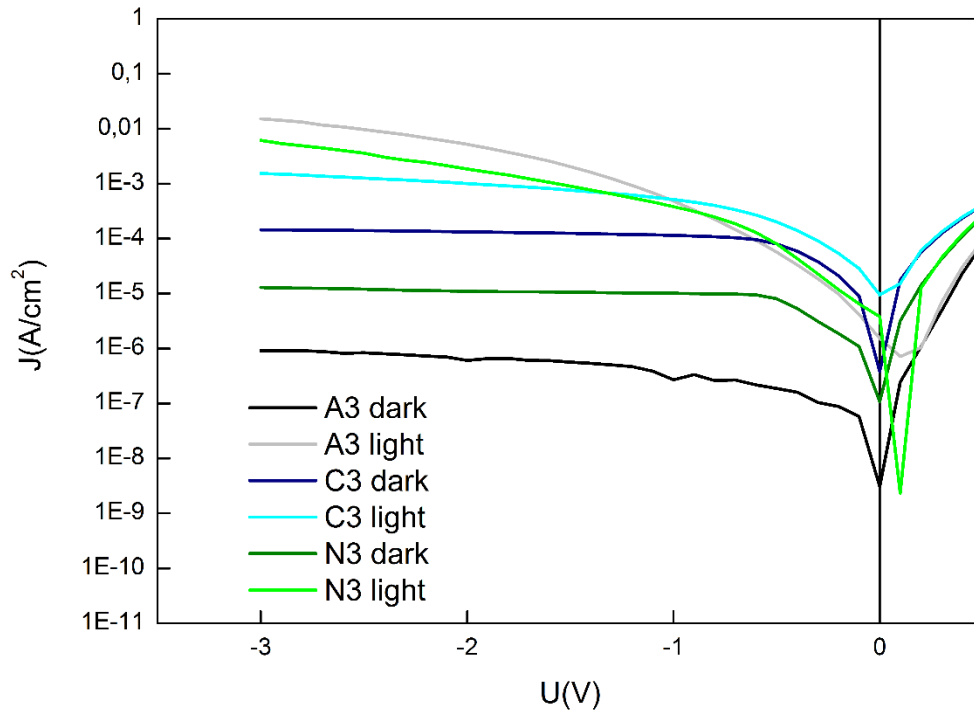
Figure 47. Comparison of the $log(J) - U$ curves for the Ge-QDs in different matrices, in the dark and under illumination.

Some articles state that the photocurrent is due to the presence of quantum dots and their control devices exhibit no such effect, [26,71] but there are also others that reported the photogeneration in samples without QDs. [28] Our control samples did show some photoconductive behavior. In control devices, the electron- hole pairs excited by illumination, that are generated in the depletion region near the Si/Al_2O_3 interface are collected. On the other hand, in the devices that contain Ge QDs, photogeneration occurs in the Ge QDs as well, therefore enhancing responsivity. For an easier analysis a graph with $I_{light} - I_{dark}$ dependence on the electric field was made, with photocurrents of all control devices drawn with a full line and QD devices drawn with a dashed line (**Figure 48**). The photocurrent in control devices could be the result of the defects in the amorphous thin matrix films, which are contributing to the hole trapping mechanism. These photocurrents are still significantly lower, than in the samples with Ge QDs, therefore confirming that the photocurrent is enhanced by the presence of Ge QDs.
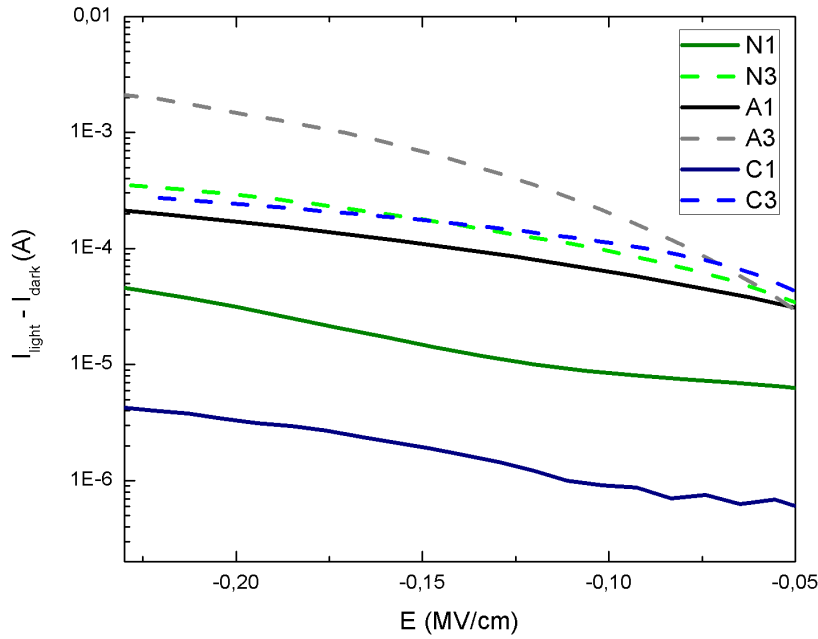

Figure 48. Photocurrent in the control samples N1, C1 and A1 (straight lines) and in the Ge QD-samples N3, C3, and A3 (dashed lines).

The fact that the sample A3 (with Ge QDs in alumina matrix) has the highest photocurrent can be explained by looking at the band alignment for Ge QDs in these three matrices. The proposed preferential hole-trapping under illumination that induces the electron injection and hence increases the current, is working when the energy barrier for the holes is higher than the one for

the electrons. **Figure 49** presents the band alignment scheme for Ge QDs in three matrices, among which Al_2O_3 stands out by its properties. Alumina matrix has the largest difference between the barrier height for electrons and for holes, hence causing efficient preferential hole trapping.

Note that in the literature different values for the bandgap and electron affinity of alumina can be found, ranging from 6.7 to 9.5 eV. [91] Also, chances are that the sputtered alumina in this work is not the same like the ones from the literature. However, all literature values have the same property of an increased hole barrier height.
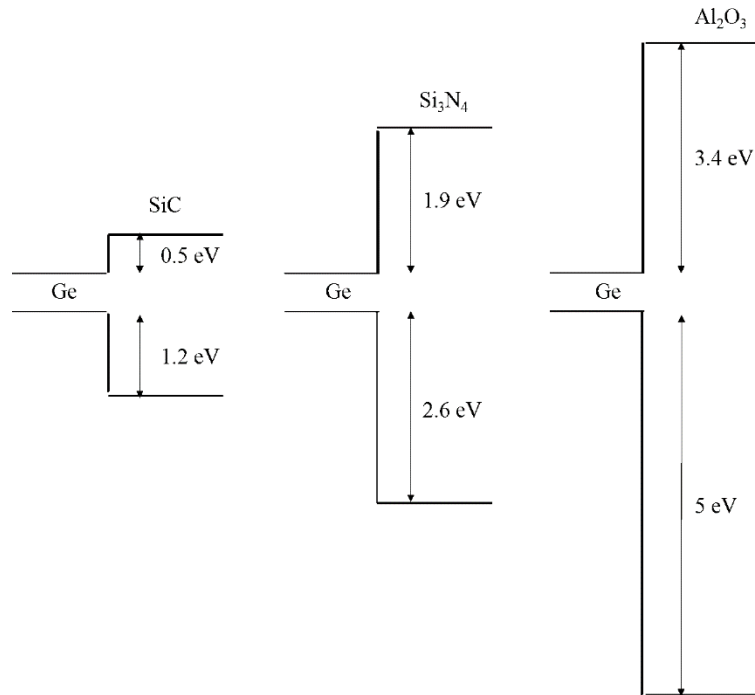
Figure 49. Band alignment scheme for Ge QDs in Al_2O_3, Si_3N_4 and SiC matrix with bandgap E_g. [19,22]

Lastly, we can conclude that the devices with core/shell Ge/Si QDs embedded in Al_2O_3 matrix are the most promising, as they exhibit the highest photocurrent and lowest dark current. Photoresponse can be further increased by changing other deposition parameters, such as deposition temperature and silicon shell. The highest achieved photocurrent in this work was 2 mA for an electric field of -0.23 MV/cm.

Detailed measurements of the spectral response in order to determine the responsivities depending on the incident light wavelength, as well as the quantum efficiency and response time remain as the aim of our future research.

5. CONCLUSION

Achieving self-assembled Ge/Si core/shell nanoparticles in alumina matrix by a simple multilayer magnetron sputtering deposition and the study of their structure depending on deposition parameters is the most important result of this work. Combination of diffusion assisted nucleation and surface morphology mechanism results in germanium nanoparticles ordered in a 3D BCT lattice. Simply adding silicon after germanium in the deposition process will result in Ge/Si core/shell quantum dots. Deposition parameters, like deposition temperature and deposition time of a certain target material significantly changes properties of the deposited thin film. An extensive research of how those parameters influence the structure, size and assembly of nanoparticles was done. In order to obtain a complete structural investigation, multiple methods were used (GISAXS, TEM, TOF-ERDA, XPS, XRD, Raman), while to get insight in application and functionality, optical and electrical measurements were done.

First group of samples consists of only Ge/Si nanoparticles in an alumina matrix. Increasing the deposition time of silicon or germanium, several samples with differing silicon shell thickness and core sizes were produced. QD sizes, shell thickness and core radius were obtained from GISAXS analysis and confirmed with TEM images. For the deposition temperature of 300 ℃, the largest QDs that were made have a 3nm radius. After that, increasing the amount of germanium results in larger QDs that merge into a thin layer. An important parameter for transport is the alumina spacing layer thickness. The vertical distance must be small to maximize tunneling probability, but still large enough to ensure QD ordering. For this reason, samples with different alumina layer thickness were made. GISAXS maps confirmed that QD self-assembly is still present for the small QD vertical edge-to-edge distance of 0.5 nm.

Increased deposition temperature enhances atomic diffusion and nanoparticle growth. Larger nanoparticles with a larger in-layer distance and a lower relative disorder are achieved for higher temperatures. GISAXS map for the sample deposited on 500 ℃ indicates higher ordering quality than for 200 ℃ deposition temperature.

Besides alumina, two other matrices were investigated: SiC and Si_3N_4, as an alternative to achieve better transport and lower degree of Ge oxidation. GISAXS maps indicated that higher deposition temperatures of 500 ℃ are necessary to obtain ordered Ge nanoparticles in these

matrices. TEM images showed that even at those higher temperatures, nanoparticles are formed in all three matrices, but with a different degree of order. Moreover, in silicon nitride matrix the ordering is present only in the first ten-twenty layers, after which QDs are randomly distributed. Matrix also strongly affects the formation of crystalline Ge QDs. Ge/Si QDs in alumina matrix and Ge QDs in silicon carbide crystallize after annealing to 800 ℃, while Ge QDs in silicon nitride require higher temperatures of $900 - 1000$ ℃ to crystallize. This could be due to lower diffusivity and high interfacial energy of Ge QDs in Si_3N_4, which require higher temperature to enhance the diffusivity and the radius of QDs.

Ge QDs in alumina matrix have a problem of Ge oxidation, especially after annealing to higher temperatures. Raman and XRD measurements showed that after annealing to 700 ℃, only a very weak Ge peak is visible, indicating that most of Ge in the film oxidized. In order to investigate this further, XPS measurements were made. They showed that even in the as grown Ge QDs in alumina matrix, germanium oxides dominate the pure Ge. The same measurement was done for Ge QDs in silicon nitride and silicon carbide matrix and revealed that even in those matrices Ge oxidation is present. Only the sample with Ge/Si core/shell QDs in alumina matrix had no Ge oxidation, but the silicon shell partially oxidized.

Furthermore, optical properties were studied using spectroscopic ellipsometry. Imaginary part of the dielectric constant, which is connected to the thin film absorption, was calculated. QDs with a Si shell showed a much stronger absorption than pure Ge QDs. Furthermore, increasing the shell thickness results in a blue-shift of the absorption peak. It is demonstrated that the optical energy gap strongly depends on the silicon shell thickness. Moreover, matrix material influences optical properties, as well. Since all matrices are transparent in the measured range, the absorption is attributed to the presence of Ge QDs. Although sizes of Ge QDs in all three matrices were very similar, the optical energy gap was lower for the QDs in silicon carbide and nitride matrices, than for alumina matrix. This is caused by lower energy gaps of these matrices.

In order to test the possible application of the studied materials, their electrical properties were measured. Electrical transport for Ge QDs embedded in all three matrices is nearest neighbor hopping between the QDs. This is visible from the temperature dependence of conductivity. Conductivity is the highest for QDs in silicon carbide and the lowest in alumina matrix, as was expected. Furthermore, the response of these devices on illumination was also tested. Reverse bias current increases a few orders of magnitude after the sample is illuminated with white light from a Xenon lamp. Under illumination, electron-hole pars are generated, but the holes are

preferentially trapped and electrons are injected from the contact resulting in current enhancement. Lowest dark current and the highest photocurrent was obtained for the sample with Ge/Si QDs in alumina matrix.

The results presented in this work enable further research in multiple directions: investigation of QD formation in silicon carbide and silicon nitride matrix and further investigation of Ge/Si QDs in alumina matrix photodetector devices. Further decreasing the nanoparticle distance would enable better transport of photocurrent. Also, additional performance measurements, such as spectral response and response time, would give an interesting insight in studied materials and better understanding in how to increase the efficiency of those devices.

PROŠIRENI SAŽETAK

1. Uvod

Poznato je da nanostrukture imaju drugačija svojstva nego isti materijali većih dimenzija. Ovisno o dimenziji nanostruktura, razlikujemo kvantne jame, kvantne žice i kvantne točke. U literaturi, izraz nanočestica koristi se za čestice veličine par nanometara do nekoliko stotina nanometara. No samo nanočestice manje od Bohrovog radijusa eksitona zovu se kvantne točke. Zbog efekta zvanog kvantno zatočenje, energijski procijep kvantnih točaka povećava se smanjenjem radijusa, što znači da se optička apsorpcija takvih nanočestica može namještati kontrolirajući njihovu veličinu.[1] Osim toga, diskretna stanja daju mogućnost pobuđenja više od jednog para elektron-šupljina za jedan apsorbirani foton. [2–4] To rezultira izvanrednim svojstvima, poput povećanja apsorpcija i fotostruje, u odnosu na odgovarajuće bulk materijale. Mijenjanje veličine, gustoće, oblika i kristaliničnosti takvih materijala vodi do različitih svojstava, te time omogućuje razne primjene, [3,5,6] od materijala za solarne ćelije, FETova do fotodetektora.

U zadnjih desetak godina, materijali s Ge kvantnim točkama postali su popularna tema istraživanja. [9,22–25] U usporedbi sa Si kvantnim točkama za koje su potrebne puno više temperature $(1000 - 1100\,°C)$, Ge kvantne točke se mogu proizvesti koristeći i niže temperature, što rezultira nižim troškovima proizvodnje. No, materijali s Ge nanočesticama u oksidnim matricama imaju poznati problem oksidacije germanija, pogotovo nakon grijanja na visoke temperature koje je potrebno za postizanje kristalizacije kvantnih točaka.

Da bismo iskoristili prednosti nanomaterijala sa silicijem i germanijem, te izbjegli oksidaciju germanija, kombiniramo ih u jezgra/ljuska strukturu. Ge/Si jezgra/ljuska kvantne točke imaju poravnanje energijskih nivoa tipa dva, što uzrokuje lokalizaciju elektrona u ljusci, a šupljina u jezgri.[31] Proteklih godina objavljeno je nekoliko teorijskih članaka o energijskim nivoima i optičkim svojstvima tih materijala, no prema našim saznanjima, ovo je prvi rad u kojem se eksperimentalno postižu Ge/Si jezgra/ljuska nanočestice.

U ovoj disertaciji opisan je proces postizanja jezgra/ljuska kvantnih točaka u aluminskoj matrici, te detaljna strukturna karakterizacija tih materijala. Postignuto samouređenje takvih

nanočestica važan je rezultat, jer daje jednostavan recept za dobivanje uređenih rešetki nanočestica. Istražen je efekt kvantnog zatočenja za različite veličine jezgre i debljine ljuske. Proizvedene su nanočestice koje se razlikuju po veličini jezgre i ljuske te međusobnoj udaljenosti pa zbog toga pokazuju drugačija optička i električna svojstva. Počevši od toga, ovaj rad je baziran na istraživanju utjecaja parametara depozicije na strukturu i uređenje kvantnih točaka, te utjecaja strukture na ostala svojstva važna za primjenu, kao što su apsorpcija, električni transport i fotostruja.

2. Teorija

Apsorpcija svjetla u poluvodiču uzrokuje pobuđenje elektrona u vodljivu vrpcu, što ostavlja šupljinu u valentnoj vrpci. Ovisno o vrsti kristala i uvjetima pobuđenja, Coulombovo privlačenje između elektrona i šupljine bi moglo voditi do vezanog stanja, Wannierovog eksitona. Karakteristična skala za relativno gibanje eksitona je Bohrov radijus, koji obično iznosi $1-20$ nm, ovisno o materijalu. Do kvantnog zatočenja dolazi kada je materijal zatočen u jednu ili više dimenzija na veličinu usporedivu Bohrovom radijusu eksitona, time ograničavajući nosioce naboja na potencijalnu jamu u jednoj ili više dimenzija, što uzrokuje kvantizaciju energija. Takve strukture, zatočene u jednu, dvije ili tri dimenzije se zovu kvantne jame, kvantne žice i kvantne točke.

Kvantne točke

Kvantna točka je poluvodička nanočestica veličine nekoliko nanometara, u kojoj su par elektron-šupljina zatočeni u sve tri dimenzije. Da bismo objasnili osnovna optička svojstva materijala s kvantnim točkama, svest ćemo problem na česticu u sferičnoj kutiji, odnosno sfernom potencijalu. U tom slučaju rješavanje Schrödingerove jednadžbe rezultira energijama koje ovise o radijusu čestice (jednadžba (4)). Da bismo slučaj kvantne točke mogli svesti na problem čestice u sferi, treba uvesti nekoliko aproksimacija.

Prva aproksimacija je pretpostavljanje paraboličnog oblika valentne i vodljive vrpce blizu ekstrema. Nosioci naboja tada se ponašaju kao slobodne čestice, a zakrivljenost vrpci je uzeta u obzir s efektivnom masom nosioca. Druga aproksimacija je aproksimacija envelope valne funkcije, koja vrijedi za nanočesticu čiji je promjer veći od konstante rešetke poluvodiča. Da bi se zadovoljio rubni uvijek, valna funkcija čestice se piše kao linearna kombinacija Blochovih funkcija.

Nadalje, ovaj račun ignorira Coulombovu interakciju između elektrona i šupljine, koja stvara eksiton, a to opravdavamo aproksimacijom snažnog zatočenja. U režimu snažnog zatočenja, radijus nanočestice mora biti puno manji od Bohrovog radijusa eksitona, ali veći od konstante kristalne rešetke. Energija zatočenja skalira s $1/r^2$, a Coulombova interakcija s $1/r$, odnosno kvadratni član dominira za dovoljno male kvantne točke.

Konačno, uz sve navedene pretpostavke, energijski procijep može se prikazati pojednostavljenom jednadžbom:

$$E_g(D) = E_g(\infty) + \frac{A}{D^2} eV \cdot nm^2 \qquad (42)$$

Gdje je procijep bulk materijala označen s $E_g(\infty)$, D je polumjer kvantne točke, a parametar zatočenja $A = \pi\hbar/2m^*$ ovisi o efektivnoj masi nosioca naboja. Veličine nanočestica u ovom radu nemaju radijuse veće od 3 nm, a Bohrov radijus eksitona za bulk Ge je 24,3 nm, stoga je razumno pretpostaviti da dolazi do snažnog zatočenja.

Jezgra/ljuska kvantne točke i poravnanje vrpci

Jezgra/ljuska strukture predstavljaju nešto kompliciraniji sustav, ali imaju nekoliko prednosti nad običnim nanočesticama. Ljuska može služiti za pasivaciju površine jezgre, kao zaštitni sloj koji sprječava oksidaciju te ovisno o poravnanju energijskih nivoa, može povećati vrijeme života nosioca naboja.

Poravnanje vrpci tipa I nastaje kada ljuska ima veći procijep od jezgre što uzrokuje lokalizaciju elektrona i šupljina unutar jezgre. Takvi materijali našli su primjenu u emitirajućim uređajima. S druge strane, poravnanje vrpci tipa II uzrokuje razdvajanje nosioca naboja. U slučaju Ge/Si jezra/ljuska kvantnih točaka šupljine ostaju u jezgri, a elektroni u ljusci, što rezultira duljim vremenom nosioca naboja.

Nekoliko teorijskih članaka spominje pogodna svojstva Ge/Si jezgra/ljuska kvantnih točaka, poput produženja vremena života nosioca naboja, mijenjanje optičkih svojstava s promjenom dimenzija jezgre i/ili ljuske, itd. No dosad nije bilo eksperimentalnih članaka koji to potvrđuju. Ovaj rad predstavlja eksperimentalnu realizaciju Ge/Si jezgra/ljuska kvantnih točaka i karakterizaciju njihovih strukturnih, optičkih i električnih svojstava.

Formacija kvantnih točaka i samouređenje

Poznati mehanizmi samoorganizacije na kristalnim površinama, kao što su Stranski - Krastanov i Volmer-Weberov rast, funkcioniraju na principu različitih kristalnih rešetki sloja koji raste i

sloja ispod rastućeg, što rezultira naprezanjem u rastućem sloju i u konačnici nastankom nanočestica. Na amorfnim površinama je priroda rasta i samoorganizacije potpuno drugačija te zahtijeva posebno objašnjenje.

Za samouređenje nanočestica dobivenih magnetronskim rasprašenjem u ovom radu odgovorna su dva mehanizma: difuzijom potpomognuta nukleacija u kombinaciji s utjecajem morfologije površine. Za vrijeme depozicije podloga se obično nalazi na povišenoj temperaturi (300 °C i više). Difuzija atoma germanija stimulirana je povišenom temperaturom. Kada određena točka na površini ima kritičnu koncentraciju Ge atoma, počinje nukleacija nanočestice. Takva nakupina je manje pokretna pa nastavlja rasti, a koncentracija Ge atoma oko nakupine se smanjuje. Zbog toga je nukleacija u tom području manje vjerojatna. Na taj način se postiže uređenje nanočestica unutar jednog višesloja (paralelno površini), no da bismo objasnili uređenje među slojevima, treba uključiti i drugi mehanizam temeljen na morfologiji površine. Vjerojatnost nukleacije će biti povećana u područjima udubljenja, odnosno između nanočestica iz prethodnog sloja. Kombinacija dva spomenuta mehanizma rezultira uređenjem nanočestica u volumno centriranu tetragonalnu rešetku.

3. Eksperimentalne metode

Svi tanki filmovi proučavani u ovom radu deponirani su magnetronskim rasprašenjem. Proizvedene su germanijeve nanočestice sa silicijevom ljuskom raznih veličina jezgre i debljina ljuske, te unutar raznih matrica. Napravljena je detaljna karakterizacija vrlo širokim rasponom metoda, od strukturnih, optičkih do električnih svojstava.

Za strukturnu karakterizaciju koristila se metoda raspršenja rendgenskih zraka pod malim kutom uz vrlo mali upadni kut (engl. *Grazing incidence small angle X-ray scattering*, GISAXS), a mjerenja su napravljena na sinkrotronu Elettra u Trstu. U kombinaciji s rezultatima ToF-ERDA (engl. *Time of flight- Elastic Recoil Detection Analysis*), koji nam daju postotak određenog materijala unutar tankog filma, može se dobiti kompletna informacija o sastavu i uređenju kvantnih točaka.

Mjerenja Ramanove spektroskopije i difrakcija X-zraka (engl. *X-ray Diffraction*, XRD) poslužile su za pronalaženje temperature kristalizacije kvantnih točaka nakon grijanja. Spektroskopska elipsometrija korištena je za mjerenje optičkih svojstava, a Fotoelektronska spektroskopija X-zraka (engl. *X-ray photoelectron spectroscopy*, XPS) daje nam informaciju o

oksidaciji germanija i silicija. Električna svojstva proučavana su jednostavnim $I - U$ mjerenjima u mraku te pri osvjetljenju, a na odabranim uzorcima izmjerena je i temperaturna ovisnost vodljivosti.

Magnetronsko raspršenje

Depozicija raspršenjem materijala samo je jedna od mogućih metoda dobivanja tankih filmova koje se svode na izbacivanje atoma iz željenog materijala i kondenzaciju izbačenih atoma na podlogu. Kod raspršenja, nije potrebna povišena temperatura, kao kod naparavanja, jer se radi o termodinamički neravnotežnom procesu. Velika prednost toga je mogućnost depozicije različitih materijala istovremeno te dobivanje smjese termodinamički nemješljivih materijala, koju nije moguće dobiti ravnotežnim procesima.

Proces raspršenja započinje upuštanjem atoma plemenitog plina (u našem slučaju Ar) u vakuumsku komoru pri tlaku od $0.1 - 1$ Pa. Prije upuštanja argona, potrebno je komoru za depoziciju ispumpat do visokog vakuuma ($\sim 10^{-6} - 10^{-7}$ Pa), kako bi se minimiziralo ugrađivanje nečistoća u tanki film. Atomi argona se ioniziraju električnim izbojem, time stvarajući plazmu. Meta sadrži materijal koji se raspršuje i spojena je na negativni izvor napona. Pozitivni ioni ubrzani električnim poljem udaraju u metu te prijenosom količine gibanja izbijaju atome s površine koji se kondenziraju na podlogu u obliku tankog filma ili nanostruktura, ovisno o materijalima mete i podloge te parametrima depozicije. Takav proces može se dodatno poboljšati uvođenjem magnetskog polja uz površinu mete, te se tada zove magnetronsko raspršenje. Statičko magnetsko polje zakreće elektrone u spiralnu putanju duž silnica magnetskog toka u blizini mete (katode), umjesto da su ubrzani prema anodi. Time je povećana vjerojatnost daljnje ionizacije argona, što u konačnici pridonosi većoj efikasnosti procesa raspršenja.

Reguliranjem parametara depozicije, kao što su brzina depozicije, trajanje depozicije pojedine mete, temperatura podloge, itd., možemo kontrolirati sastav, debljinu i morfologiju deponiranih filmova. Brzina depozicije regulira se odabirom električne snage na magnetronu i tlakom radnog plina. Odabirom materijala mete određuju se elementi koji će se deponirati na podlogu. Velika prednost korištenog uređaja za magnetronsko raspršenje je što sadrži četiri magnetronska izvora, čime se omogućava depoziciju četiri različita materijala odjednom. Nosač podloga za vrijeme depozicije rotira oko svoje osi brzinom od 10 okretaja u minuti kako bi se postigla uniformnost i izotropnost deponiranih filmova.

Uređaj korišten u ovom radu je *Multisource Magnetron Sputtering System CMS-18* proizvođača *Kurt J. Lesker Company* u Laboratoriju za tanke filmove na Institutu Ruđer Bošković.

Raspršenje rendgenskih zraka pod malim kutom uz vrlo mali upadni kut

GISAXS metoda koristi se za proučavanje strukturnih svojstava nanomaterijala. Prednost ove metode kod proučavanja tankih filmova nalazi se u malom upadnom kutu, čime se smanjuje doprinos podloge u difrakciji, odnosno dobiva se bolji omjer signala i šuma.

Difrakcijski eksperimenti s geometrijom malog upadnog kuta moraju imati dobro oblikovanu zraku, jer se većina upadnog intenziteta izgubi. Sinkrotronski izvori imaju kompaktnu, kolimiranu zraku, visokog intenziteta i sjajnosti (engl. *brilliance*). Sjajnost je parametar koji opisuje kvalitetu sinkrotronskog uređaja, tako što uzima u obzir broj emitiranih fotona u sekundi, kutnu divergenciju fotona, poprečni presjek zrake i broj fotona koji unutar 0.1% energijske širine.

Signal u GISAXS mapi dolazi od razlike u prosječnoj gustoći elektrona. Ako razlika u elektronskoj gustoći dolazi od nanočestica, intenzitet će biti proporcionalan Fourierovom transformatu njihovog oblika, odnosno form faktoru. U slučaju kada su nanočestice međusobno uređene, javlja se i dodatni doprinos difrakciji koji dolazi od korelacije položaja nanočestica. Taj doprinos se zove strukturni faktor. Jezgra/ljuska kvantne točke, zbog svog posebnog oblika, imaju drugačiji form faktor od kvantnih točaka sa samo jezgrom, što u konačnici rezultira i drugačijom GISAXS mapom. Obzirom da se radi o vrlo tankim ljuskama, debelim svega nekoliko atoma, jezgra/ljuska strukture teško je razlučiti u TEM slikama. Upravo zato su nam GISAXS mjerenja jako važna za karakterizaciju.

S adekvatnim programom za analizu, moguće je dobiti informaciju o obliku, veličini i udaljenosti među nanočesticama. Analiza izmjerenih 2D GISAXS slika temelji se na računu raspodjele intenziteta u recipročnom prostoru za raspršenje X-zraka na nanočesticama te prilagodbi parametara računa eksperimentalnim vrijednostima. Eksperimentalni rezultati za difrakciju X-zraka pod malim upadnim kutom na hrapavim površinama i nanočesticama ispod površine, mogu se opisati koristeći Bornovu aproksimaciju izobličenih valova (engl. *Distorted Wave Born Approximation*, DWBA). U toj aproksimaciji, uzorak se dijeli na dva dijela: nesmetani sustav (matrica) i smetnju (nanočestice). Tada je intenzitet difuzno raspršenog zračenja u danu točku *q* dan izrazom (24). Suma u toj jednadžbi može se pojednostaviti uz pretpostavku da veličine nanočestica nisu statistički korelirane s položajima istih, što se zove

razdvojna aproksimacija (engl. *Decoupling Approximation*, DA). Što se tiče uređenja, pretpostavlja se da se nanočestice uređuju u trodimenzionalnu rešetku s usrednjenim vektorima baze $\vec{a}^{(1,2,3)}$ pa je položaj pojedine nanočestice dan izrazom (29). Ovisno o dosegu uređenja koristimo dva modela: kratkodosežno i dugodosežno uređenje. Za dugodosežno uređenje predefinirana je idealna pozicija nanočestica, a realne pozicije variraju oko idealne vrijednosti. Kratkodosežni model predpostavlja samo da samo susjedne nanočestice utječu na poziciju, odnosno samo je udaljenost između nanočestica određena, ali ne i njihove pozicije.

U slučaju nanočestica unutar višeslojnih filmova, zbog periodičnosti slojeva dolazi do dugodosežnog uređenja u z-smjeru (okomito na podlogu), dok lateralne komponente (paralelno s podlogom) zadovoljavaju model kratkodosežnog uređenja.

4. Mjerenja i rezultati

Uzorci istraživani u ovom radu klasificirani su u grupe:

I. Ge/Si serija uzoraka namijenjena za proučavanje strukturnih i optičkih svojstava u ovisnosti o raznim parametrima depozicije. Uzorci ove serije mogu se podijeliti u četiri podgrupe, u kojoj je variran po jedan parametar: debljina ljuske, veličina jezgre, temperatura depozicije i debljina sloja alumine.

II. GA, GC i GN serije za proučavanje uređenja nanočestica u raznim matricama.

III. ACN serija u kojoj su izabrani uvjeti depozicije s najboljim uređenjem u sve tri matrice, kako bi se dalje istražila električna svojstva.

Strukturna i optička svojstva

Ova disertacija predstavlja eksperimentalnu realizaciju Ge/Si jezgra/ljuska kvantnih točaka. Proučavane Ge/Si jezgra/ljuska samouređene kvantne točke napravljene su uređajem za magnetronsko raspršenje, jednostavnom depozicijom Ge/Si/Al_2O_3 višesloja. Na taj način nastale kvantne točke su ujednačenih veličina i uređene u trodimenzionalnu volumno centriranu tetragonalnu rešetku unutar Al_2O_3 matrice. Magnetronskim raspršenjem prvo se deponira tanki sloj alumine, nakon čega slijedi depozicija germanija. Difuzijom potpomognuta nukleacija germanijevih atoma rezultira nastankom nanočestica unutar jednog sloja. Nakon toga deponira se još 20-30 takvih višeslojeva. Vjerojatnost nukleacije veća je u udubinama nanočestica od prethodnog sloja, što rezultira samouređenjem Ge kvantnih točaka u volumno centriranu

nanočestičnu rešetku. Ako se nakon germanija u redoslijed depozicije doda silicij, oko nastalih Ge jezgara silicij će činiti ljusku, te na taj način možemo postići jezgra/ljuska strukturu.

GISAXS analizom serije I. pokazano je da je moguće postići Ge/Si jezgra/ljuska kvantne točke s različitim debljinama ljuske, na način da se produži vrijeme depozicije silicija. Isto tako, produženom depozicijom germanija, postiže se veća jezgra, ali maksimalna postignuta veličina jezgre je radijusa 2,2 nm, odnosno ukupnog radiusa 3 nm, jer za veći radijus dolazi do spajanja nanočestica, odnosno stvaranja tankog sloja.

Mjerenja spektroskopske elipsometrije pokazuju da se optička svojstva Ge/Si jezgra/ljuska kvantnih točaka znatno razlikuju od svojstava kvantnih točaka koje imaju samo Ge jezgru. Uzorci s jezgra/ljuska kvantnim točkama pokazali su znatno jaču apsorpciju te vrlo prilagodljiv energijski procijep, karakteristično za zatočenje tipa II. Za vrlo male promjene debljine silicijeve ljuske, optički energijski procijep, a time i apsorpcija se znatno mijenjaju.

Povećanjem temperature depozicije povećava se međusobna lateralna udaljenost nanočestica povećava, kao i radijus nanočestica. Za to je zaslužna povećana difuzija pri većoj temperaturi. Osim toga, za temperaturu depozicije od 400 ℃, uređenje nanočestica je bolje nego za 200 ℃, što se jasno vidi iz GISAXS mapa i parametra σ_{LL}/a, koji predstavlja relativno neuređenje unutar sloja. Iz toga se može zaključiti da je postizanje nanočestica većih i od 3 nm moguće, ali je za to potrebna veća temperatura depozicije.

Nadalje, vrlo važan parametar kod električnog transporta je debljina sloja alumine koji razdvaja nanočestice u vertikalnom smjeru. Obzirom da se radi o izolatoru, svakako je poželjno da je taj sloj što tanji, ali dovoljne debljine da se ne izgubi uređenje nanočestica. Napravljena su četiri uzorka s raznim debljinama aluminskog sloja, dok su drugi parametri ostali isti. Uređenje je postignuto i za uzorak sa slojem aluminske matrice, za koji su kvantne točke između dva sloja bile udaljene (od ruba do ruba) za 0.5 nm.

Također je proučavan i utjecaj matrice na rast i uređenje kvantnih točaka. Za tu svrhu napravljena je II. serija uzoraka (GC, GN i GA), u kojoj smo uz Ge/Si uzorke u aluminskoj matrici (GA), deponirali i Ge nanočestice u matricama silicij karbida i silicij nitrida. GISAXD mape pokazuju da je tek za veće temperature depozicije od 500 ℃ postignuto uređenje u matricama silicij karbida i silicij nitrida. TEM slike potvrđuju da je uređenje najlošije u silicij nitridnoj matrici, gdje se nakon određenog broja slojeva nanočestice više nisu uređene u rešetku.

Oksidacija germanija je velik problem kod sustava s Ge nanočesticama u oksidnim matricama, pogotovo izražen pri naknadnom grijanju uzoraka (aniliranje). XPS mjerenja pokazala su da silicij karbid i nitrid nisu loša alternativa za smanjivanje oksidacije germanija, no iako to ne bismo očekivali, oksidacija je prisutna i u matrici od silicij nitrida. Mogući uzrok tome je lošiji vakuum u komori za vrijeme depozicije. U konačnici, silicijeva ljuska oko germanijeve jezgre ipak pokazuje najbolje rezultate. Iako je silicijeva ljuska djelomično oksidirala, germanijeva jezgra ostaje zaštićena.

Električna mjerenja i fotostruja

Nakon detaljne analize strukture, električna svojstva tankih filmova su izmjerena.

Do vodljivosti preskakanjem dolazi kada elektroni zarobljeni u dielektričnom filmu mogu skakati, tj. tunelirati od jednog mjesta (zamke) do drugog. Kod kvantnih točaka u dielektričnoj matrici bi moglo doći do transporta preskakanjem, ali to jako ovisi o debljini barijere između dvije kvantne točke. Ako su nanočestice previše udaljene, vjerojatnost za tuneliranje se smanjuje pa drugi mehanizmi dominiraju transportom. Struja tada postaje ograničena injektiranim prostornim nabojem, koji maskira intrinzični mehanizam transporta.

Tanki filmovi deponirani su na podlogu od p-tipa kristalnog silicija, nakon čega je kontakt od aluminija deponiran na stranu silicija, a prozirni kontakt ITO (engl. *Indium tin oxide*) na stranu tankog filma. Mjeren je protok struje između ta dva kontakta, odnosno u vertikalnom smjeru. Vrlo je zanimljivo da su svi filmovi s Ge nanočesticama pokazali značajno povećanje struje na negativnim naponima pri osvjetljenju. Takvo ponašanje ukazuje na potencijalnu primjenu istraživanih materijala za fotodetektore. Pri osvjetljenju, struja se za negativne napone povećava par redova veličina, a efekt je najizraženiji kod uzoraka s Ge/Si nanočesticama u aluminskoj matrici. Pri osvjetljenju, u nanočesticama germanija, ali i u podlozi od silicija, elektroni su pobuđeni u vodljivu vrpcu, ostavljajući šupljine u valentnoj vrpci. Pri dovoljno velikom negativnom naponu, elektroni tuneliraju prema Si-podlozi i Al kontatku, a šupljine ostaju zatočene unutar kvantnih točaka ili u zamkama površinskih defekata. Kako bi se održala električna neutralnost filma, elektroni su injektirani iz ITO kontakta što rezultira velikim porastom struje. Takvo preferencijalno zatočenje šupljina najjače je u aluminskoj matrici, što daje najveću struju pri osvjetljenju kod uzoraka s Ge/Si nanočestica u aluminskoj matrici.

5. Zaključak

Postizanje samouređenih Ge/Si jezgra/ljuska nanočestica u aluminskoj matrici jednostavnom depozicijom višesloja koristeći magnetronsko raspršenje i proučavanje ovisnosti strukture o parametrima depozicije je najvažniji rezultat ovoga rada. Kombinacijom dva mehanizma: difuzijom potpomognuta nukleacija i povećanom vjerojatnosti nukleacije u udubinama prethodnog sloja objašnjeno je nastajanje nanočestica Ge samouređenih u 3D volumno centriranu tetragonalnu rešetku. Dodavanjem silicija u proces depozicije nakon germanija, dobivaju se jezgra/ljuska kvantne točke.

Povećanjem vremena depozicije pojedine mete: silicija, germanija ili alumine, dobivene su nanočestice s raznim veličinama Si ljuske, Ge jezgre, te različitih međusobnih udaljenosti. Ukupne veličine kvantnih točaka, radijus jezgre i debljine ljuske dobivene su analizom GISAXS mapa i potvrđene su TEM slikama za nekoliko uzoraka. Najveće nanočestice za temperaturu depozicije od 300 ℃ su radijusa 3 nm. Daljnje povećanje udjela germanija rezultira spajanjem kvantnih točaka u tanki sloj. Za postizanje većih nanočestica, potrebno je povećati temperaturu depozicije. Još jedan važan parametar, posebno za električni transport, je debljina aluminskog sloja. Da bi se povećala vjerojatnost tuneliranja, međusobna udaljenost nanočestica treba biti što manja, ali i dovoljno velika da se ne izgubi uređenje. Smanjivanjem debljine aluminskog sloja, postignute su uređene nanočestice međusobne udaljenosti od samo 0.5 nm.

Nadalje, osim alumina matrice, kao alternativa za postizanje boljeg transporta i smanjivanje oksidacije Ge nanočestica, korištene su i druge dvije matrice: SiC i Si_3N_4. GISAXS rezultati pokazuju da je temperatura depozicije od 500 ℃ potrebna da bi se postigle samouređene nanočestice u tim matricama. TEM slike pokazuju da je uređenje najlošije u matrici od silicij nitrida. XPS mjerenja pokazala su da je germanijev oksid prisutan u sve tri matrice, a u najvećoj mjeri u aluminskoj matrici. No jedini uzorak koji ne sadrži germanijev oksid je uzorak s Ge/Si jezgra/ljuska kvantnim točkama, u kojima Si ljuska djelomično oksidira.

Uzorci s Ge/Si jezgra/ljuska nanočesticama također pokazuju puno snažniju apsorpciju i mogućnost pomicanja optičkog energijskog procijepa mijenjanjem debljine ljuske.

Električni transport u istraživanim tankim filmovima s Ge kvantnim točkama u tri matrice je preskakanje između najbližih kvantnih točaka, što je vidljivo iz temperaturne ovisnosti vodljivosti. Najveća vodljivost je u uzorku sa SiC matricom, dok uzorci s aluminskom

matricom imaju manje vodljivosti. Pri osvjetljenju, dolazi do povećanja struje nekoliko redova veličine. Takvo ponašanje rezultat je preferencijalnog zatočenja šupljina te injekcija elektrona iz kontakta, što uzrokuje porast struje. Najveću struju pri osvjetljenju te najmanju mračnu struju pokazuje uzorak s Ge/Si jezgra/ljuska kvantnim točkama u aluminskoj matrici.

Prezentirani rezultati omogućuju daljnje istraživanje u više smjerova: proučavanje formacije kvantnih točaka u matricama od silicij karbida i silicij nitrida, te daljnje istraživanje materijala s Ge/Si kvantnim točkama u aluminskoj matrici za fotodetektore. Dodatna mjerenja su potrebna, poput spektralnog odgovora te brzine odgovora, koji bi dali bolji uvid u svojstva uređaja te kako poboljšati efikasnost detekcije svjetlosti.

References

1.   Kůsová, K. Silicon Nanocrystals: From Indirect to Direct Bandgap. *Phys. status solidi* **215,** 1700718 (2017).

2.   Eng, P. C., Song, S. & Ping, B. State-of-the-art photodetectors for optoelectronic integration at telecommunication wavelength. *Nanophotonics* **4,** 277–302 (2015).

3.   Tomic, S., Miloszewski, J. M., Tyrrell, E. J. & Binks, D. J. Design of core/shell colloidal quantum dots for MEG solar cells. *IEEE J. Photovoltaics* **6,** 179–184 (2016).

4.   Nozik, A. J. Nanoscience and Nanostructures for Photovoltaics and Solar Fuels. *Nano Lett.* **10,** 2735–2741 (2010).

5.   Cheng, C. Semiconductor Colloidal Quantum Dots For Photovoltaic Applications. *PHD Thesis* (2014).

6.   Spitzer, M. B., Jenssen, H. P. & Cassanho, A. An approach to downconversion solar cells. *Sol. Energy Mater. Sol. Cells* **108,** 241–245 (2013).

7.   Murray, C. B., Kagan, C. R. & Bawendi, M. G. Synthesis and Characterization of Monodisperse Nanocrystals and Close-Packed Nanocrystal Assemblies. *Annu. Rev. Mater. Sci.* **30,** 545–610 (2000).

8.   Mestanza, S. N. M., Rodriguez, E. & Frateschi, N. C. The effect of Ge implantation dose on the optical properties of Ge nanocrystals in SiO2. *Nanotechnology* **17,** 4548–4553 (2006).

9.   Bogdanović-Radović, I. *et al.* Conditions for formation of germanium quantum dots in amorphous matrices by MeV ions: Comparison with standard thermal annealing. *Phys. Rev. B - Condens. Matter Mater. Phys.* **86,** 1–8 (2012).

10.   Sharp, I. D. *et al.* Stable, freestanding Ge nanocrystals. *J. Appl. Phys.* **97,** 124316 (2005).

11.   Cosentino, S. *et al.* Light harvesting with Ge quantum dots embedded in SiO 2 or Si 3 N 4. *J. Appl. Phys.* **115,** 043103 (2014).

12.   Hsu, B. *et al.* A High Efficient 820 nm MOS Ge. **24,** 318–320 (2003).

13.   Müller-Kirsch, L. *et al.* Formation of GaSb/GaAs quantum dots in MOCVD growth. *Phys. E Low-dimensional Syst. Nanostructures* **13,** 1181–1184 (2002).

14.   Stavarache, I. *et al.* Structural investigations of Ge nanoparticles embedded in an amorphous SiO2 matrix. *J. Nanoparticle Res.* **13,** 221–232 (2011).

15.   Cosentino, S. *et al.* Light absorption in Ge nanoclusters embedded in SiO2: comparison between magnetron sputtering and sol–gel synthesis. *Appl. Phys. A* **116,** 233–241 (2014).

16.   Lepadatu, A. M., Stavarache, I., Stoica, T. F. & Ciurea, M. L. Study of Ge nanoparticles embedded in an amorphous SiO2 matrix with photoconductive properties. *Dig. J. Nanomater. Biostructures* **6,** 67–73 (2011).

17.   Ray, S. K., Das, S., Singha, R. K., Manna, S. & Dhar, A. Structural and optical properties of germanium nanostructures on Si(100) and embedded in high-k oxides.

Nanoscale Res. Lett. **6,** 224 (2011).

18. Bar, R. *et al.* Multilayer Ge nanocrystals embedded within Al2O3 matrix for high performance floating gate memory devices. *Appl. Phys. Lett.* **107,** 93102 (2015).

19. Conibeer, G. *et al.* Silicon quantum dot nanostructures for tandem photovoltaic cells. *Thin Solid Films* **516,** 6748–6756 (2008).

20. Huang, S. & Conibeer, G. Sputter-grown Si quantum dot nanostructures for tandem solar cells. *J. Phys. D. Appl. Phys.* 024003 (2013). doi:10.1088/0022-3727/46/2/024003

21. Cho, E.-C. *et al.* Silicon quantum dot/crystalline silicon solar cells. *Nanotechnology* **19,** 245201 (2008).

22. Terrasi, A. *et al.* Transient photoresponse and incident power dependence of high-efficiency germanium quantum dot photodetectors. *J. Appl. Phys.* **083103,** (2016).

23. Pinto, S. R. C. *et al.* Influence of annealing conditions on the formation of regular lattices of voids and Ge quantum dots in an amorphous alumina matrix. *Nanotechnology* **23,** 405605 (2012).

24. Buljan, M. *et al.* Grazing-incidence small-angle X-ray scattering: Application to the study of quantum dot lattices. *Acta Crystallogr. Sect. A Found. Crystallogr.* **68,** 124–138 (2012).

25. Lee, S., Huang, S., Conibeer, G. & Green, M. In-situ fabrication and characterization of ordered Ge QDs in Si3N4matrix without barrier layers by rf-magnetron sputtering. *Appl. Surf. Sci.* **290,** 167–171 (2014).

26. Cosentino, S. *et al.* Role of Ge nanoclusters in the performance of photodetectors compatible with Si technology. **548,** 551–555 (2013).

27. Terrasi, A., Cosentino, S., Crupi, I. & Mirabella, S. *Ge nanostructures for harvesting and detection of light. Nanotechnology and Photovoltaic Devices: Light Energy Harvesting with Group IV Nanostructures* (2015). doi:10.1201/b18090-10

28. Tzeng, S. S. & Li, P. W. Enhanced 400–600 nm photoresponsivity of metal–oxide–semiconductor diodes with multi-stack germanium quantum dots. *Nanotechnology* **19,** 235203 (2008).

29. Tseng, S. S., Chen, I. H. & Li, P. W. Photoresponses in polycrystalline silicon phototransistors incorporating germanium quantum dots in the gate dielectrics. *Appl. Phys. Lett.* **93,** 191112 (2008).

30. Mirabella, S. *et al.* Matrix role Ge NCs in Si3N4 or SiO2. *Appl. Phys. Lett.* **101,** 011911 (2012).

31. Nestoklon, M. O., Poddubny, A. N., Voisin, P. & Dohnalova, K. Tuning Optical Properties of Ge Nanocrystals by Si Shell. *J. Phys. Chem. C* **120,** 18901–18908 (2016).

32. Javan, M. B. Ge-Si and Si-Ge core-shell nanocrystals: Theoretical study. *Thin Solid Films* **589,** 120–124 (2015).

33. de Oliveira, E. L., Albuquerque, E. L., de Sousa, J. S., Farias, G. A. & Peeters, F. M. Configuration-Interaction Excitonic Absorption in Small Si/Ge and Ge/Si Core/Shell Nanocrystals. *J. Phys. Chem. C* **116,** 4399–4407 (2012).

34.   Kechiantz, A. M., Kocharyan, L. M. & Kechiyants, H. M. Band alignment and conversion efficiency in Si/Ge type-II quantum dot intermediate band solar cells. *Nanotechnology* **18,** 405401 (2007).

35.   Banyai, Ladislaus Alexander; Koch, S. W. *Semiconductor Quantum Dots. World Scientific* (1993).

36.   QD confinement. Available at: https://warwick.ac.uk/fac/sci/physics/current/postgraduate/regs/mpagswarwick/ex5/bandstructure/.

37.   Flügge, S. *Practical Quantum Mechanics*. (Springer Berlin Heidelberg, 2012).

38.   Introduction to the Physics of Semiconductor Devices. Available at: http://www.matschmi.de/intr_phys_semi_dev/bandstructure/eff_mass.html.

39.   Norris, D. J. Measurement and Assignment of the Size-Dependent Optical Spectrum in Cadmium Selenide (CdSe) Quantum dots. 158 (1995).

40.   Liu, Y. & Ju, H. Ivan Pelant and Jan Valenta: Luminescence spectroscopy of semiconductors. *Anal. Bioanal. Chem.* **409,** 1473–1474 (2017).

41.   Barbagiovanni, E. G., Lockwood, D. J., Simpson, P. J. & Goncharova, L. V. Quantum confinement in Si and Ge nanostructures: Theory and experiment. *Appl. Phys. Rev.* **1,** 011302 (2014).

42.   Prodanović, N. Semiconductor quantum dots: intraband electronic, optical and carrier dynamical properties. (2014).

43.   Heterojunctions. Available at: https://en.wikipedia.org/wiki/Heterojunction.

44.   Buljan, M. *et al.* Crystal structure of defect-containing semiconductor nanocrystals – an X-ray diffraction study. *J. Appl. Crystallogr.* **42,** 660–672 (2009).

45.   Buljan, M. *et al.* The influence of deposition temperature on the correlation of Ge quantum dot positions in amorphous silica matrix. *Nanotechnology* **20,** 085612 (2009).

46.   Buljan, M. *et al.* Ge quantum dot lattices in Al2O3 multilayers. *J. Nanoparticle Res.* **15,** (2013).

47.   Buljan, M. *et al.* Tuning the growth properties of Ge quantum dot lattices in amorphous oxides by matrix type. *J. Appl. Crystallogr.* **46,** 1490–1500 (2013).

48.   Buljan, M. *et al.* Formation of three-dimensional quantum-dot superlattices in amorphous systems: Experiments and Monte Carlo simulations. *Phys. Rev. B* **79,** 35310 (2009).

49.   Buljan, M. *et al.* Self-assembling of Ge quantum dots in an alumina matrix. *Phys. Rev. B - Condens. Matter Mater. Phys.* **82,** (2010).

50.   Endres, J., Holý, V., Daniš, S. & Buljan, M. Kinetic Monte Carlo simulation of growth of Ge quantum dot multilayers with amorphous matrix. *J. Nanoparticle Res.* **19,** 135 (2017).

51.   Chiu, F. C. A review on conduction mechanisms in dielectric films. *Advances in Materials Science and Engineering* **2014,** (2014).

52.   Mott, N. F. & Davis, E. A. *Electronic Processes in Non-Crystalline Materials*. (OUP

Oxford, 2012).

53. Car, T. *et al.* Annealing induced semiconductor-metal transition in Ge+ITO film. *Appl. Phys. Lett.* **111,** (2017).

54. Werner, J. Origin of Curved Arrhenius Plots for the Conductivity of Polycrystalline Semiconductors. *Solid State Phenom.* **37–38,** 213–218 (1994).

55. Mentzel, T. S. *et al.* Charge transport in PbSe nanocrystal arrays. *Phys. Rev. B* **77,** 075316 (2008).

56. Ray, N., Staley, N. E., Grinolds, D. D. W., Bawendi, M. G. & Kastner, M. A. Measuring Ligand-Dependent Transport in Nanopatterned PbS Colloidal Quantum Dot Arrays Using Charge Sensing. *Nano Lett.* **15,** 4401—4405 (2015).

57. Omnes, F. Introduction to Semiconductor Photodetectors. *Optoelectronic Sensors* (2010). doi:doi:10.1002/9780470611630.ch1

58. Conibeer, G. Si and other group IV quantum dot based materials for tandem solar cells. in *Energy Procedia* **15,** 200–205 (2012).

59. Ossicini, S. *et al.* Understanding Doping In Silicon Nanostructures. *IEEE J. Sel. Top. Quantum Electron.* **12,** 1585–1591 (2006).

60. Conibeer, G. *et al.* Silicon quantum dot based solar cells : addressing the issues of doping , voltage and current transport. *Prog. Photovolt: Res.Appl.* **19,** 813–824 (2011).

61. Zhang, B., Shrestha, S., Green, M. A. & Conibeer, G. Surface states induced high P-type conductivity in nanostructured thin film composed of Ge nanocrystals in SiO2matrix. *Appl. Phys. Lett.* **97,** (2010).

62. Measurement of photodetectors. 9 Available at: http://www.dsod.p.lodz.pl/materials/OPT10_IFE.pdf.

63. Thornton, J. A. High Rate Thick Film Growth. *Annu. Rev. Mater. Sci.* **7,** 239–260 (1977).

64. Buljan, M. *et al.* Analysis of 2D GISAXS patterns obtained on semiconductor nanocrystals. *Vacuum* **71,** 65–70 (2003).

65. Jerčinović, M. Samoorganizacija i karakterizacija niklenih nanočestica u dielektričnoj matrici. (2014).

66. Buljan, M. Svojstva poluvodičkih nanočestica u amorfnoj SiO2 matrici. (2008).

67. Nekić, N. *et al.* Ge/Si core/shell quantum dots in alumina: tuning the optical absorption by the core and shell size. *Nanophotonics* (2017). doi:10.1515/nanoph-2016-0133

68. By, P., Lin, Y. W., Staff, N. & Lin, Y. Spectroscopic ellipsometry. *Mater. Today* **8,** 54 (2005).

69. Janicki, V. *et al.* Ellipsometric study of thermally induced redistribution and crystallization of Ge in Ge:SiO2 mixture layers. *Thin Solid Films* **519,** 5419–5423 (2011).

70. Lee, S., Huang, S., Conibeer, G. & Green, M. Applied Surface Science In-situ fabrication and characterization of ordered Ge QDs in Si 3 N 4 matrix without barrier layers by rf-magnetron sputtering. *Appl. Surf. Sci.* **290,** 167–171 (2014).

71. Cosentino, S. *et al.* Size dependent light absorption modulation and enhanced carrier transport in germanium quantum dots devices. *Sol. Energy Mater. Sol. Cells* **135,** 22–28 (2015).

72. Car, T. *et al.* Closely packed Ge quantum dots in ITO matrix: influence of Ge crystallization on optical and electrical properties. *Mater. Res. Express* **3,** 65003 (2016).

73. Cosentino, S. *et al.* The role of the surfaces in the photon absorption in Ge nanoclusters embedded in silica. *Nanoscale Res. Lett.* **6,** 135 (2011).

74. GISAXS. Available at: http://gisaxs.com/index.php/Q_value.

75. Arora, A. K., Rajalakshmi, M., Ravindran, T. R. & Sivasubramanian, V. Raman spectroscopy of optical phonon confinement in nanostructured materials. *J. Raman Spectrosc.* **38,** 604–617 (2007).

76. Brune, H. Growth Modes. *Encycl. Mater. Sci. Technol.* 3683–3693 (1984).

77. Popović, S. & Skoko, Ž. X-ray diffraction broadening analysis. *Maced. J. Chem. Chem. Eng. Vol 34, No 1* (2015). doi:10.20450/mjcce.2015.642

78. Wei, Y., Sullivan, J. L. & Said, S. O. A study of contaminant overlayer on Ge(100) surface using kinetic resolved XPS. *Vacuum* **45,** 597–601 (1994).

79. Tyrrell, E. Influence of elevated radiative lifetime on efficiency of CdSe / CdTe Type II colloidal quantum dot based solar cells. (2016). doi:10.1016/j.solmat.2016.01.018

80. Sun, G., Chang, F. & Soref, R. A. High efficiency thin-film crystalline Si/Ge tandem solar cell. *Opt. Express* **18,** 3746–3753 (2010).

81. Yakimov, A., Kirienko, V., Armbrister, V. & Dvurechenskii, A. Broadband Ge / SiGe quantum dot photodetector on pseudosubstrate. 4–8 (2013).

82. Konstantatos, G. & Sargent, E. H. Infrared Physics & Technology Colloidal quantum dot photodetectors. *Infrared Phys. Technol.* **54,** 278–282 (2011).

83. Bar, R., Manna, S. & Ray, S. K. Size dependent photoresponse characteristics of crystalline Ge quantum dots based photodetectors. *Opt. Mater. (Amst).* **60,** 501–505 (2016).

84. Ramos, L. E., Furthmüller, J. & Bechstedt, F. Quantum confinement in Si- and Ge-capped nanocrystallites. *Phys. Rev. B - Condens. Matter Mater. Phys.* **72,** 045351 (2005).

85. Buljan, M. *et al.* Production of three-dimensional quantum dot lattice of Ge/Si core-shell quantum dots and Si/Ge layers in an alumina glass matrix. *Nanotechnology* **26,** (2015).

86. Tauc, J, Grigorovici, R. V. A. Optical properties and electronic structure of amorphous germanium. *Phys. Status Solidi* **15,** 627–637 (1996).

87. Gutsch, S. *et al.* Charge transport in Si nanocrystal / SiO2 superlattices. *J. Appl. Phys.* **113,** 133703 (2013).

88. Ciurea, M. L. & Lepadatu, A. M. Tuning the properties of Ge and Si nanocrystals based structures by tailoring the preparation conditions Review. **10,** 59–87 (2015).

89. Ray, N. *et al. 3D Ge Nanowire Networks in an Alumina Matrix : Structure and Electronic Charge Transport.* (2018).

90. Cosentino, S. *et al.* Role of Ge nanoclusters in the performance of photodetectors compatible with Si technology. *Thin Solid Films* **548,** 551–555 (2013).

91. Jia, Y. *et al.* Band Offset Characterization of the Atomic Layer Deposited Aluminum Oxide on m-Plane Indium Nitride. *J. Electron. Mater.* **45,** 2013–2018 (2016).

92. ToF-ERDA. Available at: http://digre.pmf.unizg.hr/57/.

BIOGRAPHY

Nikolina Nekić was born on 25th of January 1991 in Zagreb, Croatia. In Osijek, she finished elementary school and 3rd gymnasium. In 2014 she graduated Research oriented study of physics at the Faculty of Science, University of Zagreb, with the thesis *Dynamics of cold rubidium atoms in the magneto-optical trap,* under the guidance of dr.sc. Ticijana Ban, done on the Institute of Physics. Half a year later, in January of 2015, she was employed as a research assistant in the Laboratory for thin films, Division for material physics at Ruđer Bošković Institute in Zagreb, where she worked on a project *Nano-networks of Quantum Dots in Glasses: From Self-assembly to Energy Conversion and Hydrogen Storage*, with dr.sc.Maja Buljan as the lead researcher. Nikolina was a part of the Cost Action project *Multiscale in modeling and validation for solar photovoltaics*. She is the author and coauthor of 6 scientific papers, one of which is in preparation, participated in 5 scientific meetings, conferences, and 3 schools/ workshops, where she presented her work in a form of a poster, or an invited talk. For five semesters she was a teaching assistant in classes Introductory Physics Lab 1 and 2 at the Physics department. Nikolina was also an active participant in science popularization events, such as ODI (Ruđer Bošković open day), first as a volunteer and later as a leader of the workshop.

LIST OF PUBLCATIONS

Publications in CC – journals

1. N. Nekić, I. Šarić,, K. Salamon, L. Basioli, J.Sancho Parramon, S. Bernstorff, M. Buljan "Self-assembly of Ge-based QDs embedded in matrices Al_2O_3, Si_3N_4, SiC: Ge oxidation", in preparation, 2018.

2. N. Nekić, J. Sancho Parramon, I. Bogdanović-Radović, J. Grenzer, R. Hübner, S. Bernstorff, M. Ivanda and M. Buljan, "Ge/Si core/shell quantum dots in alumina: tuning the optical absorption by the core and shell size," *Nanophotonics*, vol. 6, no. 5, pp. 1055-1062, 2017.

3. T. Car, N. Nekić, M. Jerčinović, K. Salamon, I. Bogdanović-Radović, I. Delač-Marion, J. Dasović, G. Dražić, M. Ivanda, S. Bernstorff, B. Pivac, M. Kralj, N. Radić and M. Buljan, „Closely packed Ge quantum dots in ITO matrix: influence of Ge crystallization on optical and electrical properties," *Materials Research Express*, 2016.

4. T. Car, A. Šantić, N. Ray, N. Nekić, K. Salamon, S. Bernstroff and M. Buljan, "Annealing induced semiconductor- metal transition in Ge + ITO film", *Applied Physics Letters,* vol 111, no. 17, pp. 172104, 2017.

5. S. A. Mezzasalma, T. Car, N. Nekić, M. Jerčinović, M. Buljan "Temperature behaviour of the average size of nanoparticle lattices co-deposited with an amorphous matrix. Analysis of Ge+Al2O3 and Ni+Al2O3 thin films," *Journal of Physics: Condensed Matter*, vol 29, no. 43, pp. 435301, 2017.

6. M. Buljan, M. Karlušić, N. Nekić, M. Jerčinović, I. Bogdanović-Radović, S. Bernstorff, N. Radić, I. Mekterović, "GISAXS analysis of ion beam modified films and surfaces", *Computer Physics Communications*, no. 212, pp. 69-81, 2017.

Conference abstracts

1. N. Nekić, I.Šarić, R. Hübner, S. Bernstorff, M. Buljan, "Structure and transport properties in self-ordered Ge-based quantum dots embedded in different matrices", *Nanotexnology NN18 and ISSON18*, Thessaloniki, Greece, 2018. (poster, international peer review)

2. N. Nekić, J. Sancho Parramon, J. Grenzer, R. Hübner, S. Bernstorff, M. Buljan, "Structure and transport properties in quantum dot lattices of Ge/Si core/shell quantum dots

in different matrices", *Physics of Solar Cells: from basics to nanoscience*, Les Houches, France, 2018. (poster, international peer review)

3. L. Basioli, V. Despoja, J. Sancho Parramon, S. Fazinić, <u>N. Nekić</u>, S. Bernstroff, G. Dražić, M. Ivanda, M. Buljan, "Self-assembled Ge/metal core/shell nanoparticles in alumina matrix", *Programme and book of abstracts*, Ljubljana, 2018. str. 11-11 (invited talk, peer review)

4. <u>N. Nekić</u>, J. Sancho Paramon, J. Grenzer, I. Bogdanović-Radović, M. Ivanda, R. Hübner, M. Jerčinović, S. Bernstorff, V. Holy, M. Buljan, "Quantum dot lattices of Ge/Si core/shell quantum dots in alumina glass matrix for application in solar cells," *EMRS Spring Meeting,* Lille, France, 2015. (poster, international review)

5. <u>N. Nekić</u>, J. Sancho Parramon, J. Grenzer, I. Bogdanović-Radović, M. Ivanda, R. Hübner, M. Jerčinović, S. Bernstorff, V. Holy, M. Buljan, "Quantum dot lattices of Ge/Si core/shell quantum dots in alumina glass matrix for application in solar cells," *22nd International Scientific Meeting on Vacuum Science and Technique: Program and Book of Abstracts,* Osilnica, Slovenija, 2015. pp. 22-22 (invited talk, peer review)

6. T. Car, <u>N. Nekić</u>, N. Radić, M. Jerčinović, K. Salamon, I. Bogdanović-Radović, I. Delač Marion, J. Dasović, B. Pivac, G. Dražić, "Closely packed Ge quantum dots in ITO matrix: influence of Ge crystallization on optical and electric properties," *22nd International Scientific Meeting on Vacuum Science and Technique: Program and Book of Abstracts*, Osilnica, 2015. pp. 38-38 (poster, international peer-review)